Magnetic Helicity Fluxes and their Effects in Dynamo Theory

Licentiate Thesis

Simon Candelaresi
Nordita, Stockholm, Sweden
Supervisor: Prof. Axel Brandenburg, Nordita

14 January 2011

List of papers included in the thesis

I **Magnetic-field decay of three interlocked flux rings with zero linking number.**
Del Sordo F., Candelaresi S. and Brandenburg A.
Phys. Rev. E, 81:036401, Mar 2010

II **Decay of trefoil and other magnetic knots.**
Candelaresi S., Del Sordo F. and Brandenburg A.
In *Advances in Plasma Astrophysics.* Cambridge University Press.
arXiv:1011.0417

III **Small-scale magnetic helicity losses from a mean-field dynamo.**
Brandenburg A., Candelaresi S. and Chatterjee P.
Mon. Not. Roy. Astron. Soc., 398:1414-1422, September 2009

IV **Equatorial magnetic helicity flux in simulations with different gauges.**
Mitra D., Candelaresi S., Chatterjee P., Tavakol R. and Brandenburg A.
Astronomical Notes, 331:130-135, January 2010

V **Magnetic helicity transport in the advective gauge family.**
Candelaresi S., Hubbard A., Brandenburg A. and Mitra D.
Physics of Plasmas, 18:012903, 2011

List of papers not included in the thesis

A **Magnetic helicity fluxes in alpha omega dynamos.**
Candelaresi S. and Brandenburg A.
In *Advances in Plasma Astrophysics.* Cambridge University Press.
arXiv:1012.4354

B **Influence of magnetic helicity in MHD.**
Candelaresi S., Del Sordo F. and Brandenburg A.
In *Astrophysical Dynamics: From Stars to Galaxies.* Cambridge University Press.
arXiv:1008.5235

List of Symbols

The definition of all symbols are placed in the text where they occur for the first time. This is a list with some generally used symbols which are not obvious to every physicist.

h	$= \boldsymbol{A} \cdot \boldsymbol{B}$ magnetic helicity density (gauge dependent)
$\overline{\boldsymbol{B}}$	mean value of $\boldsymbol{B}$
$\dot{\boldsymbol{B}}$	$= \frac{\partial}{\partial t}\boldsymbol{B}$ partial time derivative of $\boldsymbol{B}$
$u_{i,j}$	spatial derivative in the j direction of the ith component of u
$\boldsymbol{\mathcal{E}}$	$= \boldsymbol{u} \times \boldsymbol{b}$ electromotive force
ϕ_i	magnetic flux of loop i
η_t	turbulent magnetic diffusivity
η_T	$= \eta + \eta_\mathrm{t}$ total magnetic diffusivity
κ	diffusion coefficient
Re	fluid Reynolds number, defined in (10)
$\mathrm{Re_M}$	magnetic Reynolds number, defined in (10)
$\mathrm{Pr_M}$	$= \mathrm{Re_M}/\mathrm{Re}$ magnetic Prandtl number
$\frac{\mathrm{D}}{\mathrm{D}t}$	$= \frac{\partial}{\partial t} + \boldsymbol{U} \cdot \boldsymbol{\nabla}$ advective derivative
$\langle . \rangle$	spatial average
$\Re(z)$	real value of the complex number z

Abstract

The roles of magnetic helicity and magnetic helicity fluxes in astrophysical objects are investigated using various models and field configurations. Their roles in dynamo theory are confirmed through magnetohydrodynamic simulations both within the framework of mean-field theory and in direct numerical simulations.

The constraint of magnetic helicity conservation in a periodic system at high magnetic Reynolds numbers is analyzed for setups of three magnetic flux rings which can be interlocked. The linking is able to hinder the magnetic field to decay only if the linking implies magnetic helicity. If the magnetic field is not helical the decay shows the same behavior irrespective of the actual linking of the rings which supports the assumption that only the magnetic helicity is the decisive topological quantity in magnetic relaxation.

The regime of high magnetic Reynolds numbers is analyzed by using a one-dimensional mean-field model for a helically forced dynamo. A wind with linear profile is imposed such that magnetic helicity can be advected to one of the domain boundaries. It is shown that with vacuum boundary conditions helicity can be shed from of the domain, which alleviates the quenching at high magnetic Reynolds numbers. Additionally the same boundary is closed for a different setup where a diffusive flux is allowed at the midplane of the system. This is shown to also reduce the quenching mechanism and to allow for dynamo action at large magnetic Reynolds numbers.

The influence of the gauge on magnetic helicity transport and fluxes is explored in the Weyl gauge, the resistive gauge and the pseudo-Lorenz gauge as well as a newly introduced advecto-resistive gauge. In the first three gauges spatially averaged fluxes are analyzed and compared with the one-dimensional mean-field model. The alleviation of the quenching is independent of the gauge as it was expected since it is a physical effect. In the advecto-resistive gauge magnetic helicity density evolves like a passive scalar in the kinematic regime owing it to the advective nature of the gauge. In the dynamical regime magnetic helicity is advected into length scales of the turbulent eddies.

Contents

1 Introduction

The magnetic activity of the Sun has been observed for more than 400 years[1] starting with Galileo Galilei and his contemporaries who observed sunspots for the first time in 1609. Sunspots are regions on the photosphere which are cooler (3000–4500K) than the surface temperature of 5770K. The decrease in temperature is caused by the intense magnetic field in the spots (up to 2000 gauss) which reduces convection and the rise of hot material. Subsequently that area cools down via thermal radiation. The appearance of the sunspots does not happen randomly in time, but shows an 11 year cycle. During this period the azimuthally averaged number of sunspots versus time and latitude shows a butterfly like diagram (Fig. 1). This is interpreted to be due to the equatorial migration of the magnetically active regions which follow the same cycle with a reversed polarity every 11 years (Fig. 2).

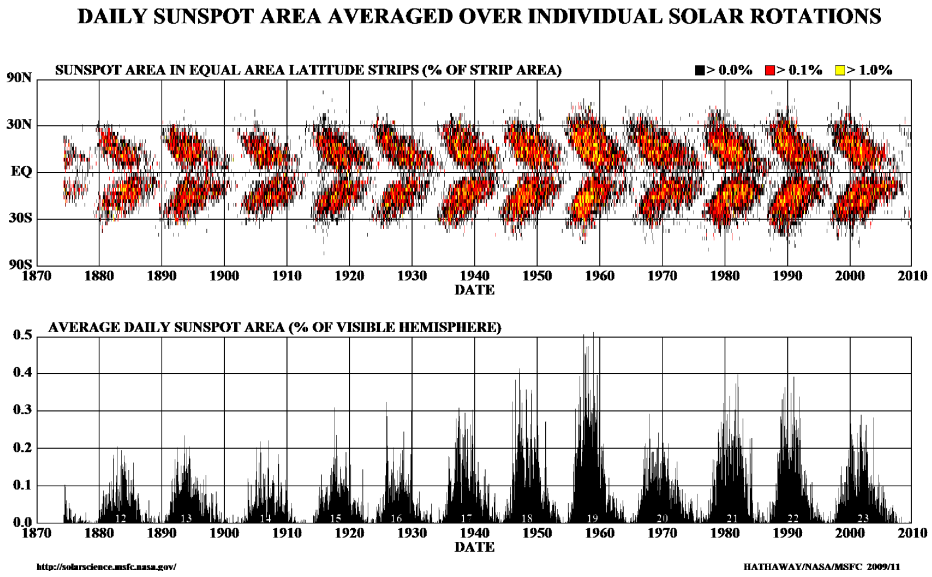

Figure 1: Sunspot diagrams showing the 11 years cycle. Note the apparent onset of another cycle in the year 2009 which had been long waited for.

[1] Until Hale's discovery in 1908 it had not been known that the Sun has a magnetic field. But since the sunspots are manifestations of intense field regions it is fair to say that unknowingly the magnetic field had been observed.

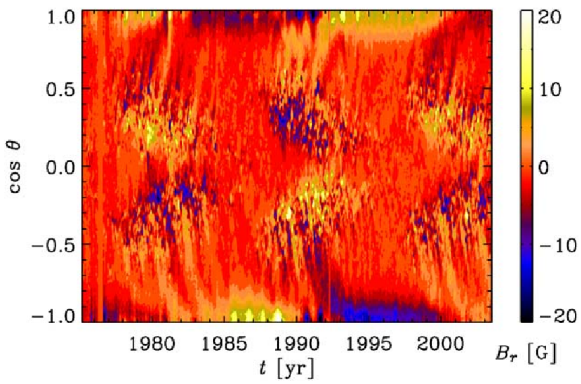

Figure 2: Longitudinally averaged radial component of the magnetic field observed by R. Knaack. The axes denote cosine of the colatitude ($\cos\theta$) and time in years.

Since the Sun's magnetic field is alternating it cannot be a relic one and must be generated from inside. Its cause is believed to be a dynamo (see [Brandenburg, 2009] for a review). In a first rigorous existence proof, it was shown by analytical works [Herzenberg, 1958] that for certain motions and boundary conditions it is possible to generate and maintain large scale magnetic fields in a magnetohydrodynamic (MHD) system[2]. In [Herzenberg, 1958] two rigid spheres embedded in a conducting medium were considered. It was shown analytically that for certain relative rotation angles magnetic fields are generated. How dynamo action is achieved and how magnetic fields on large scales are being kept up are the central questions of current research.

The role of magnetic helicity $H_\mathrm{m} = \int \boldsymbol{A}\cdot\boldsymbol{B}\,\mathrm{d}V$, where $\boldsymbol{B}$ is the magnetic field and $\boldsymbol{B} = \nabla\times\boldsymbol{A}$, has been suggested to play a crucial role in the creation of large scale magnetic fields. When computing power became more viable large scale fields could be generated in simulations [Léorat et al., 1975]. This was accompanied by a cascading of helicity into large scales (inverse cascade).

It is the aim of this work to find the role of magnetic helicity during the dynamo process in the astrophysical context and how magnetic helicity fluxes contribute. The tool of choice is the Pencil Code[3] which is a high-order finite difference PDE solver.

[2] An MHD systems can be a conducting liquid or a plasma.
[3] http://pencil-code.googlecode.com

2 Framework

2.1 Basic Magnetohydrodynamics

Astrophysical plasmas are approximated to being electrically conducting fluids for which the equations of magnetohydrodynamics (MHD) apply. By combining the Navier-Stokes equations for a compressible fluid with the Maxwell equations (see appendix B) one obtains a set of MHD equations. By further taking the non-relativistic limit the displacement current can be neglected. In MKS units the MHD equations for a compressible viscous fluid can be written as follows:

$$\begin{aligned}
\dot{\rho} + \boldsymbol{\nabla} \cdot (\rho \boldsymbol{U}) &= 0 && (1)\\
\rho \dot{\boldsymbol{U}} + \rho(\boldsymbol{U} \cdot \boldsymbol{\nabla})\boldsymbol{U} + \boldsymbol{\nabla} p &= \boldsymbol{J} \times \boldsymbol{B} + \boldsymbol{F}_{\text{visc}} + \boldsymbol{F} && (2)\\
\boldsymbol{\nabla} \times \boldsymbol{B} &= \mu_0 \boldsymbol{J} && (3)\\
\boldsymbol{\nabla} \times \boldsymbol{E} &= -\dot{\boldsymbol{B}} && (4)\\
\boldsymbol{\nabla} \cdot \boldsymbol{B} &= 0 && (5)\\
\boldsymbol{J} &= \sigma(\boldsymbol{E} + \boldsymbol{U} \times \boldsymbol{B}). && (6)
\end{aligned}$$

The quantities are defined as follows:

ρ	density of the medium
$\boldsymbol{U}$	velocity field, sometimes written $\boldsymbol{v}$
p	pressure
$\boldsymbol{J}$	electric current density
$\boldsymbol{B}$	magnetic flux density (aka magnetic field)
μ_0	vacuum magnetic permeability
$\boldsymbol{E}$	electric field
σ	electric conductivity
$\boldsymbol{F}$	external force
$\boldsymbol{F}_{\text{visc}}$	viscous force with $\boldsymbol{F}_{\text{visc}} = \rho^{-1}\boldsymbol{\nabla} \cdot 2\nu\rho\mathbf{S}$ and $\mathsf{S}_{ij} = \frac{1}{2}\left(U_{i,j} + U_{j,i}\right) - \frac{1}{3}\delta_{ij}\boldsymbol{\nabla} \cdot \boldsymbol{U}$ is the traceless rate of strain tensor for a monatomic gas, with the viscosity ν

Using the equation of state of an isothermal gas one can combine all these equations and express $\boldsymbol{B} = \boldsymbol{\nabla} \times \boldsymbol{A}$ in terms of its vector potential $\boldsymbol{A}$ which

yields the three commonly used equations:

$$\frac{\partial \boldsymbol{A}}{\partial t} = \boldsymbol{U} \times \boldsymbol{B} + \eta \nabla^2 \boldsymbol{A} \tag{7}$$

$$\frac{\mathrm{D}\boldsymbol{U}}{\mathrm{D}t} = -c_\mathrm{s}^2 \boldsymbol{\nabla} \ln \rho + \boldsymbol{J} \times \boldsymbol{B}/\rho + \boldsymbol{F}_\mathrm{visc} \tag{8}$$

$$\frac{\mathrm{D} \ln \rho}{\mathrm{D}t} = -\boldsymbol{\nabla} \cdot \boldsymbol{U}, \tag{9}$$

with the magnetic diffusivity $\eta = 1/\mu\sigma$, the magnetic permeability μ, the speed of sound c_s and the advective derivative $\frac{\mathrm{D}}{\mathrm{D}t} = \frac{\partial}{\partial t} + \boldsymbol{U} \cdot \boldsymbol{\nabla}$. For the derivation of equations (7) to (9) the vector calculus identities in appendix A are used.

Commonly used parameters in MHD to characterize the medium are the hydrodynamic and magnetic Reynolds number

$$\mathrm{Re} = \frac{UL}{\nu}, \quad \mathrm{Re_M} = \frac{UL}{\eta}, \tag{10}$$

where U is a typical velocity of the system which we usually take to be the root mean square (rms) of the velocity and L is a characteristic length which is usually taken to be the length of the energy carrying eddies. In the extreme case of a perfectly conducting fluid (ideal MHD) the magnetic diffusivity $\eta \to 0$ and the magnetic Reynolds number $\mathrm{Re_M} \to \infty$.

2.2 Frozen-in Magnetic Fields

In the limit of low magnetic diffusivities η (high magnetic Reynolds numbers $\mathrm{Re_M}$) magnetic field lines move with the fluid [Priest and Terry, 2000, pp. 23] (introduced by Hannes Alfvén). In other words, the field lines get distorted the same way as the fluid itself (Fig. 3). One then says that the field is "frozen-in". Since in astrophysical bodies $\mathrm{Re_M}$ is very high ($\mathrm{Re_M}(\mathrm{Sun}) = 10^9$, $\mathrm{Re_M}(\mathrm{galaxies}) = 10^{29}$) this concept is of fundamental importance for most of the coming discussions.

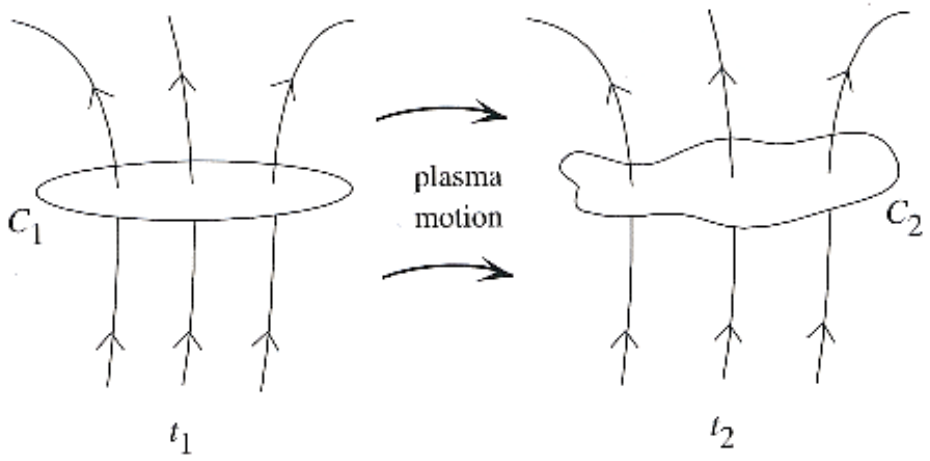

Figure 3: The magnetic field lines through the area C_1 get distorted the same way as the area itself. So the magnetic flux through C_2 keeps the same [Priest and Terry, 2000, p. 24].

2.3 Magnetic Relaxation and Stability

Force-free magnetic fields were believed to exist in astrophysical bodies like nebulae. The justification was that the Lorentz force in these objects would be so strong that it could not be compensated by a pressure gradient or gravitational forces. A force-free configuration would mean:

$$\alpha \boldsymbol{B} = \boldsymbol{\nabla} \times \boldsymbol{B}, \tag{11}$$

with the constant α. This was questioned by [Chandrasekhar and Woltjer, 1958] who were looking for the maximum magnetic energy of a plasma under the constraint that energy dissipation $\int_V (\boldsymbol{\nabla} \times \boldsymbol{B})^2 \, \mathrm{d}V$ is constant in time. The result is a more general form of the force-free condition (11):

$$\boldsymbol{\nabla} \times (\boldsymbol{\nabla} \times \boldsymbol{B}) \quad = \quad \alpha^2 \boldsymbol{B}, \tag{12}$$

with the constant Lagrangian multiplier α. Equation (12) gives more general solutions than (11) whose solutions are contained in (12). However the constraint of the constant energy dissipation does not seem physically justified and so the more plausible constraint of constant magnetic helicity was used to derive a similar formula.

In [Woltjer, 1958a] it was shown that the magnetic helicity does not change in time for the case of ideal MHD, i.e. $\eta = 0$:

$$\frac{\mathrm{d}}{\mathrm{d}t}\int_V \boldsymbol{A}\cdot\boldsymbol{B}\ \mathrm{d}V = 0, \tag{13}$$

where the magnetic field vanishes at the boundaries. With this constraint the minimum magnetic energy fulfills:

$$\boldsymbol{\nabla}\times\boldsymbol{B} = \alpha\boldsymbol{B}. \tag{14}$$

This result is also true in the limit $\eta \to 0$. Adding interactions between fluid and fields and using the full MHD equations more constraints than the constant helicity have to be taken into account. In that case equation (14) will change and for a compressible fluid $\boldsymbol{B}$ for the minimum energy will depend on the density fluctuations [Woltjer, 1958b].

Another highly important relaxed state which was experimentally discovered for toroidal and helical magnetic fields was explained by [Taylor, 1974]. Under the constraint of magnetic helicity conservation the minimal magnetic energy state is given by

$$\boldsymbol{\nabla}\times\boldsymbol{B} = \lambda\boldsymbol{B}, \tag{15}$$

where λ is a function in space and constant along the magnetic field lines, viz $\boldsymbol{B}\cdot\boldsymbol{\nabla}\lambda = 0$. From this it can be shown that by increasing the angle between the toroidal and the actual field (i.e. increasing the helicity) the field in the toroidal direction flips sign at a certain angle. This is the so-called *reversed field pinch*.

2.4 Mean-Field Theory

Solving for the full MHD equations in three dimensions can be computationally very costly. In order to reduce the calculations needed one can compute mean quantities where the small-scale turbulent effects are embodied in mean-field coefficients. This is the mean-field approach [Moffatt, H. K., 1978, Krause and Raedler, 1980] and it is widely used in MHD. The fields are split into a mean part and a fluctuating part, e.g.

$$\boldsymbol{B} \;=\; \overline{\boldsymbol{B}} + \boldsymbol{b}, \tag{16}$$

where $\boldsymbol{b}$ is the fluctuating part of the field and $\overline{\boldsymbol{B}}$ is a mean value and can be taken over 1, 2 or 3 dimensions, e.g.

$$\overline{\boldsymbol{B}}(z,t) \;=\; \int \boldsymbol{B}(\boldsymbol{x},t)\ \mathrm{d}x\ \mathrm{d}y \tag{17}$$

for a planar average. However it is not important how the averaging is done as long as the Reynolds rules apply:

$$\overline{\boldsymbol{B}_1 + \boldsymbol{B}_2} = \overline{\boldsymbol{B}}_1 + \overline{\boldsymbol{B}}_2, \quad \overline{\overline{\boldsymbol{B}}} = \overline{\boldsymbol{B}}, \quad \overline{\boldsymbol{b}} = 0 \tag{18}$$

$$\overline{\overline{\boldsymbol{B}}_1 \overline{\boldsymbol{B}}_2} = \overline{\boldsymbol{B}}_1 \overline{\boldsymbol{B}}_2, \quad \overline{\partial_\mu \boldsymbol{B}} = \partial_\mu \overline{\boldsymbol{B}}, \qquad \mu = 0, 1, 2, 3. \tag{19}$$

Applying the mean-field approach to our MHD equations yields two evolution equations for the magnetic field:

$$\partial_t \overline{\boldsymbol{B}} = \eta \nabla^2 \overline{\boldsymbol{B}} + \boldsymbol{\nabla} \times (\overline{\boldsymbol{U}} \times \overline{\boldsymbol{B}} + \overline{\boldsymbol{\mathcal{E}}}), \quad \boldsymbol{\nabla} \cdot \overline{\boldsymbol{B}} = 0 \tag{20}$$

$$\eta \nabla^2 \boldsymbol{b} + \boldsymbol{\nabla} \times (\overline{\boldsymbol{U}} \times \boldsymbol{b} + \boldsymbol{G}) - \partial_t \boldsymbol{b} = -\boldsymbol{\nabla} \times (\boldsymbol{u} \times \overline{\boldsymbol{B}}), \quad \boldsymbol{\nabla} \cdot \boldsymbol{b} = 0, \tag{21}$$

with the electromotive force (emf)

$$\boldsymbol{\mathcal{E}} \;=\; \boldsymbol{u} \times \boldsymbol{b} \tag{22}$$

and

$$\boldsymbol{G} = \boldsymbol{u} \times \boldsymbol{b} - \overline{\boldsymbol{u} \times \boldsymbol{b}}. \tag{23}$$

The electromotive force is assumed to be linear and homogeneous in $\boldsymbol{B}$ and its general form can be represented by the convolution

$$\begin{aligned} \boldsymbol{\mathcal{E}}_i(\boldsymbol{x}, t) \;&=\; \boldsymbol{\mathcal{E}}_i^{(0)}(\boldsymbol{x}, t) + \\ &\int\int K_{ij}(\boldsymbol{x}, \boldsymbol{x}', t, t') \overline{B}_j(\boldsymbol{x} - \boldsymbol{x}', t - t') \; \mathrm{d}^3 x' \; \mathrm{d}t', \end{aligned} \tag{24}$$

where the Einstein summation convention over double indices is applied. To make things simpler one takes the Taylor expansion of the magnetic field

$$\overline{B}_j(\boldsymbol{x}', t) \;=\; \overline{B}_j(\boldsymbol{x}, t) + (x_k' - x_k) \frac{\partial \overline{B}_j(\boldsymbol{x}, t)}{\partial x_k} + \ldots \tag{25}$$

and assumes a local and instantaneous dependence of the emf on the magnetic field:

$$\mathcal{E}_i \;=\; \alpha_{ij} \overline{B}_j + b_{ijk} \frac{\partial \overline{B}_j}{\partial x_k} + \ldots, \tag{26}$$

with

$$a_{ij} \;=\; \int\int K_{ij}(\boldsymbol{x}, \boldsymbol{x}', t, t') \; \mathrm{d}^3 x' \; \mathrm{d}t' \tag{27}$$

$$b_{ijk} \;=\; \int\int K_{ij}(\boldsymbol{x}, \boldsymbol{x}', t, t')(x_k' - x_k) \; \mathrm{d}^3 x' \; \mathrm{d}t'. \tag{28}$$

By further assuming that there is no mean velocity field $\boldsymbol{U}$ and that $\boldsymbol{u}$ corresponds to homogeneous and isotropic turbulence the emf reduces to the simple form

$$\boldsymbol{\mathcal{E}} = \alpha\overline{\boldsymbol{B}} - \eta_\mathrm{t}\boldsymbol{\nabla}\times\overline{\boldsymbol{B}} \tag{29}$$

$$a_{ij} = \alpha\delta_{ij} \tag{30}$$

$$b_{ijk} = \eta_\mathrm{t}\epsilon_{ijk}. \tag{31}$$

2.5 α^2 Mean-Field Dynamo

In mean-field theory the crucial quantity is the α term of (27) that describes the effect of small-scale turbulent velocity and magnetic field correlations on the mean-field. In the absence of any mean velocity field $\overline{\boldsymbol{U}}$ and under the assumption of isotropy, only α is responsible for the creation of large scale fields. The induction equation for that case reads

$$\frac{\partial\overline{\boldsymbol{B}}}{\partial t} = \alpha\boldsymbol{\nabla}\times\overline{\boldsymbol{B}} + \eta_\mathrm{T}\nabla^2\overline{\boldsymbol{B}}, \tag{32}$$

where $\boldsymbol{\nabla}\cdot\overline{\boldsymbol{B}} = 0$ and $\eta_\mathrm{T} = \eta + \eta_\mathrm{t}$ is the sum of the magnetic diffusivity η and turbulent diffusivity η_t. One is interested in how different modes of $\overline{\boldsymbol{B}}$ increase in time and look for solutions of the form

$$\overline{\boldsymbol{B}}(t) = \Re(\hat{\boldsymbol{B}}(k)\exp(i\boldsymbol{k}\cdot\boldsymbol{x} + \lambda t)). \tag{33}$$

To solve (32), $\hat{\boldsymbol{B}}(k)$ has to be solved by the eigenvalue equation [Moffatt, H. K., 1978, Krause and Raedler, 1980]

$$\lambda\hat{\boldsymbol{B}}(k) = \begin{pmatrix} -\eta_\mathrm{T}k^2 & -\mathrm{i}\alpha k_z & \mathrm{i}\alpha k_y \\ \mathrm{i}\alpha k_z & -\eta_\mathrm{T}k^2 & -\mathrm{i}\alpha k_x \\ -\mathrm{i}\alpha k_y & \mathrm{i}\alpha k_x & -\eta_\mathrm{T}k^2 \end{pmatrix}\hat{\boldsymbol{B}}(k), \tag{34}$$

which leads to the growth rates λ

$$\lambda_0 = -\eta_\mathrm{T}k^2, \quad \lambda_\pm = -\eta_\mathrm{T}k^2 \pm |\alpha k|. \tag{35}$$

Depending on the values of α and η_T, different modes are growing or decaying. By increasing α more large scale fields grow. By adding a mean velocity to (32) one obtains the mean-field induction equation for the $\alpha\omega$ mean-field dynamo.

2.6 $\alpha\omega$ Mean-Field Dynamo

The $\alpha\omega$ dynamo works with the help of shear, which can be due to differential rotation in stratified rotating objects. Shear is mediated via a mean flow of the form, e.g.

$$\overline{\boldsymbol{U}} = \begin{pmatrix} 0 \\ Sx \\ 0 \end{pmatrix}, \tag{36}$$

where S is the strength of the shear and x the x-coordinate. Seeking solutions of the form (33) which are axisymmetric ($k_y = 0$) leads to the eigenvalue problem

$$\lambda \boldsymbol{B}(k) = \begin{pmatrix} -\eta_{\rm T} k^2 & -{\rm i}\alpha k_z & 0 \\ {\rm i}\alpha k_z + S & -\eta_{\rm T} k^2 & -{\rm i}\alpha k_x \\ 0 & {\rm i}\alpha k_x & -\eta_{\rm T} k^2 \end{pmatrix}, \tag{37}$$

which has the eigenvalues

$$\lambda_0 = -\eta_{\rm T} k^2, \quad \lambda_\pm = -\eta_{\rm T} k^2 \pm \left(\alpha^2 k^2 - i\alpha S k_z\right)^{1/2}. \tag{38}$$

The real values of the λ are the actual growth rates. In the limit of $S \gg \alpha k_z$ it is

$$\Re(\lambda_\pm) \approx -\eta_{\rm T} k^2 \pm \left|\frac{1}{2}\alpha S k_z\right|^{1/2}, \tag{39}$$

with the frequency

$$\left|\frac{1}{2}\alpha S k_z\right|^{1/2}. \tag{40}$$

2.7 Saturation Phenomenology

The α-effect in mean-field theory is responsible for an exponential growth of the magnetic field energy. This growth happens in the linear regime. As the magnetic field grows, non-linear terms become more important, particularly the Lorentz force $\boldsymbol{J} \times \boldsymbol{B}$. Since all physical dynamos run into saturation (see Fig. 4 for simulation results) it was proposed that the magnetic field energy reduces the value of α such that the dynamo becomes marginally excited and saturates. A heuristic quenching formalism has been proposed to be [Ivanova and Ruzmaikin, 1977]:

$$\alpha = \frac{\alpha_0}{1 + \overline{\boldsymbol{B}}^2 / B_{\rm eq}^2}, \tag{41}$$

with the mean magnetic energy $\overline{\boldsymbol{B}}^2$ and the equipartition magnetic energy $B_{\rm eq}^2$. This model has the drawback that the value of α still is half of its initial value when the magnetic field is in equipartition which may not be correct. An improved relation was suggested by [Vainshtein and Cattaneo, 1992], which includes the magnetic Reynolds number:

$$\alpha \;=\; \frac{\alpha_0}{1+{\rm Re}_{\rm M}\overline{\boldsymbol{B}}^2/B_{\rm eq}^2}. \tag{42}$$

The $1/{\rm Re}_{\rm M}$ dependence of α is known as catastrophic quenching since for the Sun ${\rm Re}_{\rm M} = 10^9$ and the Galaxy ${\rm Re}_{\rm M} = 10^{29}$ and so $\alpha/\alpha_0 \ll 1$. In a later work [Cattaneo and Hughes, 1996] simulations confirmed equation (42) extremely well (Fig. 5).

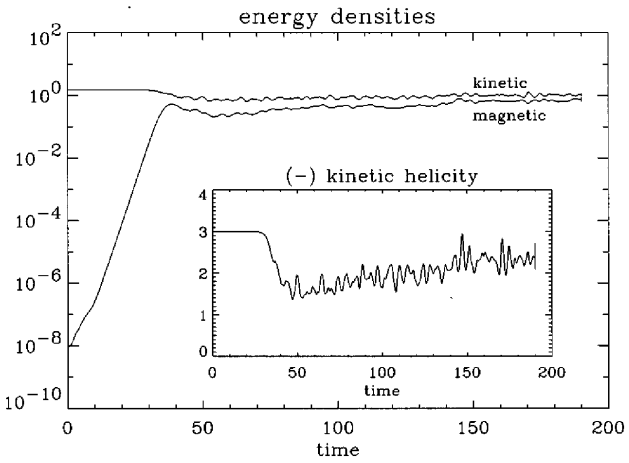

Figure 4: Time evolution of the kinetic and magnetic energies and kinetic helicity for ${\rm Re}_{\rm M} = {\rm Re} = 100$ [Cattaneo and Hughes, 1996]. The magnetic energy increases in the kinematic phase exponentially and saturates close to equipartition values.

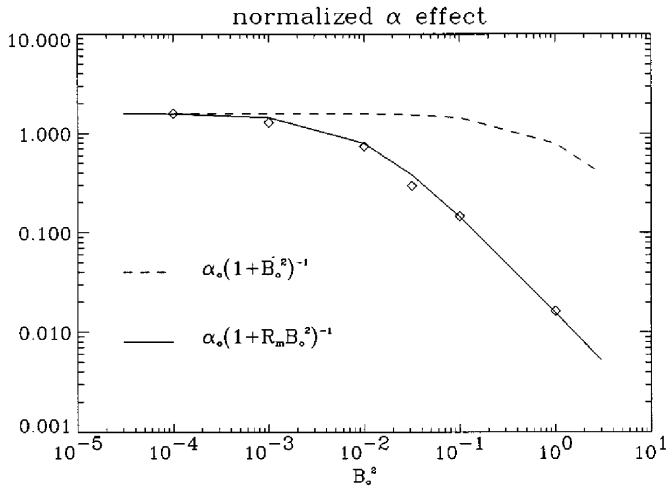

Figure 5: Normalized α as function of $\boldsymbol{B}_0^2$ [Cattaneo and Hughes, 1996], where $\boldsymbol{B}_0$ is the initial mean magnetic field. The simulation values are represented as diamonds, the model for equation (41) is the dashed line and for equation (42) is the solid line.

Another contribution to the saturation characteristics comes from the boundary conditions. Taking magnetic helicity conservation into account in a periodic box the saturation level of the magnetic energy behaves like $\mathrm{Re}_\mathrm{M}^{-1}$ and grows on resistive time scales rather than on dynamical scales, which is needed for a dynamo [Brandenburg, 2001]. In the same year it was found that by increasing Re_M a higher fraction of the magnetic energy is stored in smaller scales [Brandenburg and Dobler, 2001] with a dependence of $\langle\overline{\boldsymbol{B}}^2\rangle/\langle\boldsymbol{B}^2\rangle \propto \mathrm{Re}_\mathrm{M}^{-1/2}$ (Fig. 6). This result was however challenged in a later work [Brandenburg and Subramanian, 2005b], where a $\mathrm{Re}_\mathrm{M}^{-1}$ dependence was found.

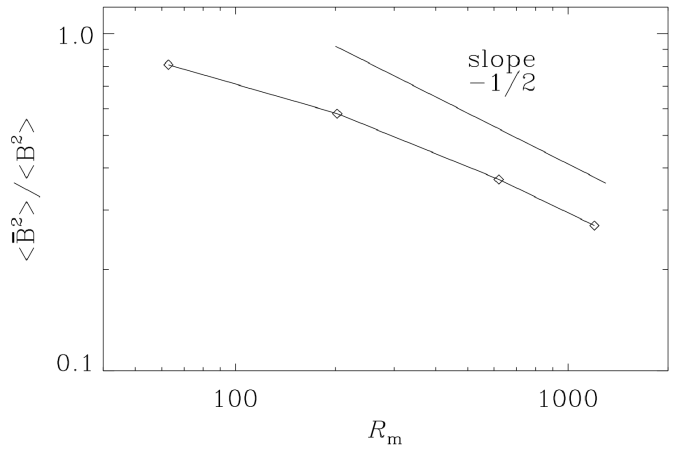

Figure 6: Mean magnetic energy to the total magnetic energy versus magnetic Reynolds number [Brandenburg and Dobler, 2001].

3 Observations

One of the most prominent activities of the Sun, which can be observed with a chronograph in the visible spectrum and x-ray, are coronal mass ejections (CMEs) (Fig. 7). They have an average[4] mass of $1.6 \cdot 10^{12}$kg and velocities between 20 and 3200 km/s.

[4]SOHO/LASCO measurements between 1996 and 2003

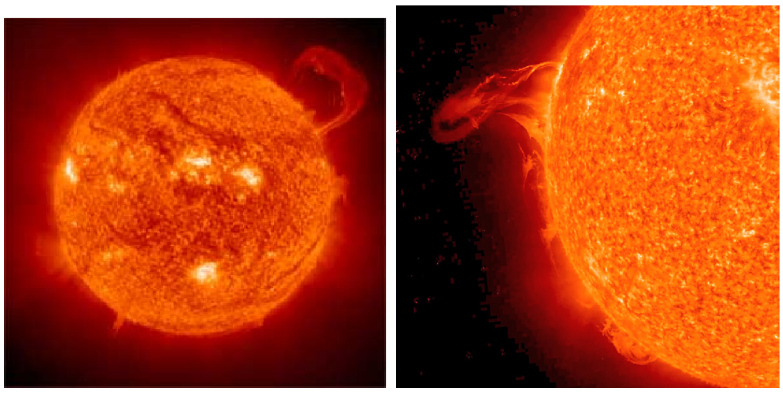

Figure 7: Coronal mass ejections as observed by SOHO. The right picture was taken in 7 May 2010.

Observations of the Sun using vector magnetograms with soft X-rays have shown [Pevtsov et al., 1996] that the magnetic field at the Sun's active regions is chiral and hence helical. In the same work it was demonstrated that reconnection of magnetic field lines occur amongst regions with same chirality. From Hα and X-ray observation in the chromosphere and the corona [Leka et al., 1996] it was conjectured that the flux bundles which make up the sunspots are twisted before they emerge (Fig. 8).

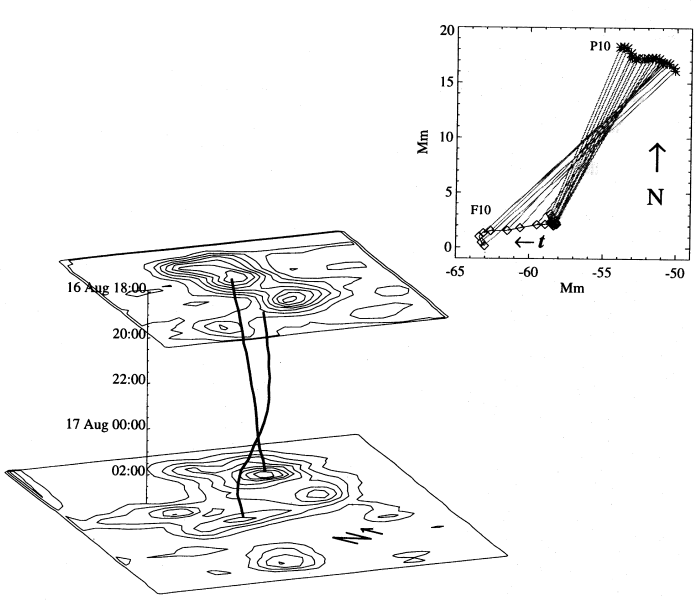

FIG. 3*a*

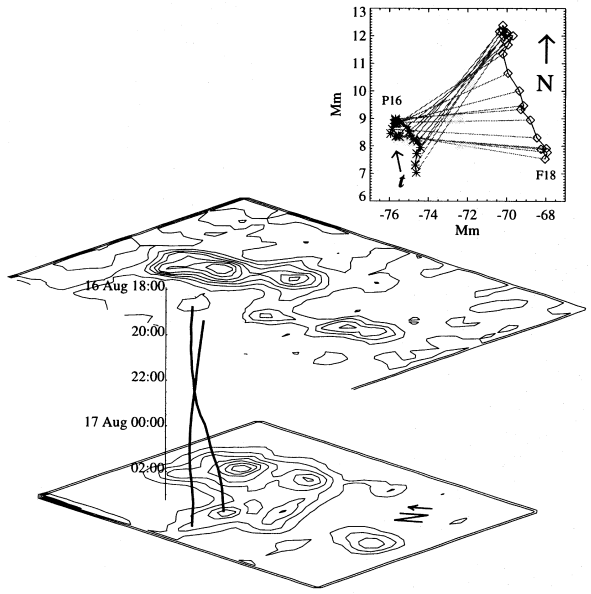

FIG. 3*b*

Figure 8: Two magnetic bipole observations for an interval of 9 hours with $\Delta t = 20\text{min}$. The solid lines indicate the position of the bipole on the Sun's surface at different times. The insets show the position of the bipoles on the surface for different times. [Leka et al., 1996]

The group of [Canfield et al., 1997] used magnetograms to compute the chirality α of the magnetic fields [5]. This was done by assuming a force-free field, i.e. $\nabla \times \boldsymbol{B} = \alpha \boldsymbol{B} = \boldsymbol{J}$, and making a fit for α. In the same work it was also shown that the chirality, which contributes to the magnetic helicity, is not changed after reconnection of active regions. Force-free magnetic fields could be shown to be approximately present only at a height of 400 km above the photosphere [Metcalf et al., 1995]. In a subsequent work [Canfield and Pevtsov, 1998], chiral magnetic field observations were interpreted to originate below the photosphere in the convection zone or at the bottom of the convection zone.

It was shown [Manoharan et al., 1996] that those S-shaped regions are precursors of coronal mass ejections and later [Canfield et al., 1999] that those regions are more likely to erupt. This could suggest that helicity is shed via CMEs.

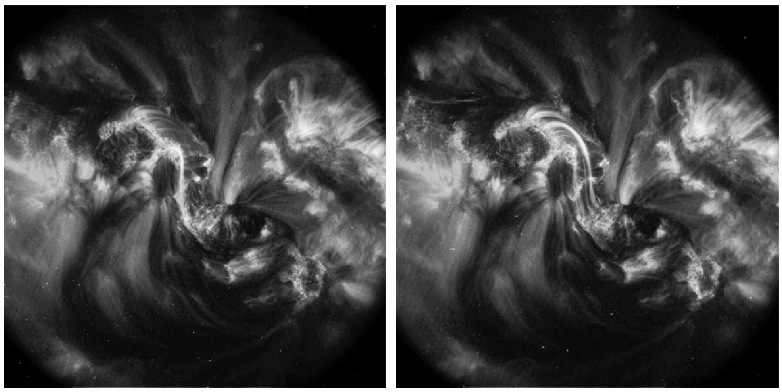

Figure 9: 195$\mathring{A}$ emission on 1999, August 21 at 18:26 UT (left) and 18:51 UT (right) [Gibson et al., 2002].

[Gibson et al., 2002] could reconstruct the field lines in the photosphere from observations (Fig. 9). It was demonstrated that the field lines show twisting (Fig. 10). Considering the previous works one is tempted to make the assumption that twisted regions are more likely to be shed.

[5] This α is not to be confused with the alpha tensor from the mean-field dynamo.

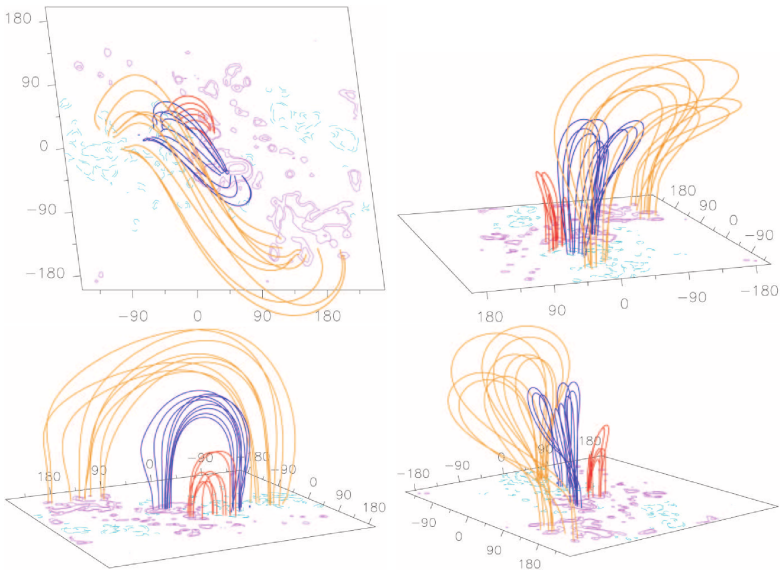

Figure 10: Force-free extrapolation of the photospheric magnetic field from 1999, August 21 [Gibson et al., 2002].

4 Magnetic Helicity

The magnetic helicity is defined as

$$H_{\mathrm{m}} \quad = \quad \int_V \boldsymbol{A} \cdot \boldsymbol{B} \, \mathrm{d}V, \tag{43}$$

where $\boldsymbol{B} = \boldsymbol{\nabla} \times \boldsymbol{A}$ is the magnetic field expressed in terms of the magnetic vector potential $\boldsymbol{A}$. The integral is taken over the volume. This quantity is in general gauge dependent. If the boundary conditions are chosen to be such that the normal component of the magnetic field vanishes or that the volume is infinite and $\boldsymbol{B}$ decreases quickly enough then H_{m} is gauge independent. The quantity $h = \boldsymbol{A} \cdot \boldsymbol{B}$ is called the magnetic helicity density which is always gauge dependent.

Magnetic helicity directly affects the dynamical evolution of the system. The *realizability condition* [Moffatt, H. K., 1978] defines a lower bound for the spectral magnetic energy $E_{\mathrm{m}}(k)$ in presence of magnetic helicity:

$$E_{\mathrm{m}}(k) \quad \geq \quad k|H(k)|/2\mu_0, \tag{44}$$

where k is the wave number corresponding to the inverse length of the scale and

$$E_{\mathrm{m}}(k) = \int_{k-\delta k/2}^{k+\delta k/2} |\hat{\boldsymbol{B}}(\boldsymbol{k})|^2 \, \mathrm{d}^3k, \qquad H(k) = \int_{k-\delta k/2}^{k+\delta k/2} |\hat{\boldsymbol{A}}(\boldsymbol{k}) \cdot \hat{\boldsymbol{B}}(\boldsymbol{k})| \, \mathrm{d}^3k \tag{45}$$

$$\hat{\boldsymbol{A}}(\boldsymbol{k}) = \int \boldsymbol{A}(\boldsymbol{x}) e^{-i\mathbf{k}\boldsymbol{x}} \, \mathrm{d}^3x, \qquad \hat{\boldsymbol{B}}(\boldsymbol{k}) = \int \boldsymbol{B}(\boldsymbol{x}) e^{-i\mathbf{k}\boldsymbol{x}} \, \mathrm{d}^3x. \tag{46}$$

Note that the magnetic energy at each wave length is bound which restricts conversions of energy stored in large-scale fields to energy stored in small-scale fields and vice versa. A derivation of the realizability condition is presented in appendix C

It was also shown [Chandrasekhar and Woltjer, 1958] that the magnetic helicity is a conserved quantity in a perfectly conducting fluid. Before that [Woltjer, 1958a] showed that for conserved helicity the configuration of lowest energy is such that the magnetic field is force-free (Lorentz force $\boldsymbol{F}_{\mathrm{L}} = \boldsymbol{J} \times \boldsymbol{B} = \boldsymbol{0}$). For low magnetic resistivities this implies that the magnetic field can only decay on resistive time scales. This has been used in Tokamak experiments [Brown and Bellan, 1992] to study plasma stability.

Helical magnetic configurations can be twisted flux tubes, knots and interlocked flux tubes (see Fig. 11).

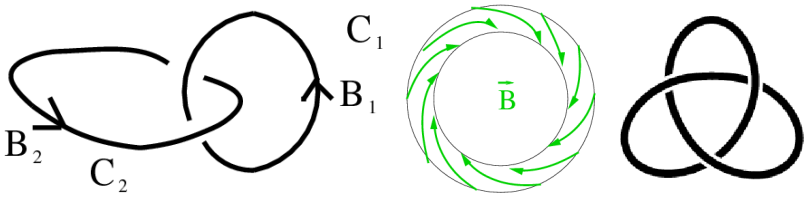

Figure 11: *Left*: Two interlocked flux rings which make up a helical configuration. *Center*: Magnetic flux ring which has a twisted magnetic field and finite helicity. *Right*: The trefoil knot [Moffatt, 1969]. With a magnetic field tangential to the knot the helicity of the configuration is finite.

Differential rotation may give rise to helical magnetic structures [Moffatt, H. K., 1978]. Also the stretch-twist-fold [Childress and Gilbert, 1995, p. 24] mechanism together with reconnection is believed to lead to magnetic field configurations which are helical. By measuring the Hα line and using vector magnetograms it was shown [Gary et al., 1987] that the active regions in

the Sun have a twisted magnetic field. This implies that also the solar flares have a twisted, hence helical field.

One of the earliest works in which the role of magnetic helicity was investigated was [Léorat et al., 1975]. There they used the eddy-damped quasi normal markovianized approximation (EDQNM) as proposed in [Orszag, 1970] and assumed homogeneity and isotropy. The purpose of this work was to study a saturation mechanism which counteracts the exponential increase of the magnetic energy during the linear phase. As driving mechanism they inject energy with the spectrum shown in (Fig. 12) as dotted lines. They find an increasing and then saturating magnetic energy (Fig. 13), which cascades to larger wave numbers where it is dissipated into heat.

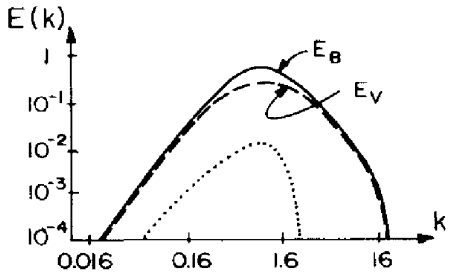

Figure 12: Magnetic (E_B) and kinetic (E_V) energy spectrum after some evolution in time. The dotted line represents the injected energy spectrum. In this run neither kinetic nor magnetic helicity was injected [Léorat et al., 1975].

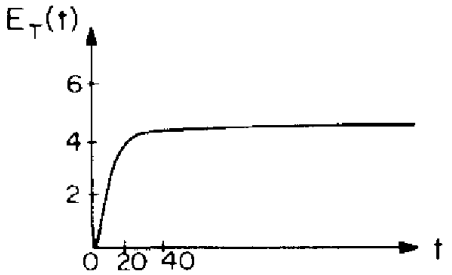

Figure 13: Evolution of the total energy E_T in time [Léorat et al., 1975].

In order to see how magnetic helicity evolves, the same group considered a setup with injected magnetic helicity. There $H_{\rm m}$ evolves to larger structures (inverse cascade) (Fig. 14).

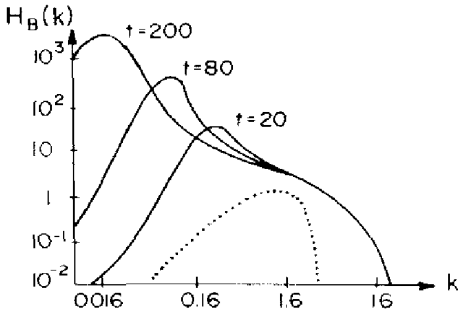

Figure 14: Magnetic helicity spectrum at different times. The dotted line represents the injected helicity [Léorat et al., 1975].

4.1 Topological Aspects of Magnetic Helicity

Magnetic helicity is strongly related to the topology of the magnetic field configuration. It was shown by [Moffatt, 1969] that the magnetic helicity of linked flux tubes is proportional to their linking number. Gauss found that the mutual linking number α_{ij} of two linked curves i and j in 3d space can be computed by the line integrals over the curves C_i and C_j

$$\alpha_{ij} = \frac{1}{4\pi} \oint_{C_i} \oint_{C_j} \frac{\mathbf{R}(d\mathbf{l}_i \times d\mathbf{l}_j)}{R^3}, \tag{47}$$

where $\mathbf{R} = \mathbf{l}_i - \mathbf{l}_j$. The connection to magnetic helicity was established by [Moffatt, 1969] where he considered separate magnetic flux tubes which do not intersect, are not self interlocked (knotted) and have constant magnetic flux ϕ_i. The mutual linking number of tube i with tube j is given as [Moreau, 1961, Moffatt, 1969]

$$\int_V \boldsymbol{A}_i \cdot \boldsymbol{B}_j \, \mathrm{d}V = 2\alpha_{ij}\phi_i\phi_j, \tag{48}$$

where ϕ_i is the magnetic flux through the cross section of a magnetic flux tube. By using Moffatt's [Moffatt, 1969] decomposition one can also define a linking number for single knots. One has to decompose such a knot into

several rings (Fig. 15) and apply equation (48). By doing so one of the two separate curves gets an internal twist which by itself contributes to the total helicity.

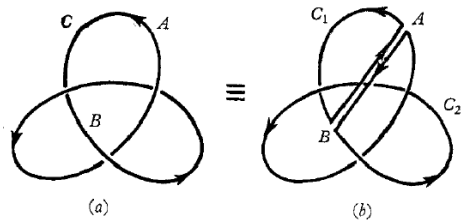

Figure 15: Decomposition of a trefoil knot [Moffatt, 1969]. Splitting the curve at the points A and B and inserting lines of opposite flux one obtains two rings which are interlinked. Note that for flux tubes the curve C_2 would obtain an internal twist.

4.2 Magnetic Helicity at High Magnetic Reynolds Numbers

The evolution equation for the magnetic helicity density reads

$$\frac{\partial h}{\partial t} = -2\eta \boldsymbol{J} \cdot \boldsymbol{B} - \boldsymbol{\nabla} \cdot \boldsymbol{F}, \tag{49}$$

where $\boldsymbol{F}$ is the magnetic helicity flux which, in the advective gauge (**Paper V**), reads

$$\boldsymbol{F} = h\boldsymbol{U} + \eta \boldsymbol{J} \times \boldsymbol{A}. \tag{50}$$

The first term on the RHS of (49) acts as a source term. For the case of ideal MHD (i.e. $\eta = 0$) the $\eta \boldsymbol{J} \cdot \boldsymbol{B}$ term vanishes and h behaves like a passive scalar which gets advected with the fluid and there is no net creation or destruction of magnetic helicity. Although not obvious, in the limit of $\eta \to 0$ the source term behaves the same way. This is best seen by first looking at the time evolution of the spatially averaged magnetic energy [Brandenburg and Käpylä, 2007]

$$\frac{1}{2}\frac{\partial}{\partial t}\langle \boldsymbol{B}^2 \rangle = -\langle \boldsymbol{U} \cdot (\boldsymbol{J} \times \boldsymbol{B}) \rangle - \eta \langle \boldsymbol{J}^2 \rangle, \tag{51}$$

where $\langle . \rangle$ denotes a volume average. For a statistically steady state, i.e. the space averages do not change in time, the current scales like

$$\boldsymbol{J} \propto \eta^{-1/2} \tag{52}$$

and hence

$$\eta\langle \boldsymbol{J}\cdot\boldsymbol{B}\rangle \to \eta^{1/2}, \tag{53}$$

which tends to 0 in the limit of $\eta \to 0$.

The scaling of the source term of magnetic helicity shows a fundamentally different behavior than the kinetic helicity, which has the space averaged time evolution equation [Brandenburg and Käpylä, 2007]

$$\frac{\partial}{\partial t}\langle \boldsymbol{U}\cdot\boldsymbol{W}\rangle = -2\eta\langle \boldsymbol{Q}\cdot\boldsymbol{W}\rangle + 2\langle \boldsymbol{W}\cdot\boldsymbol{\mathcal{F}}_{\rm ext}\rangle, \tag{54}$$

where $\boldsymbol{W} = \boldsymbol{\nabla}\times\boldsymbol{U}$ is the vorticity, $\boldsymbol{Q} = \boldsymbol{\nabla}\times\boldsymbol{W}$ and $\boldsymbol{\mathcal{F}}_{\rm ext}$ is an external forcing function. Again it is instructive to look at the evolution equation of the space averaged kinetic energy

$$\frac{1}{2}\frac{\partial}{\partial t}\langle \boldsymbol{U}^2\rangle = \langle \boldsymbol{U}\cdot\boldsymbol{\mathcal{F}}_{\rm ext}\rangle - \nu\langle \boldsymbol{W}^2\rangle. \tag{55}$$

Since the velocity does not change with ν $\boldsymbol{W}$ scales like

$$\boldsymbol{W} \propto \nu^{-1/2}. \tag{56}$$

The inverse length scale k, which is associated with the spatial derivative in Fourier space, scales like

$$k \propto \boldsymbol{W}/\boldsymbol{U} \propto \nu^{-1/2}, \tag{57}$$

so that $\boldsymbol{Q}$ scales like

$$\boldsymbol{Q} \propto \nu^{-1}, \tag{58}$$

and the source term for the kinetic helicity

$$\nu\langle \boldsymbol{Q}\cdot\boldsymbol{W}\rangle \propto \nu^{-1/2}. \tag{59}$$

The source term for the kinetic helicity tends to ∞ for low viscosities in contrast to the source term for the magnetic helicity which tends to 0 for low magnetic resistivities.

5 Magnetic Field Decay for Various Flux Tube Configurations

The presence of magnetic helicity slows down the decay of the magnetic energy due to the realizability condition (44). In a non-ideal fluid with

periodic or closed boundary conditions magnetic helicity can only decay on a resistive time scale [Berger, 1984] and so does then the magnetic energy.

A more descriptive way to clarify the role of magnetic helicity is by considering its topological interpretation as the linking number of magnetic flux tubes (see section 4.1 and Fig. 11). For a configuration of two flux tubes which are mutually interlocked magnetic energy can change either by decay, which would happen slowly on a resistive time scale, or by destroying the topology via reconnection which might be faster. In the limit of high magnetic Reynolds numbers only the latter will show any effect for sub-resistive times.

In **Paper I** and **Paper II** we address the role of topology in the decay of magnetic helicity and energy. One configuration consists of three interlocked flux rings where the magnetic field is oriented such that the total magnetic helicity is finite (second panel of Fig. 16). There is however a configuration with the same topology but vanishing helicity (first panel of Fig. 16), which we also consider in order to find whether it is the topology or merely the magnetic helicity which determines the time evolution of the magnetic field. A control set up is studied where the rings are not interlocked and the helicity vanishes (third panel of Fig. 16). Additionally we investigate a helical configuration which resembles a trefoil knot (fourth panel of Fig. 16).

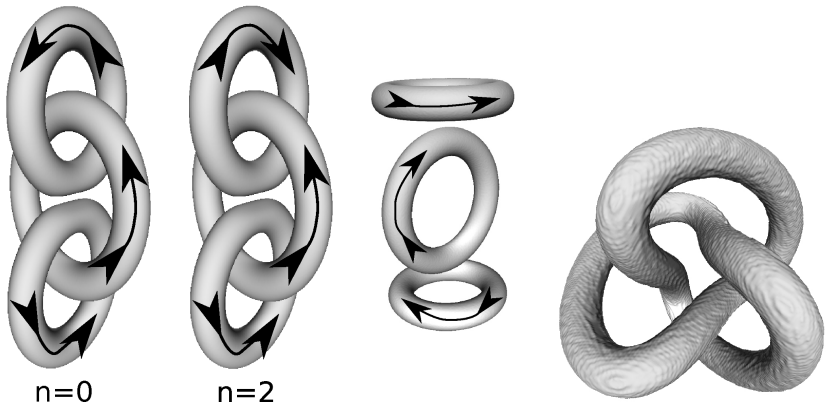

Figure 16: Initial magnetic flux configurations for the helical case (second panel), non-helical and linked case (first panel) and non-linked case (third panel), as well as for the trefoil knot (fourth panel).

In our simulations we solve the equations for a compressible isothermal

fluid with constant speed of sound and finite resistivities as governed by equations (7)–(9). The initial conditions are magnetic flux tubes with constant magnetic flux as shown in Fig. 16, where the radius of the inner ring is 1.2 times larger than the outer rings. The magnetic flux ϕ through each ring is however the same. In order to diminish resistive effects we choose $\nu = \eta = 10^{-4} R_0 c_\mathrm{s}$, where R_0 is the initial radius of the outer rings. All physical quantities are set to be periodic at the boundaries of the simulations cube of size 256^3 grid points. Periodic boundaries make sure that magnetic helicity is not shed via fluxes out of the domain. As a convenient time unit we choose the Alfvén time $T_\mathrm{A} = \sqrt{\mu_0 \rho_0} R_0^3 / \Phi$, with the initial density of the medium ρ_0 and initial magnetic flux through the tubes Φ, with which we write $\tau = t / T_\mathrm{A}$.

As projected by the realizability condition the magnetic energy decay is slower for the helical case than for the non-helical one (Fig. 17). The helical cases show an approximate decay power law of $t^{-1/3}$, while both non-helical setups show an approximate $t^{-3/2}$ decay. The decay of magnetic helicity occurs on a resistive time scale and due to the realizability condition also the magnetic energy decays at the same pace. The non-interlocked case shows the same decay characteristics as the interlocked, but non-helical case. This suggests that the actual topology plays at most only a minor role.

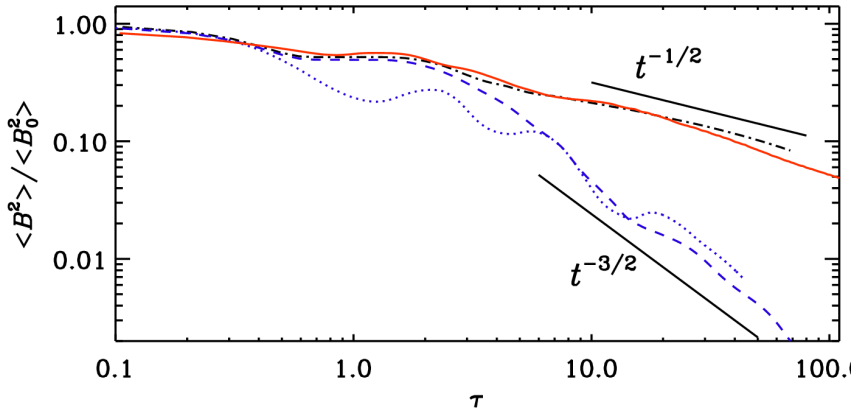

Figure 17: Decay of the normalized magnetic energy for the trefoil knot (solid/red line), helical ring configuration (dash-dotted line), zero helicity and linking (dashed/blue line) and zero helicity and no linking (dotted/blue line).

To get a grasp of the influence of the topology we plot the magnetic field lines for a time at which helical and non-helical cases differ by a factor of around 2 in energy which is at time $\tau = 4$ (Fig. 18). For the helical case the field of the outer rings reconnect with the inner ring which results in a twisted internal ring. This is due to helicity conservation, since twisting is topologically equivalent to linking. Reconnection also happens for the non-helical case where each outer ring induces a twist of opposite sign in the inner ring which results in no twist and the initial topology is lost.

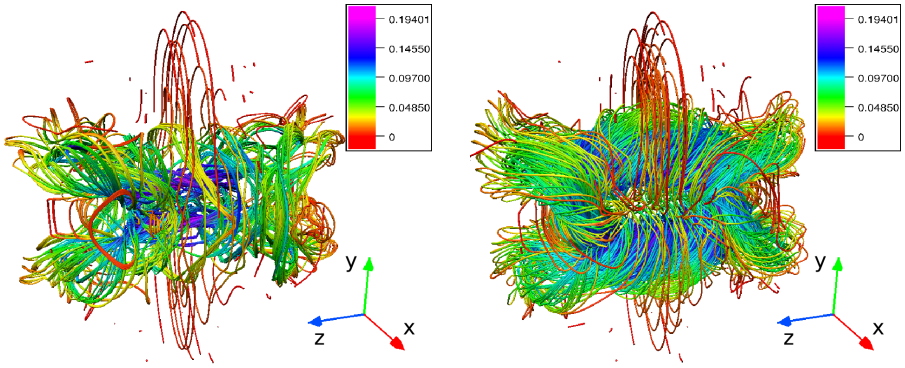

Figure 18: Streamlines of the magnetic field at time $\tau = 4$ for the initial configuration of three interlocked flux tubes. The zero helicity case (left) loses its topological structure while for the helical case (right) the linking gets transformed into twisting which is equivalent to linking.

The trefoil knot also keeps its topology after 5 Alfvén times (Fig. 19). In contrast to the helical ring configuration the linking is not transformed into internal twist.

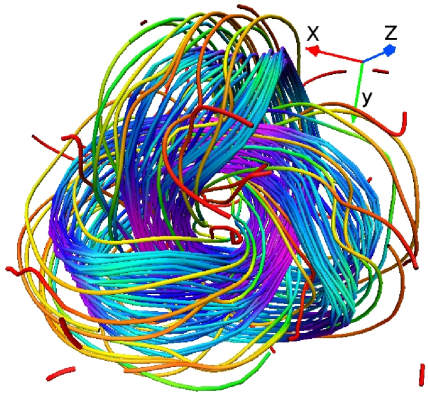

Figure 19: Magnetic field lines at $\tau = 5$ for the trefoil knot. The colors represent the magnitude of the magnetic field. Note that internal twist generation is weak.

In conclusion we can say that the actual topological structure does not play any significant role in the decay of magnetic fields. In the presence of magnetic helicity it is this quantity which determines the dynamical evolution of the magnetic energy. For entangled magnetic flux configurations which have vanishing magnetic helicity (i.e. $|\langle \boldsymbol{A} \cdot \boldsymbol{B} \rangle| / L \langle \boldsymbol{B}^2 \rangle \ll 1$, with L being a typical length of the system) we can predict with our results that there will be little to no difference in magnetic energy decay compared to the non-entangled case.

6 Effects of Magnetic Helicity Fluxes

It was proposed by [Blackman and Field, 2000a,Blackman and Field, 2000b] that the α quenching (see section 2.7) can be reduced by allowing magnetic helicity to leave the system through fluxes. Such fluxes could then allow for higher saturation magnetic fields and reduce the time for the system to reach saturation [Brandenburg and Dobler, 2001].

In **Paper III** the importance of small-scale magnetic helicity fluxes is shown in a numerical experiment for a one-dimensional mean-field dynamo. We use the mean-field approach in order to achieve large magnetic Reynolds numbers up to 10^5 which would not be attainable in three-dimensional simulations.

The evolution equations for the magnetic helicity density stored in the

large- and small-scale fields in mean-field theory are given by

$$\frac{\partial \overline{h}_{\rm m}}{\partial t} = 2\overline{\boldsymbol{\mathcal{E}}} \cdot \overline{\boldsymbol{B}} - 2\eta\mu_0 \overline{\boldsymbol{J}} \cdot \overline{\boldsymbol{B}} - \boldsymbol{\nabla} \cdot \overline{\boldsymbol{F}}_{\rm m} \tag{60}$$

$$\frac{\partial \overline{h}_{\rm f}}{\partial t} = -2\overline{\boldsymbol{\mathcal{E}}} \cdot \overline{\boldsymbol{B}} - 2\eta\mu_0 \overline{\boldsymbol{j} \cdot \boldsymbol{b}} - \boldsymbol{\nabla} \cdot \overline{\boldsymbol{F}}_{\rm f}, \tag{61}$$

where the indices m and f denote the mean and fluctuating fields respectively and the fluxes are given by

$$\overline{\boldsymbol{F}}_{\rm m} = \overline{\boldsymbol{E}} \times \overline{\boldsymbol{A}} + \overline{\Psi}\ \overline{\boldsymbol{B}}, \qquad \overline{\boldsymbol{F}}_{\rm f} = \overline{\boldsymbol{e} \times \boldsymbol{a}} + \overline{\psi b}, \tag{62}$$

with the electric potential $\Psi = \overline{\Psi} + \psi$. We use the following relation between the magnetic α and the helicity stored in the small-scale fields

$$\alpha_{\rm M} = -\frac{1}{3}\tau \overline{\boldsymbol{j} \cdot \boldsymbol{b}}/\overline{\rho}, \qquad \overline{\boldsymbol{j} \cdot \boldsymbol{b}} = k_{\rm f}^2 \overline{h}_{\rm f}, \tag{63}$$

where τ is the correlation time and $k_{\rm f}$ the wave vector of the helical forcing. The evolution equation for $\alpha_{\rm M}$ reads

$$\frac{\partial \alpha_{\rm M}}{\partial t} = -2\eta_{\rm t} k_{\rm f}^2 \left(\frac{\overline{\boldsymbol{\mathcal{E}}} \cdot \overline{\boldsymbol{B}}}{B_{\rm eq}^2} + \frac{\alpha_{\rm M}}{{\rm Re}_{\rm M}} \right) - \frac{\partial \overline{\mathcal{F}}_\alpha}{\partial z}, \tag{64}$$

where $\eta_{\rm t} = \frac{1}{3}\tau \overline{\boldsymbol{u}}^2$ is the turbulent diffusivity, $B_{\rm eq} = (\mu_0 \overline{\rho} \overline{\boldsymbol{u}^2})^{1/2}$ is the equipartition field strength and the magnetic α fluxes

$$\overline{\mathcal{F}}_\alpha = \overline{\boldsymbol{\mathcal{F}}}_{\alpha z}, \quad \overline{\mathcal{F}}_\alpha = \frac{\mu_0 \overline{\rho} \eta_{\rm t} k_{\rm f}^2}{B_{\rm eq}^2} \overline{\boldsymbol{F}}_{\rm f}. \tag{65}$$

The flux for the magnetic α is affected by advection, which might be due to galactic fountain flows or stellar wind, and a Fickian diffusion, so we write

$$\overline{\mathcal{F}}_\alpha = \alpha_{\rm M} \overline{U} - \kappa_\alpha \frac{\alpha_{\rm M}}{\partial z}, \tag{66}$$

where κ_α is the diffusion coefficient and $\overline{U}$ is the mean velocity field in z-direction. In order to create helicity fluxes we impose a wind which increases linearly with height, so we set $\overline{U} = U_0 z/H$, where the domain goes from $z = 0$ to $z = H$.

The crucial component in models with magnetic helicity fluxes are the boundary conditions for the magnetic field. In order to allow such fluxes there have to be vacuum boundary (vertical field) conditions at the top of the domain, i.e. $\overline{A}_{x,z} = \overline{A}_{y,z} = 0$. In contrast, closed or perfect conductor

conditions do not allow fluxes ($\overline{A}_x = \overline{A}_y = 0$). On the equator we can make an assumption about the parity of the field by adjusting the boundary conditions at $z = 0$. We choose the lower boundaries such that the magnetic field is symmetric ($\overline{A}_x = \overline{A}_y = 0$), or antisymmetric ($\overline{A}_{x,z} = \overline{A}_{y,z} = 0$).

The combination of vacuum conditions with symmetric field as well as perfect conductor with antisymmetric field leads to oscillating large scale fields close to equipartition values (Fig. 20). This means that both setups are able to create and sustain a large scale dynamo where catastrophic quenching can be removed. In both cases the field propagates towards the open boundary which allows for magnetic helicity fluxes.

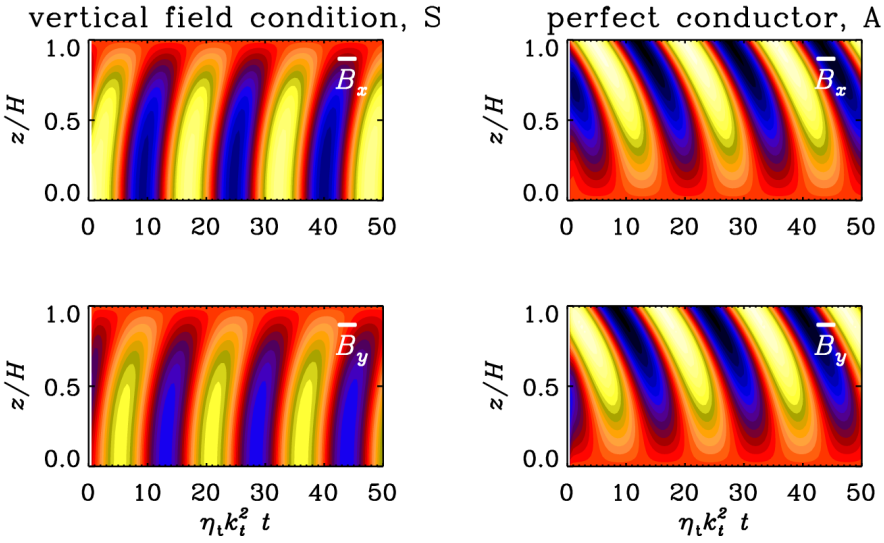

Figure 20: Space-time diagrams for B_x and B_y for a symmetric (S) field with vacuum boundary conditions and antisymmetric field (A) with perfect conductor boundary conditions.

We need the above boundary conditions because we find it is easier to excite the dynamo with them rather than vacuum with antisymmetric field or perfect conductor with symmetric field in absence of any wind.

Without any wind the saturation magnetic energy decreases as $\mathrm{Re}_\mathrm{M}^{-1}$ (Fig. 21) with increasing the magnetic Reynolds number Re_M. This quenching is however alleviated by imposing a wind which carries the magnetic helicity to the upper boundary where it can be shed in the case of vacuum boundary conditions.

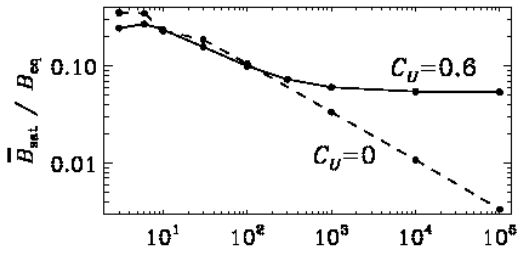

Figure 21: Saturation magnetic energy normalized for equipartition versus magnetic Reynolds number $\mathrm{Re_M}$ with advective helicity flux (solid line). Compare the case without the flux (dashed line). The catastrophic quenching gets alleviated by helicity fluxes.

In the case of perfect conductor boundaries there can be no magnetic helicity flux out of the domain. Therefore we impose a Fickian diffusive flux through the midplane (see equation (66)). This can also alleviate the α-quenching (Fig. 22).

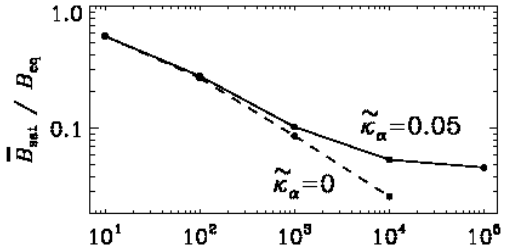

Figure 22: Saturation magnetic energy normalized for equipartition versus magnetic Reynolds number $\mathrm{Re_M}$ with diffusive helicity fluxes through the equator (solid line). Compare the case without the flux (dashed line). Also here the quenching gets alleviated.

Both the small- and large-scale components of magnetic helicity get shed at the boundaries. The sign of the fluxes are however different (Fig. 23) due to no net total magnetic helicity production.

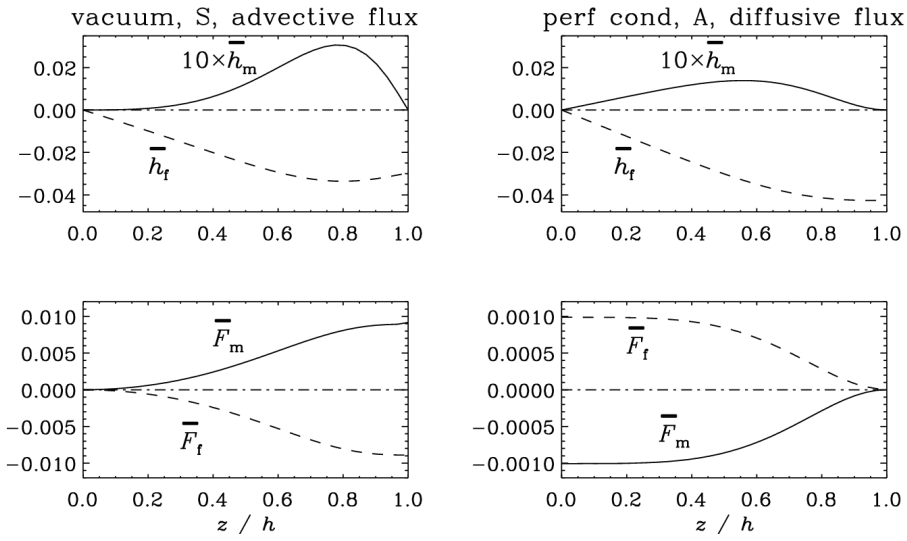

Figure 23: z-profile of the magnetic helicity density of the mean and fluctuating fields (upper panels) together with the z-profile of their fluxes (lower panels). For the A solution we allowed for a diffusive flux with $\kappa_\alpha = 0.05$.

7 Gauge Issues of Magnetic Helicity

The magnetic helicity density $h = \boldsymbol{A} \cdot \boldsymbol{B}$ is a quantity which depends on the gauge of $\boldsymbol{A}$. The gauge transformation $\boldsymbol{A} \rightarrow \boldsymbol{A} + \boldsymbol{\nabla}\Lambda$ adds the term $\boldsymbol{\nabla}\Lambda \cdot \boldsymbol{B}$ to h. Magnetic helicity $H_\mathrm{m} = \int_V \boldsymbol{A} \cdot \boldsymbol{B} \, \mathrm{d}V$ is generally also gauge dependent. However for certain boundary conditions it is gauge independent. Consider the gauge transformed magnetic helicity:

$$\begin{aligned} \int_V (\boldsymbol{A} + \boldsymbol{\nabla}\Lambda) \cdot \boldsymbol{B} \, \mathrm{d}V &= \int_V \boldsymbol{A} \cdot \boldsymbol{B} \, \mathrm{d}V + \int_V \boldsymbol{\nabla} \cdot (\Lambda \boldsymbol{B}) \, \mathrm{d}V \\ &= \int_V \boldsymbol{A} \cdot \boldsymbol{B} \, \mathrm{d}V + \int_S \Lambda \boldsymbol{B} \cdot \mathrm{d}\boldsymbol{S}, \end{aligned} \tag{67}$$

where the last term on the RHS is the surface integral with the normal vector $\boldsymbol{S}$. This means that for perfect conductor boundary conditions, periodic domains, or for magnetic fields vanishing at the surface, H_m is gauge independent.

Apart from the magnetic helicity density, also the helicity fluxes are gauge depended. Since helicity fluxes are crucial for dynamos (**Paper III**)

the question how different gauges can influence these fluxes is addressed in **Paper IV** and **Paper V**.

7.1 Equatorial Magnetic Helicity Flux with Different Gauges

The imposed Fickian diffusion for the magnetic helicity in **Paper III** was introduced ad hoc. It is of great importance to see if such a diffusive flux can occur by itself in 3d MHD simulations. Helicity fluxes are gauge dependent. However the alleviation of α-quenching through those fluxes is a physical effect. Therefore the question arises how the gauge choice modifies the diffusive fluxes.

In **Paper IV** we address these questions. We perform 3d MHD simulations for an isothermal compressible ideally conducting fluid as described by the equations (8), (9) and a modified form of (7)

$$\frac{\partial \boldsymbol{A}}{\partial t} = \boldsymbol{U} \times \boldsymbol{B} - \eta\mu_0 \boldsymbol{J} - \boldsymbol{\nabla}\Psi, \tag{68}$$

with the electrostatic potential Ψ. The domain is a a Cartesian box of size $128\times128\times256$ mesh points. We denote the long side as the z-direction where the midplane is at $z = 0$. The boundary conditions are chosen to be periodical in all physical quantities and we vary the magnetic Reynolds number $\mathrm{Re_M}$ between 6 and 68. As driving a helical forcing is imposed which changes sign at the midplane.

The time evolution of magnetic helicity is given by the sum of (60) and (61)

$$\frac{\partial h}{\partial t} = -2\boldsymbol{E}\cdot\boldsymbol{B} - \boldsymbol{\nabla}\cdot\boldsymbol{\mathcal{F}}, \tag{69}$$

where

$$\boldsymbol{\mathcal{F}} = \boldsymbol{E}\times\boldsymbol{A} + \Psi\boldsymbol{B} \tag{70}$$

is the magnetic helicity flux. We can distinguish large and small-scale helicities by applying the mean-field formalism and average over the xy-plane. Note that this is only done for diagnostics, the simulations are fully 3d DNS. The evolution for the mean magnetic helicity stored in the large and small-scale fields are given by (60) and (61), with their fluxes (62).

The gauges under consideration are the Weyl gauge, resistive gauge and pseudo-Lorenz gauge (i.e. $c \to c_s$). In the Weyl gauge the electrostatic potential $\Psi = 0$, while for the resistive gauge it takes the form $\Psi = \eta\boldsymbol{\nabla}\cdot\boldsymbol{A}$. The pseudo-Lorenz gauge is fixed by the time derivative of the electrostatic potential

$$\frac{\partial \Psi}{\partial t} = -c_s^2 \boldsymbol{\nabla}\cdot\boldsymbol{A}. \tag{71}$$

We want to confirm if in analogy to **Paper III** there is a Fickian diffusive flux of small-scale magnetic helicity through the midplane of the form

$$\overline{\boldsymbol{\mathcal{F}}}_{\rm f} = -\kappa_{\rm f} \boldsymbol{\nabla} \overline{h}_{\rm f}, \tag{72}$$

with the diffusion coefficient $\kappa_{\rm f}$ for the small-scale magnetic helicity density. This is done by simply measuring the gradient of $\overline{h}_{\rm f}$ at the midplane and take a xy-average.

To see the importance of each term in (61) we plot their time averaged z-profile (Fig. 24). The averaging is done in a statistically stationary state. The diffusion coefficient $\kappa_{\rm f}$ is computed by doing a lest-square fit. Fickian diffusion agrees quiet well for our calculations (Fig. 24 (lower panel)) There is a particularly good agreement at the midplane.

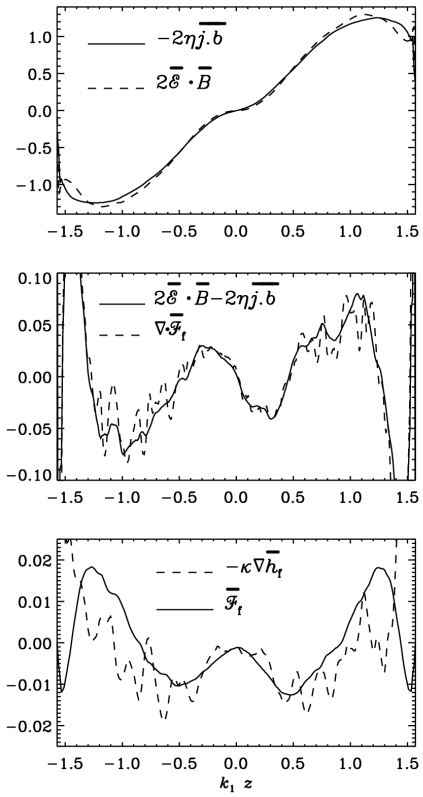

Figure 24: z-profile of the terms on the RHS of equation (61) for a selected run in resistive gauge (upper and middle panel). The lower panel shows the measured small-scale helicity flux together with the fitted Fickian diffusion profile.

In a statistically steady state $\overline{h}_\mathrm{f}$ fluctuates while a time average over a short period does not change in time. With this we can write the time averaged magnetic helicity flux in z-direction as

$$\frac{\partial\overline{\mathcal{F}}^z_\mathrm{f}}{\partial z} = -2\overline{\boldsymbol{\mathcal{E}}}\cdot\overline{\boldsymbol{B}} - 2\eta\overline{\boldsymbol{j}\cdot\boldsymbol{b}}. \tag{73}$$

Since there are only physical quantities present on the RHS the time averaged small-scale magnetic helicity flux in z-direction is also gauge independent. This we can also confirm in simulations for our three gauges (Fig. 25).

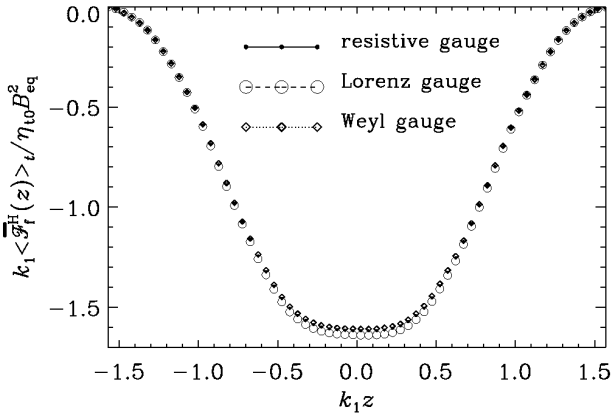

Figure 25: z-profile of the normalized and time averaged small-scale magnetic helicity flux for the three gauges.

7.2 Magnetic Helicity Transport in the Advective Gauge Family

Different helicity transport in different gauges will lead to different scales of helicity storage. This question is addressed in **Paper V** where a gauge is chosen in which the vector potential $\boldsymbol{A}$ appears as an advection term. This gauge is called advecto-resistive because the vector potential $\boldsymbol{A}$ appears as an advected and as a diffusive quantity. The induction equation

$$\frac{\partial \boldsymbol{B}}{\partial t} = \boldsymbol{\nabla} \times (\boldsymbol{U} \times \boldsymbol{B} - \eta \boldsymbol{J}) \tag{74}$$

is uncurled into

$$\frac{\partial \boldsymbol{A}}{\partial t} = \boldsymbol{U} \times \boldsymbol{B} - \eta \boldsymbol{J} - \boldsymbol{\nabla} \left(\boldsymbol{U} \cdot \boldsymbol{A} - \eta \boldsymbol{\nabla} \cdot \boldsymbol{A} \right), \tag{75}$$

which would reduce to the resistive gauge

$$\frac{\partial \boldsymbol{A}}{\partial t} = \boldsymbol{U} \times \boldsymbol{B} + \eta \nabla^2 \boldsymbol{A} \tag{76}$$

without the advection term $\boldsymbol{U} \cdot \boldsymbol{A}$ and the advective gauge without the resistive term $\eta \boldsymbol{\nabla} \cdot \boldsymbol{A}$. The evolution equation for the magnetic helicity in the advecto-resistive gauge is

$$\frac{\partial h^{\rm ar}}{\partial t} = -2\eta \boldsymbol{J} \cdot \boldsymbol{B} - \boldsymbol{\nabla} \cdot \boldsymbol{F}^{\rm ar}, \tag{77}$$

with the magnetic helicity flux

$$\boldsymbol{F}^{\mathrm{ar}} = h^{\mathrm{ar}}\boldsymbol{U} - \eta(\boldsymbol{\nabla}\cdot\boldsymbol{A}^{\mathrm{ar}})\boldsymbol{B} + \eta\boldsymbol{J}\times\boldsymbol{A}^{\mathrm{ar}}. \tag{78}$$

The evolution equations of the magnetic helicity in the resistive and advecto-resistive gauges differ only by the flux, which for the resistive gauge would read

$$\boldsymbol{F}^{\mathrm{r}} = h^{\mathrm{r}}\boldsymbol{U} - (\boldsymbol{U}\cdot\boldsymbol{A}^{\mathrm{r}} + \eta(\boldsymbol{\nabla}\cdot\boldsymbol{A}^{\mathrm{r}}))\boldsymbol{B} + \eta\boldsymbol{J}\times\boldsymbol{A}^{\mathrm{r}}. \tag{79}$$

Doing numerical simulation in the advecto-resistive gauge leads to difficulties. All the runs are numerically unstable. Considering the gauge transformation from the stable resistive gauge to the advecto-resistive gauge

$$\boldsymbol{A}^{\mathrm{ar}} = \boldsymbol{A}^{\mathrm{r}} + \boldsymbol{\nabla}\Lambda, \tag{80}$$

with the gauge field Λ, and the evolution equation for the magnetic vector potential

$$\frac{\mathrm{D}A_i^{\mathrm{ar}}}{\mathrm{D}t} = -U_{j,i}A_j^{\mathrm{ar}} + \eta\nabla^2 A_i^{\mathrm{ar}}, \tag{81}$$

it becomes clear that terms of the form $\boldsymbol{\nabla}\times(\boldsymbol{\nabla}\Lambda)$ come into play. Such terms are zero analytically, while numerically they are not due to numerical errors. The spurious contributions increase the current $\boldsymbol{J}$ artificially and so the Lorentz force and thereby the velocity.

To overcome this difficulty and still use the advecto-resistive gauge for the helicity transport the simulations are done in the intrinsically stable resistive gauge. In order to obtain the magnetic helicity in the advecto-resistive gauge we apply the gauge transformation (80). Λ obeys the evolution equation

$$\frac{\mathrm{D}\Lambda}{\mathrm{D}t} = -\boldsymbol{U}\cdot\boldsymbol{A} + \eta\nabla^2\Lambda. \tag{82}$$

Note that Λ has no effect on the vector potential $\boldsymbol{A}$. In **Paper V** this approach is called the "Λ method".

In order to test if the Λ method works we compare runs with this method against the direct advecto-resistive runs (Fig. 26). Both methods agree perfectly until the instability shows up.

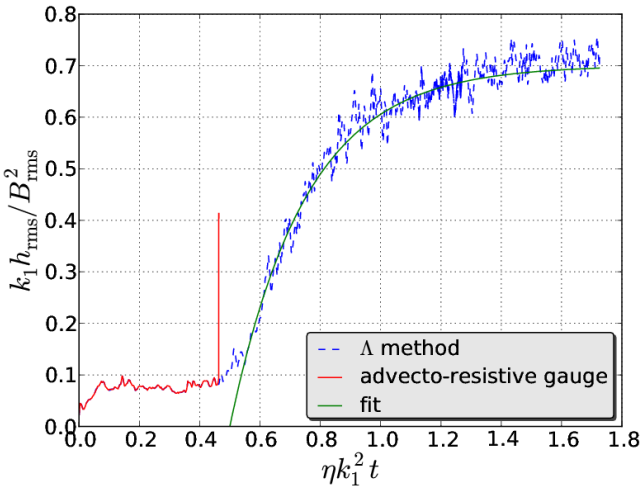

Figure 26: Normalized rms value of the magnetic helicity density in dependence of the diffusive time. Both methods match until the instability arises and the direct method stops. The fit is an exponential relaxation of the form $1 - \exp\left(-2\eta k_{\mathrm{m}}^2 (t - t_{\mathrm{sat}})\right)$, where $k_{\mathrm{m}} = 1.4 k_1$

In Fig. 27 we plot the power spectra of $\boldsymbol{A}$, $\boldsymbol{B}$ and $\boldsymbol{U}$ for a time instance shortly before the instability causes the simulation to stop. The errors are particularly well pronounced for small scales, i.e. high k, where the instability starts. Later this also affects the larger scales.

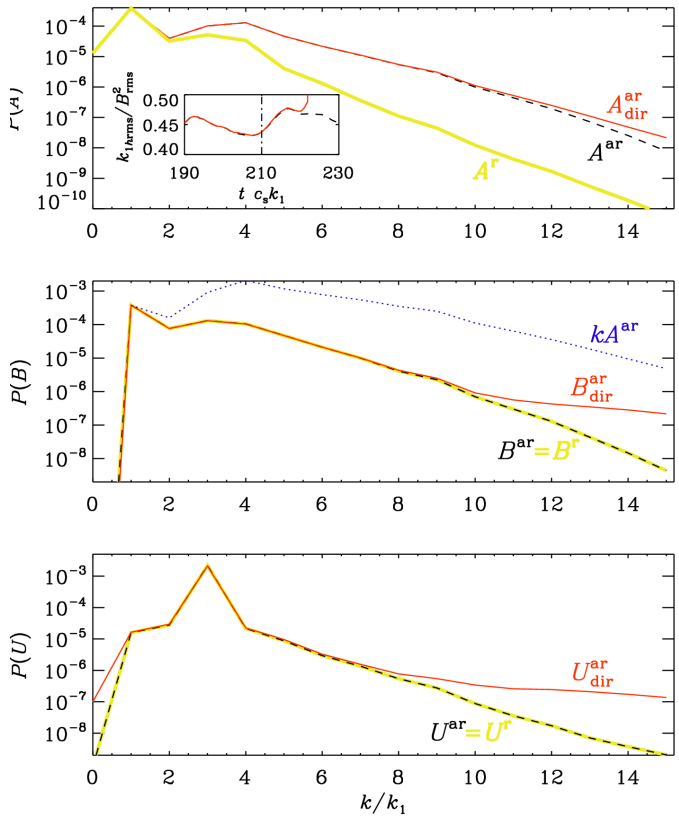

Figure 27: Power spectra for the fields $\boldsymbol{A}$, $\boldsymbol{B}$ and $\boldsymbol{U}$ for two runs of which one is done in the advecto-resistive gauge (subscript "dir") and the other with the Λ method (no subscript). The superscripts "ar" and "r" denote a quantity in the advecto-resistive and resistive gauge respectively. The spectra are taken at a time instance shortly before the instability (see inset of panel one). The physical fields in the simulation with the Λ method (thick solid and dashed lines) are well-behaved and don't change when we transform $\boldsymbol{A}$ numerically. The runs in the direct gauge (thin solid line) however show an increased high k tail which is particularly well pronounced for the velocity (lower panel) which eventually leads to the instability.

For high magnetic Reynolds numbers and in the kinematic regime the time evolution equation for the magnetic helicity reduces to the one for a passive scalar C

$$\frac{\mathrm{D}C}{\mathrm{D}t} = \kappa \nabla^2 C, \tag{83}$$

with the diffusivity of the passive scalar κ. We compare the behavior of the magnetic helicity density with the passive scalar by imposing a linear gradient for C and solve for (83) together with the MHD equations with the Λ method (Fig. 28). For low k the spectrum for $h^{\rm ar}$ and C in the kinematic regime show the same Kazantsev like power law of $k^{3/2}$, while the spectrum of $h^{\rm r}$ shows a steeper slope. For higher k both c and $h^{\rm ar}$ show similar power laws. In the non-linear regime the passive scalar shows a Kazantsev like power law of $-5/3$ which agrees with $h^{\rm r}$. This we attribute to the velocity term in (79) which creates more spatial variations for $h^{\rm r}$. Computing $\boldsymbol{A}$ in this gauge leads to a strong high k tail for the root mean square (rms) value of the magnetic helicity in the advecto-resistive gauge. This becomes even more pronounced in the saturation phase which is attributed to the ability of any advective gauge to make the helicity efficiently cascade into scales of the small-scale eddies.

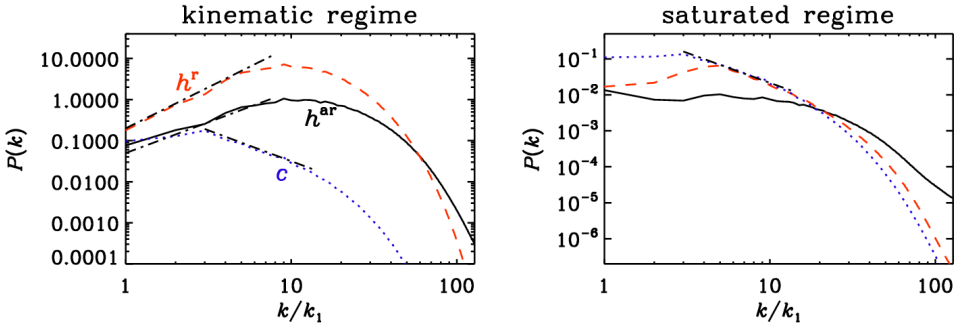

Figure 28: Power spectra of the magnetic helicity in the resistive ($h^{\rm r}$) and advecto-resistive gauge ($h^{\rm ar}$) together with the spectrum of a passive scalar (c) in the kinematic regime (left) and saturated regime (right) for $\mathrm{Re_M} = 80$ and $\mathrm{Pr_M} = 1$.

Conclusively we can say that in the advecto-resistive gauge the magnetic helicity behaves like a passive scalar for high $\mathrm{Re_M}$ in the kinematic regime. In the saturated regime it shows strong small-scale structures which we attribute to the ability of the advecto-resistive gauge to transport magnetic helicity into scales of the small-scale eddies. Another take home message is that the use of a gauge transformation of the form of (80) together with an evolution equation of the form of (82) can be used to compute gauge dependent quantities in a numerically unstable gauge.

8 Outlook

8.1 Magnetic Helicity Fluxes

Depending on the boundary conditions, the dynamos get more or less easily excited. It would however be beneficial to test if also stable solutions of mixed parity can occur with dynamical α quenching. Such studies were originally done for simple α quenching as it is described in (41) [Brandenburg et al., 1989].

The role of diffusive magnetic helicity fluxes studied in **Paper III** has also been considered in [Guerrero et al., 2010, Chatterjee et al., 2010, Chatterjee et al., 2011]. The setups however were idealized and did not consider the types of inhomogeneities that are present in physical systems like the Sun. Therefore setups with strong stratification should be considered in future works.

In **Paper III** and **Paper IV** the parameters were chosen such that the magnetic Prandtl number was of order unity. This is however not true for the Sun where $\mathrm{Pr_M} = 10^{-5}$, for which small-scale dynamo action is suppressed. The parameter range for which dynamo action occurs will change if we add shear to the system. This should facilitate the growth of large-scale magnetic fields of equipartition strength. Such investigations have already been started **Paper A** and are being followed up for a full paper.

A remarkable possibility of small-scale magnetic helicity fluxes was discussed by [Vishniac and Cho, 2001]. In the presence of a mean velocity field there can be helicity fluxes along sheets of constant shear. This theory has been derived analytically for low magnetic Reynolds numbers. It was however challenged if such helicity fluxes actually exist [Hubbard and Brandenburg, 2011] and only non-vanishing turbulent diffusive magnetic helicity fluxes were found. It is of interest to study whether modifications of this theory hold and how it behaves at high magnetic Reynolds numbers, which is the interesting regime for astrophysics. As an auxiliary tool, mean-field theory is a good candidate which makes high $\mathrm{Re_M}$ tangible.

8.2 Higher Order Topological Invariants

We have shown the importance of magnetic helicity during reconnection events in **Paper I** and **Paper II**. Since this has not been adequately appreciated in other works on reconnection it would be important to revisit those works considering the aspect of magnetic helicity conservation.

Magnetic helicity is a second order invariant in the magnetic field $\boldsymbol{B}$, since H_m scales with $|\boldsymbol{A}|^2$. H_m is sufficient when considering magnetic field

configurations which consist of interlocked flux rings like in Fig. 16. However there exist configurations which are not topologically trivial where magnetic helicity vanishes, like the Borromean rings and the IUCAA logo[6] (Fig. 29). [Yeates et al., 2010] showed that magnetic relaxation can be limited even in the absence of magnetic helicity. A topological number which they defined via field line mapping adds an additional constraint on magnetic relaxation.

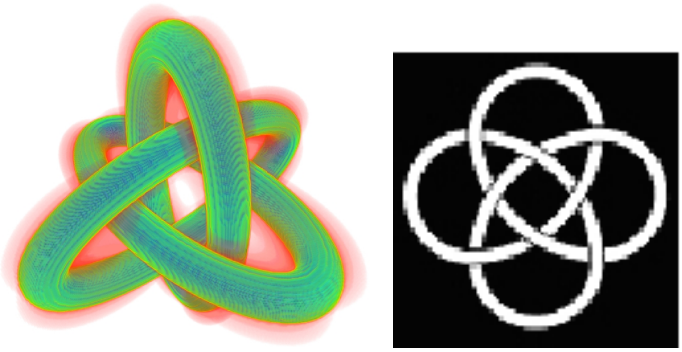

Figure 29: *Left*: Borromean rings. *Right*: IUCAA logo.

Other topological quantities might be of interest when considering knotted structures. The trefoil and higher foil knots (Fig. 30) are helical. However their helicity content cannot be simply represented as for interlocked flux rings (see equation (48)). In the limit of high magnetic Reynolds numbers and with the right boundary conditions helicity is approximately conserved and any decay of energy has to be preceded by reconnection of the flux tube with itself. This makes such configurations particularly interesting. In the limit of an infinite number of foils, where the flux tube approaches itself to an infinitesimally small distance, the configuration can be regarded as a particular version of a twisted flux tube which might not share the same properties. Some preliminary work on the trefoil knot has already been performed in **Paper II**.

[6] IUCAA stands for "Inter-University Centre for Astronomy and Astrophysics", which is the affiliation of professor Subramanian, a frequent visitor at Nordita.

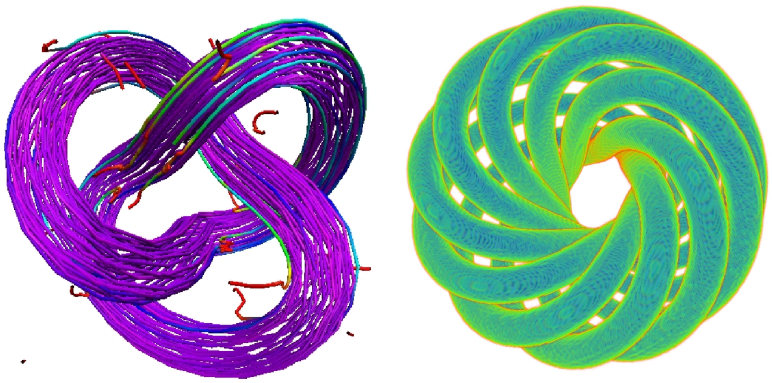

Figure 30: *Left*: magnetic streamlines of the trefoil knot. *Right*: magnetic flux tube of the 9-foil knot.

In **Paper I** we showed that for high magnetic Reynolds numbers a linked configuration with no helicity behaves similarly but not equally to the unlinked configuration. In order to distinguish those cases one can refer to [Ruzmaikin and Akhmetiev, 1994] who suggested with the help of Seifert surfaces two higher order topological invariants of order three and four. Unlike helicity these invariants are not conserved in reconnection. For the Borromean rings they even vanish after reconnection [Ruzmaikin and Akhmetiev, 1994].

9 My Contribution to the Papers

Paper I started out of my project for a course on solar physics. I contributed with performing some of the simulations, producing plots and writing some chapters. The evaluation of the simulation results was done together with the other authors. **Paper II** is a follow up of **Paper I** and was completely conducted by me. **Paper III** started together with my postgraduate studies. I performed some of the simulations and contributed to the text and did various corrections. For **Paper IV** I contributed to the evaluation and interpretation of the simulations as well to doing various corrections. For **Paper V** I was the executor. I performed most of the simulations, plotted various diagrams and wrote large parts of the text.

10 Svensk Sammanfattning

Solens magnetfält uppenbarar sig genom dess solfläckar. De är regioner med ett starkt magnetfält som överstiger omgivande fälts storlek med upp till 2000 Gauss. Det starka fältet undertrycker konvektionsströmmar av hett ämne som medför att fläcken kyls av genom termisk strålning. Solfläckar uppstår inte godtyckligt, utan de uppvisar en cykel som varar 11 år. Under den tiden kan man observera att det genomsnittliga antalet på solfläckar i varje breddgrad varierar på ett sådant sätt att dess diagram ser ut som en fjäril (Fig. 1).

Solens magnetiska aktivitet påverkar solvinden, som består av laddade partiklar med en hastighet mellan 1000 och 2000 km i timmen. Denna vind är inte farlig för människor på jorden, eftersom vi blir skyddade av jordens magnetfält. När partiklarna träffar jorden yttrar det sig genom imponerande norrsken och sydsken. Däremot kan det vara farligt för elektroniska anläggningar både på jorden och i rymden. Det har hänt flera gånger att känslig elektronisk utrustning har blivit påverkad av solvinden. I mars 1989 blev Quebecs elektricitetsnät skadat av laddade partiklar från solen. För rymdfarare är det livsfarligt att bli träffad av solvinden. Därför är det viktigt att kunna förutsäga solens aktivitet.

Solens magnetfält tycks uppstå genom en dynamoprocess. Det är den enda accepterade förklaringen hittills. Det visar sig att den magnetiska heliciteten spelar en viktig roll inom dynamoteorin, eftersom den blir naturligt separerad i stor- och småskaliga delar under uppbyggnaden av stora magnetfält. Dess närvaro motverkar dynamoprocessen och måste därför föras ut ur systemet.

I denna avhandling undersöker jag hur den magnetiska heliciteten kan påverka en dynamo. Jag visar att den måste släppas ut ur systemet via strömmar genom domänens gräns. Mer överraskande är att redan strömmar genom ekvatorn kan lindra dämpningen av dynamoprocessen. Den magnetiska heliciteten beror på valet av gauge, däremot beror den fysikaliska dynamoprocessen inte på gaugen. Jag visar att om man ändrar gaugen så förblir tidsgenomsnittet av helicitetsströmmen konstant, vilket räddar dess fysikaliska betydelse.

Den magnetiska heliciteten är knuten till den topologiska strukturen av det magnetiska fältet. Därför jämför jag tre konfigurationer varav två skiljer sig bara i den magnetiska heliciteten medan topologin är den samma. Den tredje, som är en testkonfiguration, är topologiskt annorlunda men har hellre ingen magnetisk helicitet. De båda ohelikala konfigurationerna beter sig likadant men skillnat från den helikala. Det tyder på att det är den

magnetiska heliciteten snarare än den topologiska strukturen som påverkar systemens dynamik.

11 Acknowledgements

Even though this thesis has been produced by one person the work it is based on was a collaborative effort. Therefore I thank Piyali Chatterjee, Dhrubaditya Mitra, Alexander Hubbard, Fabio Del Sordo and Axel Brandenburg for the excellent teamwork and countless discussions. Special thanks goes to my supervisor Axel Brandenburg for innumerable many dialogues which helped a great deal in understanding this wide field and choosing the right direction to go. I also thank Alexander Hubbard, Piyali Chatterjee and Hans von Zur-Mühlen for proofreading parts of this thesis, as well as my fellow PhD students Fabio Del Sordo, Jörn Warnecke and Koen Kemel for helps with the Pencil Code and LaTeX.

Appendices

A Vector Calculus Identities

For the derivation of the evolution equations in MHD in section 2.1 some of the following vector calculus identities are used.

$$(\mathbf{a}\times\mathbf{b})\cdot(\mathbf{c}\times\mathbf{d}) = (\mathbf{a}\cdot\mathbf{c})(\mathbf{b}\cdot\mathbf{d}) - (\mathbf{a}\cdot\mathbf{d})(\mathbf{b}\cdot\mathbf{c}) \tag{84}$$

$$\mathbf{a}\times(\mathbf{b}\times\mathbf{c}) = (\mathbf{a}\cdot\mathbf{c})\mathbf{b} - (\mathbf{a}\cdot\mathbf{b})\mathbf{c} \tag{85}$$

$$\nabla\times(\nabla\times\mathbf{a}) = \nabla(\nabla\cdot\mathbf{a}) - \nabla^2\mathbf{a} \tag{86}$$

$$\nabla\cdot(\psi\mathbf{a}) = \mathbf{a}\cdot\nabla\psi + \psi\nabla\cdot\mathbf{a} \tag{87}$$

$$\nabla\times(\psi\mathbf{a}) = \nabla\psi\times\mathbf{a} + \psi\nabla\times\mathbf{a} \tag{88}$$

$$\begin{aligned}\nabla(\mathbf{a}\cdot\mathbf{b}) = {} & (\mathbf{a}\cdot\nabla)\mathbf{b} + (\mathbf{b}\cdot\nabla)\mathbf{a} \\ & +\mathbf{a}\times(\nabla\times\mathbf{b}) + \mathbf{b}\times(\nabla\times\mathbf{a})\end{aligned} \tag{89}$$

$$\nabla\cdot(\mathbf{a}\times\mathbf{b}) = \mathbf{b}\cdot(\nabla\times\mathbf{a}) - \mathbf{a}\cdot(\nabla\times\mathbf{b}) \tag{90}$$

$$\nabla\times(\mathbf{a}\times\mathbf{b}) = \mathbf{a}(\nabla\cdot\mathbf{b}) - \mathbf{b}(\nabla\cdot\mathbf{a}) + (\mathbf{b}\cdot\nabla)\mathbf{a} - (\mathbf{a}\cdot\nabla)\mathbf{b} \tag{91}$$

B Maxwell Equations

The Maxwell equations as we use them in section 2.1 are those formulated with the total charges, that is also charges contained in macroscopical objects (media).

$$\nabla\cdot\mathbf{E} = \frac{\rho}{\epsilon_0} \tag{92}$$

$$\nabla\cdot\mathbf{B} = 0 \tag{93}$$

$$\nabla\times\mathbf{E} + \frac{\partial\mathbf{B}}{\partial t} = 0 \tag{94}$$

$$\nabla\times\mathbf{B} - \mu_0\epsilon_0\frac{\partial\mathbf{E}}{\partial t} = \mu_0\mathbf{J}, \tag{95}$$

with:

$\mathbf{E}$	electric field
$\mathbf{B}$	magnetic induction, magnetic flux density, magnetic field[7]
ρ	total charge density
$\mathbf{J}$	total current density
ϵ_0	permittivity of vacuum
μ_0	permeability of vacuum

C Realizability Condition Derived

The realizability condition has been noted in section 4. The missing derivation [Brandenburg and Subramanian, 2005a, pp. 30] will be discussed here.

The Fourier-transformed magnetic vector potential $\widehat{\boldsymbol{A}}(\boldsymbol{k})$ is decomposed into a longitudinal component $\boldsymbol{h}^{\parallel}$ and the two eigenfunctions of the curl operator $\boldsymbol{h}^{\pm}$

$$\widehat{\boldsymbol{A}}(\boldsymbol{k}) \quad = \quad a^{+}(\boldsymbol{k})\boldsymbol{h}^{+}(\boldsymbol{k}) + a^{-}(\boldsymbol{k})\boldsymbol{h}^{-}(\boldsymbol{k}) + a^{\parallel}(\boldsymbol{k})\boldsymbol{h}^{\parallel}(\boldsymbol{k}), \tag{96}$$

with the prefactors $a(\boldsymbol{k})$. The vectors $\boldsymbol{h}$ are normalized such that

$$\boldsymbol{h}^{+}(\boldsymbol{k})^{*} \cdot \boldsymbol{h}^{+}(\boldsymbol{k}) = \boldsymbol{h}^{-}(\boldsymbol{k})^{*} \cdot \boldsymbol{h}^{-}(\boldsymbol{k}) = \boldsymbol{h}^{\parallel}(\boldsymbol{k})^{*} \cdot \boldsymbol{h}^{\parallel}(\boldsymbol{k}) = 1. \tag{97}$$

Applying the curl operator in k-space leads to:

$$\boldsymbol{k} \times \boldsymbol{h}^{\pm}(\boldsymbol{k}) = \pm k \boldsymbol{h}^{\pm}(\boldsymbol{k}), \quad \boldsymbol{k} \times \boldsymbol{h}^{\parallel}(\boldsymbol{k}) = \boldsymbol{0}, \qquad k = |\boldsymbol{k}|. \tag{98}$$

It follows now that the spectral magnetic helicity $\widehat{H}(k)$ and the magnetic energy $\widehat{M}(k)$ are:

$$\widehat{H}(k) = \int_{-\pi/2}^{\pi/2} \int_{0}^{2\pi} \mathrm{d}\phi \; \mathrm{d}\theta \; \widehat{\boldsymbol{A}}(\boldsymbol{k}) \cdot \widehat{\boldsymbol{B}}(\boldsymbol{k}) k^2 \sin\theta = k(|a_k^{+}|^2 - |a_k^{-}|^2)V \tag{99}$$

$$\widehat{M}(k) = \frac{1}{2\mu_0} \int_{-\pi/2}^{\pi/2} \int_{0}^{2\pi} \mathrm{d}\phi \; \mathrm{d}\theta \; \widehat{\boldsymbol{B}}^2(\boldsymbol{k}) k^2 \sin\theta = \frac{1}{2\mu_0} k^2 (|a_k^{+}|^2 + |a_k^{-}|^2)V, \tag{100}$$

with $V = 4\pi k^2$. From this it follows the realizability condition (44)

$$E_{\mathrm{m}}(k) \geq k|H(k)|/2\mu_0. \tag{101}$$

[7] Common usage is to call $\mathbf{B}$ the magnetic field. In this work I will do so as well. Strictly speaking the magnetic field is $\mathbf{H}$

References

[Berger, 1984] Berger, M. A. (1984). Rigorous new limits on magnetic helicity dissipation in the solar corona. *Geophysical and Astrophysical Fluid Dynamics*, 30:79–104.

[Blackman and Field, 2000a] Blackman, E. G. and Field, G. B. (2000a). Constraints on the Magnitude of α in Dynamo Theory. *ApJ*, 534:984–988.

[Blackman and Field, 2000b] Blackman, E. G. and Field, G. B. (2000b). Coronal activity from dynamos in astrophysical rotators. *Mon Not Roy Astron Soc*, 318:724–732.

[Brandenburg, 2001] Brandenburg, A. (2001). The Inverse Cascade and Nonlinear Alpha-Effect in Simulations of Isotropic Helical Hydromagnetic Turbulence. *ApJ*, 550:824–840.

[Brandenburg, 2009] Brandenburg, A. (2009). Paradigm shifts in solar dynamo modeling. In *IAU Symposium*, volume 259 of *IAU Symposium*, pages 159–166.

[Brandenburg and Dobler, 2001] Brandenburg, A. and Dobler, W. (2001). Large scale dynamos with helicity loss through boundaries. *Astronomy and Astrophysics*, 369:329–338.

[Brandenburg and Käpylä, 2007] Brandenburg, A. and Käpylä, P. J. (2007). Magnetic helicity effects in astrophysical and laboratory dynamos. *New Journal of Physics*, 9:305.

[Brandenburg et al., 1989] Brandenburg, A., Krause, F., Meinel, R., Moss, D., and Tuominen, I. (1989). The stability of nonlinear dynamos and the limited role of kinematic growth rates. *Astronomy and Astrophysics*, 213:411–422.

[Brandenburg and Subramanian, 2005a] Brandenburg, A. and Subramanian, K. (2005a). Astrophysical magnetic fields and nonlinear dynamo theory. *Physics Reports*, 417:1–209.

[Brandenburg and Subramanian, 2005b] Brandenburg, A. and Subramanian, K. (2005b). Strong mean field dynamos require supercritical helicity fluxes. *Astronomische Nachrichten*, 326:400–408.

[Brown and Bellan, 1992] Brown, M. and Bellan, P. (1992). Efficiency and scaling of current drive and refuelling by spheromak injection into a tokamak. *Nuclear Fusion*, 32(7):1125.

[Canfield et al., 1999] Canfield, R. C., Hudson, H. S., and McKenzie, D. E. (1999). Sigmoidal morphology and eruptive solar activity. *Geophys. Res. Lett.*, 26(6):627–630.

[Canfield and Pevtsov, 1998] Canfield, R. C. and Pevtsov, A. A. (1998). Helicity of Solar Active-Region Magnetic Fields. In K. S. Balasubramaniam, J. Harvey, & D. Rabin, editor, *Synoptic Solar Physics*, volume 140 of *Astronomical Society of the Pacific Conference Series*, page 131.

[Canfield et al., 1997] Canfield, R. C., Pevtsov, A. A., and McClymont, A. N. (1997). Magnetic Chirality and Coronal Reconnection. In R. D. Bentley & J. T. Mariska, editor, *Magnetic Reconnection in the Solar Atmosphere*, volume 111 of *Astronomical Society of the Pacific Conference Series*, page 341.

[Cattaneo and Hughes, 1996] Cattaneo, F. and Hughes, D. W. (1996). Nonlinear saturation of the turbulent α effect. *Phys. Rev. Lett. E*, 54:4532.

[Chandrasekhar and Woltjer, 1958] Chandrasekhar, S. and Woltjer, L. (1958). On Force-Free Magnetic Fields. *Proceedings of the National Academy of Sciences of the United States of America*, 44(4):285–289.

[Chatterjee et al., 2010] Chatterjee, P., Brandenburg, A., and Guerrero, G. (2010). Can catastrophic quenching be alleviated by separating shear and α effect? *Geophysical and Astrophysical Fluid Dynamics*, 104:591–599.

[Chatterjee et al., 2011] Chatterjee, P., Guerrero, G., and Brandenburg, A. (2011). Magnetic helicity fluxes in interface and flux transport dynamos. *Astronomy and Astrophysics*, 525:A5+.

[Childress and Gilbert, 1995] Childress, S. and Gilbert, A. D. (1995). *Stretch, Twist, Fold: The Fast Dynamo*.

[Gary et al., 1987] Gary, G. A., Moore, R. L., Hagyard, M. J., and Haisch, B. M. (1987). Non-potential features observed in the magnetic field of an active region. *Astrophysical Journal*, 314:782–794.

[Gibson et al., 2002] Gibson, S. E., Fletcher, L., Zanna, G. D., Pike, C. D., Mason, H. E., Mandrini, C. H., Dmoulin, P., Gilbert, H., Burkepile, J., Holzer, T., Alexander, D., Liu, Y., Nitta, N., Qiu, J., Schmieder, B., and Thompson, B. J. (2002). The structure and evolution of a sigmoidal active region. *The Astrophysical Journal*, 574(2):1021.

[Guerrero et al., 2010] Guerrero, G., Chatterjee, P., and Brandenburg, A. (2010). Shear-driven and diffusive helicity fluxes in $\alpha\Omega$ dynamos. *Mon Not Roy Astron Soc*, 409:1619–1630.

[Herzenberg, 1958] Herzenberg, A. (1958). Geomagnetic Dynamos. *Royal Society of London Philosophical Transactions Series A*, 250:543–583.

[Hubbard and Brandenburg, 2011] Hubbard, A. and Brandenburg, A. (2011). Magnetic Helicity Flux in the Presence of Shear. *Astrophysical Journal*, 727:11.

[Ivanova and Ruzmaikin, 1977] Ivanova, T. S. and Ruzmaikin, A. A. (1977). A nonlinear magnetohydrodynamic model of the solar dynamo. *Soviet Astronomy*, 21:479–485.

[Krause and Raedler, 1980] Krause, F. and Raedler, K. (1980). *Mean-field magnetohydrodynamics and dynamo theory*.

[Leka et al., 1996] Leka, K. D., Canfield, R. C., McClymont, A. N., and van Driel-Gesztelyi, L. (1996). Evidence for Current-carrying Emerging Flux. *Astrophysical Journal*, 462:547.

[Léorat et al., 1975] Léorat, J., Frisch, U., and Pouquet, A. (1975). Helical magnetohydrodynamic turbulence and the nonlinear dynamo problem. In V. Canuto, editor, *Role of Magnetic Fields in Physics and Astrophysics*, volume 257 of *New York Academy Sciences Annals*, pages 173–176.

[Manoharan et al., 1996] Manoharan, P. K., van Driel-Gesztelyi, L., Pick, M., and Demoulin, P. (1996). Evidence for Large-Scale Solar Magnetic Reconnection from Radio and X-Ray Measurements. *The Astrophysical Journal*, 468:L73.

[Metcalf et al., 1995] Metcalf, T. R., Jiao, L., McClymont, A. N., Canfield, R. C., and Uitenbroek, H. (1995). Is the solar chromospheric magnetic field force-free? *Astrophysical Journal*, 439:474–481.

[Moffatt, 1969] Moffatt, H. K. (1969). The degree of knottedness of tangled vortex lines. *Journal of Fluid Mechanics Digital Archive*, 35(01):117–129.

[Moffatt, H. K., 1978] Moffatt, H. K., editor (1978). *Magnetic field generation in electrically conducting fluids*.

[Moreau, 1961] Moreau, J. J. (1961). *C. R. Acad. Sci.*, 252:2810.

[Orszag, 1970] Orszag, S. A. (1970). Analytical theories of turbulence. *Journal of Fluid Mechanics Digital Archive*, 41(02):363–386.

[Pevtsov et al., 1996] Pevtsov, A. A., Canfield, R. C., and McClymont, A. N. (1996). Magnetic Chirality and Coronal Reconnection. In *Bulletin of the American Astronomical Society*, volume 28 of *Bulletin of the American Astronomical Society*, page 871.

[Priest and Terry, 2000] Priest, E. R. and Terry, F. (2000). *Magnetic reconnection: MHD theory and applications*.

[Ruzmaikin and Akhmetiev, 1994] Ruzmaikin, A. and Akhmetiev, P. (1994). Topological invariants of magnetic fields, and the effect of reconnections. *Physics of Plasmas*, 1(2):331–336.

[Taylor, 1974] Taylor, J. B. (1974). Relaxation of Toroidal Plasma and Generation of Reverse Magnetic Fields. *Physical Review Letters*, 33:1139–1141.

[Vainshtein and Cattaneo, 1992] Vainshtein, S. I. and Cattaneo, F. (1992). Nonlinear restrictions on dynamo action. *ApJ*, 393:165–171.

[Vishniac and Cho, 2001] Vishniac, E. T. and Cho, J. (2001). Magnetic Helicity Conservation and Astrophysical Dynamos. *The Astrophysical Journal*, 550:752–760.

[Woltjer, 1958a] Woltjer, L. (1958a). A Theorem on Force-Free Magnetic Fields. *Proceedings of the National Academy of Sciences of the United States of America*, 44(6):489–491.

[Woltjer, 1958b] Woltjer, L. (1958b). On Hydromagnetic Equilibrium. *Proceedings of the National Academy of Science*, 44:833–841.

[Yeates et al., 2010] Yeates, A. R., Hornig, G., and Wilmot-Smith, A. L. (2010). Topological Constraints on Magnetic Relaxation. *Physical Review Letters*, 105(8):085002.

I

Magnetic-field decay of three interlocked flux rings with zero linking number

Fabio Del Sordo, Simon Candelaresi, and Axel Brandenburg
NORDITA, AlbaNova University Center, Roslagstullsbacken 23, SE-10691 Stockholm, Sweden and Department of Astronomy, Stockholm University, SE 10691 Stockholm, Sweden

(Received 22 October 2009; revised manuscript received 27 January 2010; published 3 March 2010)

The resistive decay of chains of three interlocked magnetic flux rings is considered. Depending on the relative orientation of the magnetic field in the three rings, the late-time decay can be either fast or slow. Thus, the qualitative degree of tangledness is less important than the actual value of the linking number or, equivalently, the net magnetic helicity. Our results do not suggest that invariants of higher order than that of the magnetic helicity need to be considered to characterize the decay of the field.

DOI: 10.1103/PhysRevE.81.036401 PACS number(s): 52.65.Kj, 52.30.Cv, 52.35.Vd

I. INTRODUCTION

Magnetic helicity plays an important role in plasma physics [1–3], solar physics [4–6], cosmology [7–9], and dynamo theory [10,11]. This is connected with the fact that magnetic helicity is a conserved quantity in ideal magnetohydrodynamics [12]. The conservation law of magnetic helicity is ultimately responsible for inverse cascade behavior that can be relevant for spreading primordial magnetic field over large length scales. It is also likely the reason why the magnetic fields of many astrophysical bodies have length scales that are larger than those of the turbulent motions responsible for driving these fields. In the presence of finite magnetic diffusivity, the magnetic helicity can only change on a resistive time scale. Of course, astrophysical bodies are open, so magnetic helicity can change by magnetic helicity fluxes out of or into the domain of interest. However, such cases will not be considered in the present paper.

In a closed or periodic domain without external energy supply, the decay of a magnetic field depends critically on the value of the magnetic helicity. This is best seen by considering spectra of magnetic energy and magnetic helicity. The magnetic energy spectrum $M(k)$ is normalized such that

$$\int M(k)dk = \langle \boldsymbol{B}^2 \rangle / 2\mu_0, \tag{1}$$

where $\boldsymbol{B}$ is the magnetic field, μ_0 is the magnetic permeability, and k is the wave number (ranging from 0 to ∞). The magnetic helicity spectrum $H(k)$ is normalized such that

$$\int H(k)dk = \langle \boldsymbol{A} \cdot \boldsymbol{B} \rangle, \tag{2}$$

where $\boldsymbol{A}$ is the magnetic vector potential with $\boldsymbol{B}=\boldsymbol{\nabla}\times\boldsymbol{A}$. In a closed or periodic domain, $H(k)$ is gauge invariant, i.e., it does not change after adding a gradient term to $\boldsymbol{A}$. For finite magnetic helicity, the magnetic energy spectrum is bound from below [12] such that

$$M(k) \geq k|H(k)|/2\mu_0. \tag{3}$$

This relation is also known as the realizability condition [13]. Thus, the decay of a magnetic field is subject to a corresponding decay of its associated magnetic helicity. Given that in a closed or periodic domain the magnetic helicity changes only on resistive time scales [14], the decay of magnetic energy is slowed down correspondingly. More detailed statements can be made about the decay of turbulent magnetic fields, where the energy decays in a power-law fashion proportional to $t^{-\sigma}$. In the absence of magnetic helicity, $\langle \boldsymbol{A}\cdot\boldsymbol{B} \rangle = 0$, we have a relatively rapid decay with $\sigma \approx 1.3$ [15], while with $\langle \boldsymbol{A}\cdot\boldsymbol{B} \rangle \neq 0$, the decay is slower with σ between 1/2 [9] and 2/3 [16].

The fact that the decay is slowed down in the helical case is easily explained in terms of the topological interpretation of magnetic helicity. It is well known that the magnetic helicity can be expressed in terms of the linking number n of discrete magnetic flux ropes via [13]

$$\int \boldsymbol{A} \cdot \boldsymbol{B} dV = 2n\Phi_1\Phi_2, \tag{4}$$

where

$$\Phi_i = \int_{S_i} \boldsymbol{B} \cdot d\boldsymbol{S} \quad (\text{for } i = 1 \text{ and } 2) \tag{5}$$

are the magnetic fluxes of the two ropes with cross-sectional areas S_1 and S_2. The slowing down of the decay is then plausibly explained by the fact that a decay of magnetic energy is connected with a decay of magnetic helicity via the realizability condition (3). Thus, a decay of magnetic helicity can be achieved either by a decay of the magnetic flux or by magnetic reconnection. Magnetic flux can decay through annihilation with oppositely oriented flux. Reconnection on the other hand reflects a change in the topological connectivity, as demonstrated in detail in Ref. [17], p. 28.

The situation becomes more interesting when we consider a flux configuration that is interlocked, but with zero linking number. This can be realized quite easily by considering a configuration of two interlocked flux rings where a third flux ring is connected with one of the other two rings such that the total linking number becomes either 0 or 2, depending on the relative orientation of the additional ring, as is illustrated in Fig. 1. Topologically, the configuration with linking numbers of 0 and 2 are the same except that the orientation of the field lines in the upper ring is reversed. Nevertheless, the simple topological interpretation becomes problematic in the case of zero linking number, because then also the magnetic helicity is zero, so the bound of M from below disappears,

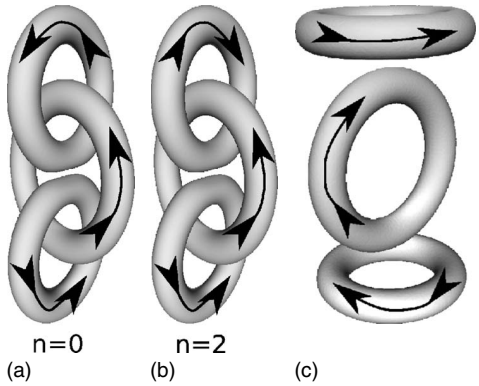

FIG. 1. Visualization of the triple ring configuration at the initial time. Arrows indicate the direction of the field lines in the rings, corresponding to a configuration with $n=0$ (left) and $n=2$ (center). On the right the noninterlocked configuration with $n=0$ is shown.

and M can now in principle freely decay to zero. One might expect that the topology should then still be preserved and that the linking number as defined above, which is a quadratic invariant, should be replaced with a higher-order invariant [18–20]. It is also possible that in a topologically interlocked configuration with zero linking number the magnetic helicity spectrum $H(k)$ is still finite and that bound (3) may still be meaningful. In order to address these questions we perform numerical simulations of the resistive magnetohydrodynamic equations using simple interlocked flux configurations as initial conditions. We also perform a control run with a noninterlocked configuration and zero helicity in order to compare the magnetic energy decay with the interlocked case.

Magnetic helicity evolution is independent of the equation of state and applies hence to both compressible and incompressible cases. In agreement with earlier work [21] we assume an isothermal gas, where pressure is proportional to density and the sound speed is constant. However, in all cases the bulk motions stay subsonic, so for all practical purposes our calculations can be considered nearly incompressible, which would be an alternative assumption that is commonly made [22].

II. MODEL

We perform simulations of the resistive magnetohydrodynamic equations for a compressible isothermal gas where the pressure is given by $p=\rho c_s^2$, with ρ being the density and c_s being the isothermal sound speed. We solve the equations for $\boldsymbol{A}$, the velocity $\boldsymbol{U}$, and the logarithmic density $\ln\rho$ in the form

$$\frac{\partial \boldsymbol{A}}{\partial t} = \boldsymbol{U}\times\boldsymbol{B} + \eta\nabla^2\boldsymbol{A}, \tag{6}$$

$$\frac{\mathrm{D}\boldsymbol{U}}{\mathrm{D}t} = -c_s^2\boldsymbol{\nabla}\ \ln\rho + \boldsymbol{J}\times\boldsymbol{B}/\rho + \boldsymbol{F}_{\mathrm{visc}}, \tag{7}$$

$$\frac{\mathrm{D}\ln\rho}{\mathrm{D}t} = -\boldsymbol{\nabla}\cdot\boldsymbol{U}, \tag{8}$$

where $\boldsymbol{F}_{\mathrm{visc}}=\rho^{-1}\boldsymbol{\nabla}\cdot 2\nu\rho\mathbf{S}$ is the viscous force; $\mathbf{S}$ is the traceless rate of strain tensor, with components $\mathbf{S}_{ij}=\frac{1}{2}(U_{i,j}+U_{j,i})-\frac{1}{3}\delta_{ij}\boldsymbol{\nabla}\cdot\boldsymbol{U}$; $\boldsymbol{J}=\boldsymbol{\nabla}\times\boldsymbol{B}/\mu_0$ is the current density; ν is the kinematic viscosity; and η is the magnetic diffusivity.

The initial magnetic field is given by a suitable arrangement of magnetic flux ropes, as already illustrated in Fig. 1. These ropes have a smooth Gaussian cross-sectional profile that can easily be implemented in terms of the magnetic vector potential. We use the PENCIL code [23], where this initial condition for $\boldsymbol{A}$ is already prepared, except that now we adopt a configuration consisting of three interlocked flux rings (Fig. 1) where the linking number can be chosen to be either 0 or 2, depending only on the field orientation in the last (or the first) of the three rings. Here, the two outer rings have radii R_o, while the inner ring is slightly bigger and has the radius $R_i=1.2R_o$, but with the same flux. We use R_o as our unit of length. The sound travel time is given by $T_s=R_o/c_s$.

In the initial state we have $\boldsymbol{U}=\mathbf{0}$ and $\rho=\rho_0=1$. Our initial flux, $\Phi=\int\boldsymbol{B}\cdot d\boldsymbol{S}$, is the same for all tubes with $\Phi=0.1c_sR_o^2\sqrt{\mu_0\rho_0}$. This is small enough for compressibility effects to be unimportant, so the subsequent time evolution is not strongly affected by this choice. For this reason, the Alfvén time, $T_A=\sqrt{\mu_0\rho_0}R_o^3/\Phi$, will be used as our time unit. In all our cases we have $T_A=10T_s$ and denote the dimensionless time as $\tau=t/T_A$. In all cases we assume that the magnetic Prandtl number ν/η is unity, and we choose $\nu=\eta=10^{-4}R_oc_s=10^{-3}R_o^2/T_A$. We use 256^3 mesh points.

We have chosen a fully compressible code, because it is readily available to us. Alternatively, as discussed at the end of Sec. I, one could have chosen an incompressible code by ignoring the continuity equation and computing the pressure such that $\boldsymbol{\nabla}\cdot\boldsymbol{U}=0$ at all times. Such an operation breaks the locality of the physics and is computationally more intensive, because it requires global communication.

III. RESULTS

Let us first discuss the visual appearance of the three interlocked flux rings at different times. In Fig. 2 we compare the three rings for the zero and finite magnetic helicity cases at the initial time and at $\tau=0.5$. Note that each ring shrinks as a result of the tension force. This effect is strongest in the core of each ring, causing the rings to show a characteristic indentation that was also seen in earlier inviscid and nonresistive simulations of two interlocked flux rings [21].

At early times, visualizations of the field show little difference, but at time $\tau=0.5$ some differences emerge in that the configuration with zero linking number develops an outer ring encompassing the two rings that are connected via the inner ring; see Fig. 2. This outer ring is absent in the configuration with finite linking number.

The change in topology becomes somewhat clearer if we plot the magnetic-field lines (see Fig. 3). For the $n=2$ configuration, at time $\tau=4$ one can still see a structure of three interlocked rings, while for the $n=0$ case no clear structure

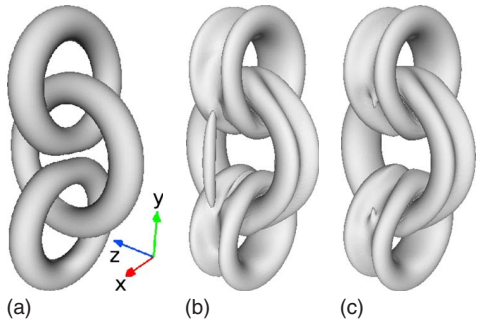

FIG. 2. (Color online) Visualization of the triple ring configuration at $\tau=0$ (left), as well as at $\tau=0.5$ with zero linking number (center) and finite linking number (right). The three images are in the same scale. The change in the direction of the field in the upper ring gives rise to a corresponding change in the value of the magnetic helicity. In the center we can see the emergence of a new flux ring encompassing the two outer rings. Such a ring is not seen on the right.

can be recognized. Note that the magnitude of the magnetic field has diminished more strongly for $n=0$ than for $n=2$. This is in accordance with our initial expectations.

The differences between the two configurations become harder to interpret at later times. Therefore, we compare in Fig. 4 cross sections of the magnetic field for the two cases. The xy cross sections show clearly the development of the new outer ring in the zero linking number configuration. From this figure it is also evident that the zero linking number case suffers more rapid decay because of the now *anti-aligned* magnetic fields (in the upper panel B_x is of opposite sign about the plane $y=0$ while it is negative in the lower panel).

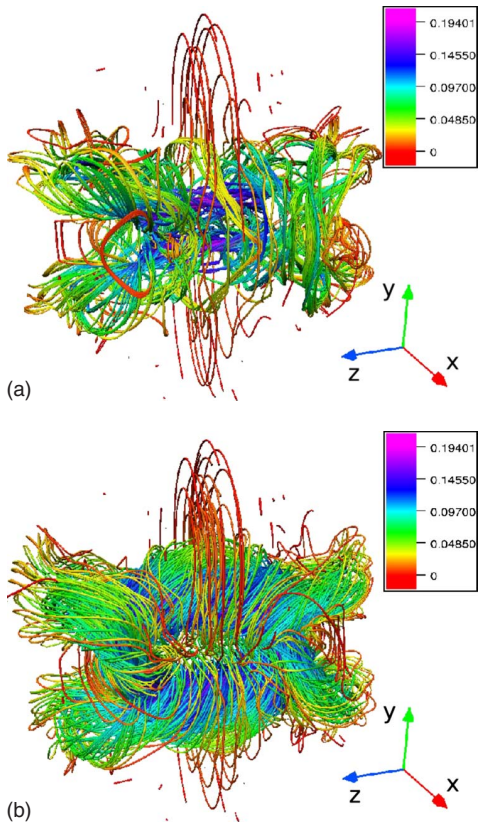

FIG. 3. (Color online) Magnetic flux tubes at time $\tau=4$ for the case of zero linking number (upper picture) and finite linking number (lower picture). The colors represent the magnitude of the magnetic field, where the scale goes from red (lowest) over green to blue (highest).

The evolution of magnetic energy is shown in Fig. 5 for the cases with zero and finite linking numbers. Even at the time $\tau\approx 0.6$, when the rings have just come into mutual contact, there is no clear difference in the decay for the two cases. Indeed, until the time $\tau\approx 2$ the magnetic energy evolves still similarly in the two cases, but then there is a pronounced difference where the energy in the zero linking number case shows a rapid decline (approximately like $t^{-3/2}$), while in the case with finite linking number it declines much more slowly (approximately like $t^{-1/3}$). However, power-law behavior is only expected under turbulent conditions and not for the relatively structured field configurations considered here. The energy decay in the zero linking number case is roughly the same as in a case of three flux rings that are not interlocked. The result of a corresponding control run is shown as a dotted line in Fig. 5. At intermediate times, $0.5<\tau<5$, the magnetic energy of the control run has diminished somewhat faster than in the interlocked case with $n=0$. It is possible that this is connected with the interlocked nature of the flux rings in one of the cases. Alternatively, this might reflect the presence of rather different dynamics in the noninterlocked case, which seems to be strongly controlled by oscillations on the Alfvén time scale. Nevertheless, at later times the decay laws are roughly the same for noninterlocked and interlocked nonhelical cases.

The time when the rings come into mutual contact is marked by a maximum in the kinetic energy at $\tau\approx 0.6$. This can be seen from Fig. 6, where we compare kinetic and magnetic energies separately for the cases with finite and zero linking numbers. Note also that in the zero linking number case magnetic and kinetic energies are nearly equal and decay in the same fashion.

Next we consider the evolution of magnetic helicity in Fig. 7. Until the time $\tau\approx 0.6$ the value of the magnetic helicity has hardly changed at all. After that time there is a gradual decline, but it is slower than the decline of magnetic energy. Indeed, the ratio $\langle \boldsymbol{A}\cdot\boldsymbol{B}\rangle/\langle \boldsymbol{B}^2\rangle$, which corresponds to a length scale, shows a gradual increase from $0.1R_o$ to nearly $0.6R_o$ at the end of the simulation. This reflects the fact that the field has become smoother and more space filling with time.

Given that the magnetic helicity decays only rather slowly, one must expect that the fluxes Φ_i of the three rings also only change very little. Except for simple configurations where flux tubes are embedded in field-free regions, it is in general difficult to measure the actual fluxes, as defined in Eq. (5). On the other hand, especially in observational solar physics, one often uses the so-called *unsigned* flux [24,25], which is defined as

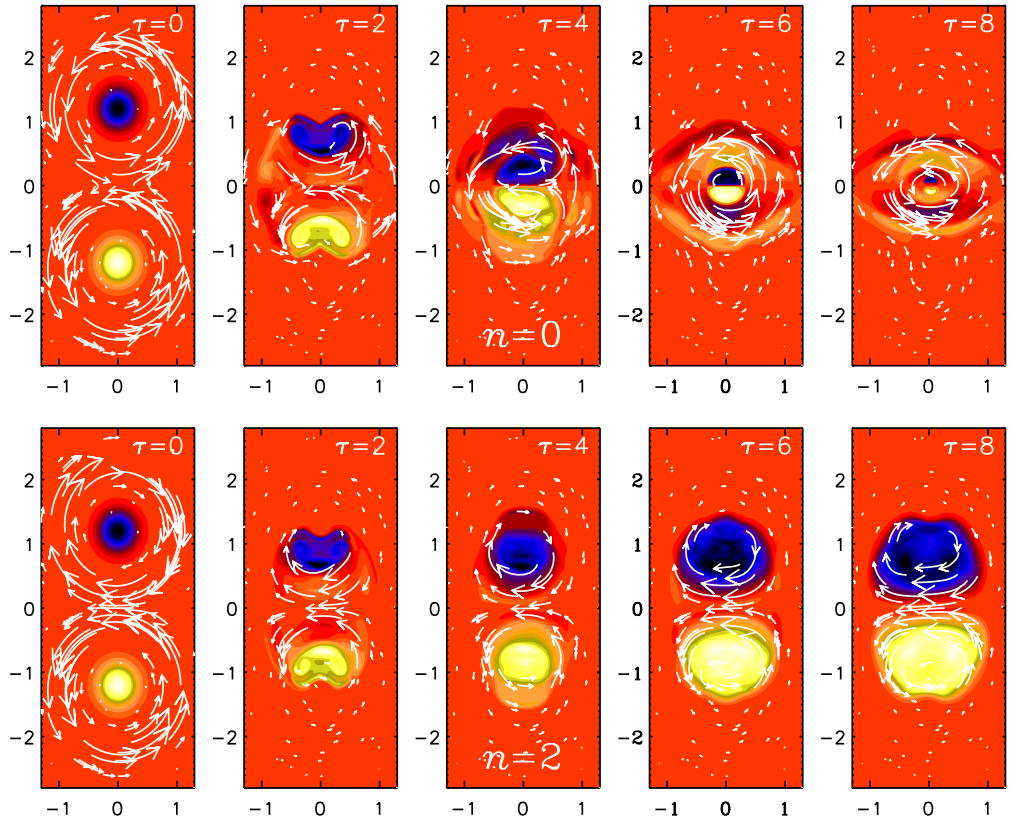

FIG. 4. (Color online) Cross sections in the xy plane of the magnetic field with zero linking number (upper row) and finite linking number (lower row). The z component (pointing out of the plane) is shown together with vectors of the field in the plane. Light (yellow) shades indicate positive values and dark (blue) shades indicate negative values. Intermediate (red) shades indicate zero value.

$$P_{2D} = \int_S |\boldsymbol{B}| dS. \tag{9}$$

For a ring of flux Φ that intersects the surface in the middle at right angles the net flux cancels to zero, but the unsigned flux gets contributions from both intersections, so $P_{2D}=2|\Phi|$. In three-dimensional simulations it is convenient to determine

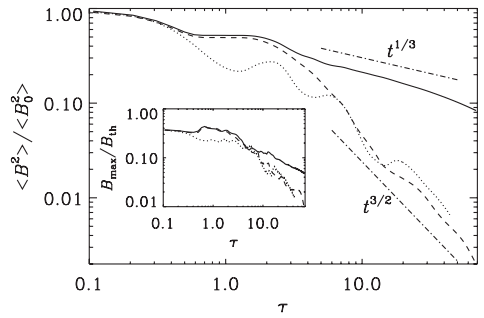

FIG. 5. Decay of magnetic energy (normalized to the initial value) for linking numbers of 2 (solid line) and 0 (dashed line). The dotted line gives the decay for a control run with noninterlocked rings. The dashed-dotted lines indicate $t^{1/3}$ and $t^{3/2}$ scalings for comparison. The inset shows the evolution of the maximum field strength in units of the thermal equipartition value, $B_{th}=c_s(\rho_0\mu_0)^{1/2}$.

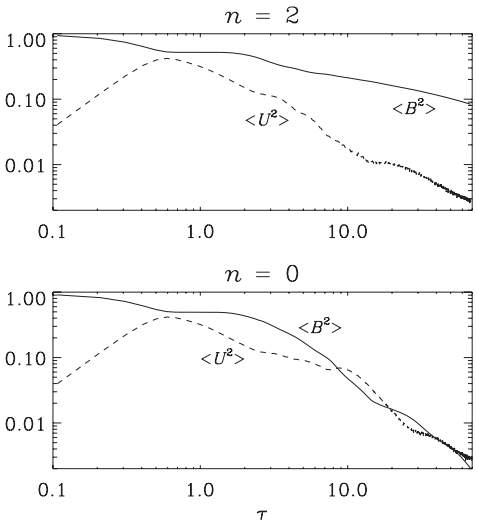

FIG. 6. Comparison of the evolution of kinetic and magnetic energies in the cases with finite and with vanishing linking numbers. Note that in both cases the maximum kinetic energy is reached at the time $\tau\approx 0.6$. The two cases begin to depart from each other after $\tau\approx 2$. In the nonhelical case the magnetic energy shows a sharp drop and reaches equipartition with the kinetic energy, while in the helical case the magnetic energy stays always above the equipartition value.

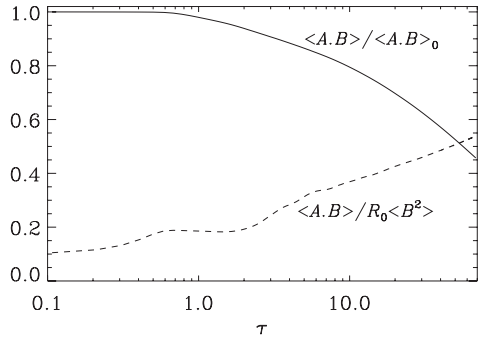

FIG. 7. Evolution of magnetic helicity in the case with finite linking number. In the upper panel, $\langle \boldsymbol{A}\cdot\boldsymbol{B}\rangle$ is normalized to its initial value (indicated by subscript 0) while in the lower panel it is normalized to the magnetic energy divided by R_o.

$$P = \int_V |\boldsymbol{B}| dV. \tag{10}$$

For several rings, all with radius R, we have

$$P = 2\pi R \sum_{i=1}^{N} |\Phi_i| = \pi N R P_{2D}, \tag{11}$$

where N is the number of rings. In Fig. 8 we compare the evolution of P (normalized to the initial value P_0) for the cases with $n=0$ and 2. It turns out that after $\tau=1$ the value of p is nearly constant for $n=2$, but not for $n=0$.

Let us now return to the earlier question of whether a flux configuration with zero linking number can have finite spectral magnetic helicity, i.e., whether $H(k)$ is finite but of opposite sign at different values of k. The spectra $M(k)$ and $H(k)$ are shown in Fig. 9 for the two cases at time $\tau=5$. This figure shows that in the configuration with zero linking number $H(k)$ is essentially zero for all values of k. This is not the case and, in hindsight, is hardly expected; see Fig. 9 for the spectra of $M(k)$ and $k|H(k)|/2\mu_0$ in the two cases at $\tau=5$. What might have been expected is a segregation of helicity not in the wave-number space, but in the physical space for positive and negative values of y. It is then possible that magnetic helicity has been destroyed by locally generated

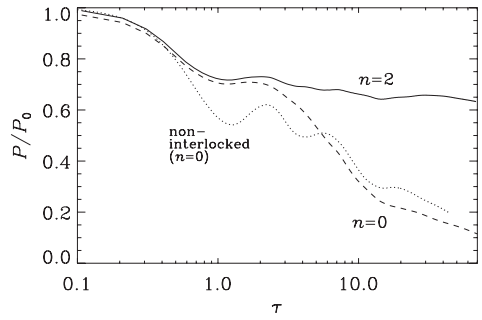

FIG. 8. Decay of the unsigned magnetic flux P (normalized to the initial value P_0) for the cases with $n=0$ and 2. The dotted line gives the decay for a control run with noninterlocked rings.

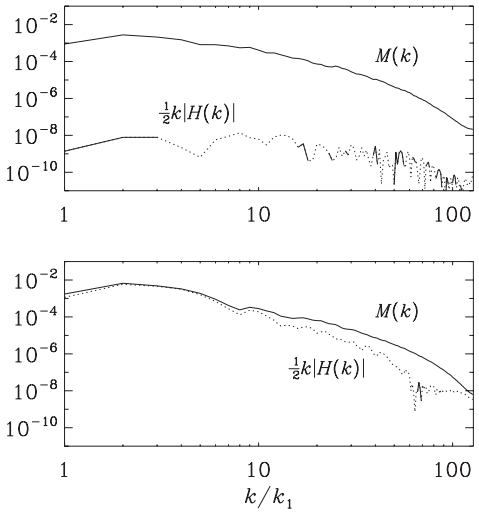

FIG. 9. Comparison of spectra of magnetic energy and magnetic helicity in the case with zero linking number (upper panel) and finite linking number (lower panel) at $\tau=5$. Stretches with negative values of $H(k)$ are shown as dotted lines.

magnetic helicity fluxes between the two domains in $y>0$ and $y<0$. However, this is not pursued further in this paper.

In order to understand in more detail the way the energy is dissipated, we plot in Fig. 10 the evolution of the time derivative of the magnetic energy $E_M=(1/2\mu_0)\int \boldsymbol{B}^2 dV$ (upper panel) and the kinetic energy $E_K=\frac{1}{2}\int \rho \boldsymbol{U}^2 dV$ (lower panel). In the lower panel we also show the rate of work done by the Lorentz force, $W_L=\int \boldsymbol{U}\cdot(\boldsymbol{J}\times\boldsymbol{B})dV$, and in the upper panel we show the rate of work done against the Lorentz force, $-W_L$.

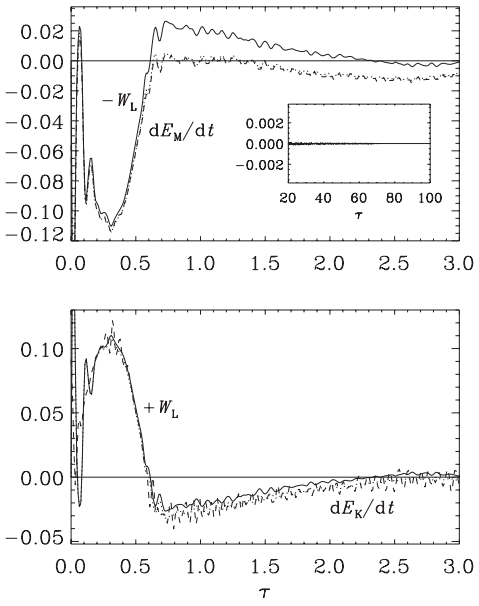

FIG. 10. Evolution of the rate of work done against the Lorentz force, $-W_L$, together with dE_M/dt (upper panel), as well as the rate of work done by the Lorentz force, $+W_L$, together with dE_K/dt (lower panel), all normalized in units of E_M/T_s, for the case with finite linking number. The inset shows $-W_L$ at late times for the case with $n=0$ (solid line) and $n=2$ (dashed line).

All values are normalized by E_{M0}/T_s, where E_{M0} is the value of E_M at $\tau=0$.

The rates of magnetic and kinetic energy dissipations, ϵ_M and ϵ_K, respectively, can be read off as the difference between the two curves in each of the two panels in Fig. 10. Indeed, we have

$$-W_L - dE_M/dt = \epsilon_M, \tag{12}$$

$$W_L + W_C - dE_K/dt = \epsilon_K, \tag{13}$$

where the compressional work term $W_C=\int p\nabla\cdot\boldsymbol{U}dV$ is found to be negligible in all cases. Looking at Fig. 10 we can say that at early times ($0<\tau<0.7$) the magnetic field contributes to driving fluid motions ($W_L>0$) while at later times some of the magnetic energy is replenished by kinetic energy ($W_L<0$), but since magnetic energy dissipation still dominates, the magnetic energy is still decaying ($dE_M/dt<0$). The maximum dissipation occurs around the time $\tau=0.7$. The magnetic energy dissipation is then about twice as large as the kinetic energy dissipation. We note that the ratio between magnetic and kinetic energy dissipations should also depend on the value of the magnetic Prandtl number $\mathrm{Pr}_M=\nu/\eta$, which we have chosen here to be unity. In this connection it may be interesting to recall that one finds similar ratios of ϵ_K and ϵ_M both for helical and nonhelical turbulence [26]. At smaller values of Pr_M the ratio of ϵ_K to $\epsilon_K+\epsilon_M$ diminishes like $\mathrm{Pr}_M^{-1/2}$ for helical turbulence [27]. In the present case the difference between $n=0$ and 2 is, again, small. Only at later times there is a small difference in W_L, as is shown in the inset of Fig. 10. It turns out that, for $n=2$, W_L is positive while for $n=0$ its value fluctuates around zero. This suggests that the $n=2$ configuration is able to sustain fluid motions for longer times than the $n=0$ configuration. This is perhaps somewhat unexpected, because the helical configuration ($n=2$) should be more nearly force free than the nonhelical configuration. However, this apparent puzzle is simply explained by the fact that the $n=2$ configuration has not yet decayed as much as the $n=0$ configuration has.

IV. CONCLUSIONS

The present work has shown that the rate of magnetic energy dissipation is strongly constrained by the presence of magnetic helicity and not by the qualitative degree of knottedness. In our example of three interlocked flux rings we considered two flux chains, where the topology is the same except that the relative orientation of the magnetic field is reversed in one case. This means that the linking number switches from 2 to 0, just depending on the sign of the field in one of the rings. The resulting decay rates are dramatically different in the two cases, and the decay is strongly constrained in the case with finite magnetic helicity.

The present investigations reinforce the importance of considering magnetic helicity in studies of reconnection. Reconnection is a subject that was originally considered in two-dimensional studies of X-point reconnection [28,29]. Three-dimensional reconnection was mainly considered in the last 20 years. An important aspect is the production of current sheets in the course of field line braiding [30]. Such current sheets are an important contributor to coronal heating [31]. The crucial role of magnetic helicity has also been recognized in several papers [32,33]. However, it remained unclear whether the decay of interlocked flux configurations with zero helicity might be affected by the degree of tangledness. Our present work suggests that a significant amount of dissipation should only be expected from tangled magnetic fields that have zero or small magnetic helicity, while tangled regions with finite magnetic helicity should survive longer and are expected to dissipate less efficiently.

ACKNOWLEDGMENTS

We acknowledge the allocation of computing resources provided by the Swedish National Allocations Committee at the Center for Parallel Computers at the Royal Institute of Technology in Stockholm and the National Supercomputer Centers in Linköping. This work was supported in part by the European Research Council under the AstroDyn Research Project No. 227952 and the Swedish Research Council Grant No. 621-2007-4064.

[1] J. B. Taylor, Phys. Rev. Lett. **33**, 1139 (1974).
[2] T. H. Jensen and M. S. Chu, Phys. Fluids **27**, 2881 (1984).
[3] M. Berger and G. B. Field, J. Fluid Mech. **147**, 133 (1984).
[4] D. M. Rust and A. Kumar, Sol. Phys. **155**, 69 (1994).
[5] D. M. Rust and A. Kumar, Astrophys. J. **464**, L199 (1996).
[6] B. C. Low, Sol. Phys. **167**, 217 (1996).
[7] A. Brandenburg, K. Enqvist, and P. Olesen, Phys. Rev. D **54**, 1291 (1996).
[8] G. B. Field and S. M. Carroll, Phys. Rev. D **62**, 103008 (2000).
[9] M. Christensson, M. Hindmarsh, and A. Brandenburg, Astron. Nachr. **326**, 393 (2005).
[10] A. Pouquet, U. Frisch, and J. Léorat, J. Fluid Mech. **77**, 321 (1976).
[11] A. Brandenburg and K. Subramanian, Phys. Rep. **417**, 1 (2005).
[12] L. Woltjer, Proc. Natl. Acad. Sci. U.S.A. **44**, 489 (1958).
[13] H. K. Moffatt, J. Fluid Mech. **35**, 117 (1969).
[14] M. Berger, Geophys. Astrophys. Fluid Dyn. **30**, 79 (1984).
[15] M.-M. Mac Low, R. S. Klessen, and A. Burkert, Phys. Rev. Lett. **80**, 2754 (1998).
[16] D. Biskamp and W.-C. Müller, Phys. Rev. Lett. **83**, 2195 (1999).
[17] E. Priest and T. Forbes, *Magnetic Reconnection* (Cambridge University Press, Cambridge, England, 2000).
[18] A. Ruzmaikin and P. Akhmetiev, Phys. Plasmas **1**, 331 (1994).
[19] G. Hornig and C. Mayer, J. Phys. A **35**, 3945 (2002).
[20] R. Komendarczyk, Commun. Math. Phys. **292**, 431 (2009).
[21] R. M. Kerr and A. Brandenburg, Phys. Rev. Lett. **83**, 1155 (1999).

[22] R. Grauer and C. Marliani, Phys. Rev. Lett. **84**, 4850 (2000).
[23] http://pencil-code.googlecode.com
[24] C. Zwaan, Sol. Phys. **100**, 397 (1985).
[25] C. J. Schrijver and K. L. Harvey, Sol. Phys. **150**, 1 (1994).
[26] N. E. L. Haugen, A. Brandenburg, and W. Dobler, Astrophys. J. **597**, L141 (2003).
[27] A. Brandenburg, Astrophys. J. **697**, 1206 (2009).
[28] E. N. Parker, J. Geophys. Res. **62**, 509 (1957).
[29] D. Biskamp, Phys. Fluids **29**, 1520 (1986).
[30] M. A. Berger, Phys. Rev. Lett. **70**, 705 (1993).
[31] K. Galsgaard and Å. Nordlund, J. Geophys. Res. **101**, 13445 (1996).
[32] Y. Q. Hu, L. D. Xia, X. Li, J. X. Wang, and G. X. Ai, Sol. Phys. **170**, 283 (1997).
[33] Y. Liu, H. Kurokawa, C. Liu, D. H. Brooks, J. Dun, T. T. Ishii, and H. Zhang, Sol. Phys. **240**, 253 (2007).

II

Advances in Plasma Astrophysics
Proceedings IAU Symposium No. 274, 2010
A. Bonanno, E. de Gouveia dal Pino & A. Kosovichev, eds.

DOI: 00.0000/X000000000000000X

Decay of trefoil and other magnetic knots

Simon Candelaresi, Fabio Del Sordo and Axel Brandenburg

NORDITA, AlbaNova University Center, Roslagstullsbacken 23, SE-10691 Stockholm, Sweden
and
Department of Astronomy, Stockholm University, SE 10691 Stockholm, Sweden

Abstract. Two setups with interlocked magnetic flux tubes are used to study the evolution of magnetic energy and helicity on magnetohydrodynamical (MHD) systems like plasmas. In one setup the initial helicity is zero while in the other it is finite. To see if it is the actual linking or merely the helicity content that influences the dynamics of the system we also consider a setup with unlinked field lines as well as a field configuration in the shape of a trefoil knot. For helical systems the decay of magnetic energy is slowed down by the helicity which decays slowly. It turns out that it is the helicity content, rather than the actual linking, that is significant for the dynamics.

Keywords. Sun: magnetic fields

Magnetic helicity has been shown to play an important role in the dynamo process (Brandenburg & Subramanian 2005). For periodic systems where helicity is conserved simulations have shown that with increasing magnetic Reynolds number $\mathrm{Re_M}$ the saturation magnetic field strength decreases like $\mathrm{Re_M^{-1/2}}$ (Brandenburg & Dobler 2001). This is problematic for astrophysical bodies since for the Sun $\mathrm{Re_M} = 10^9$ and galaxies $\mathrm{Re_M} = 10^{14}$. In order to alleviate this quenching the magnetic helicity of the small scale fields needs to be shed (Brandenburg et al. 2009).

In the active regions of the Sun twisted magnetic field lines have been observed (Pevstov et al. 1995). Later it was shown (Leka et al. 1996) that the magnetic field in sunspots gets twisted before it emerges out of the surface. (Manoharan et al. 1996) and (Canfield et al. 1999) demonstrated that helical structures are more likely to erupt into coronal mass ejections. This suggests that the Sun sheds helicity.

The magnetic helicity is related to the mutual linking for two non-intersecting flux tubes via (Moffatt 1969)

$$H = \int_V \boldsymbol{A} \cdot \boldsymbol{B} \, \mathrm{d}V = 2n\phi_1\phi_2,$$

where H is the magnetic helicity, $\boldsymbol{B} = \nabla \times \boldsymbol{A}$ is the magnetic field in terms of the vector potential $\boldsymbol{A}$, ϕ_1 and ϕ_2 are the magnetic fluxes through the tubes and n is the linking number. The flux tubes may not have internal twist. In the limit of large $\mathrm{Re_M}$ H is a conserved quantity as well as the linking number.

In presence of magnetic helicity the magnetic energy decay is constrained via the realizability condition (Moffatt 1969) which gives a lower bound for the spectral magnetic energy

$$M(k) \geqslant k|H(k)|/2\mu_0 \quad \text{with} \quad \int M(k) \, \mathrm{d}k = \langle \boldsymbol{B}^2 \rangle / 2\mu_0, \quad \int H(k) \, \mathrm{d}k = \langle \boldsymbol{A} \cdot \boldsymbol{B} \rangle,$$

the magnetic permeability μ_0, where $\langle . \rangle$ denotes volume integrals.

In this work we extend earlier work (Del Sordo et al. 2010) where the dynamics of interlocked flux rings, with and without helicity, was studied as well as a non-interlocked configuration. Here we also study a self-interlocked flux tube in the form of a trefoil knot.

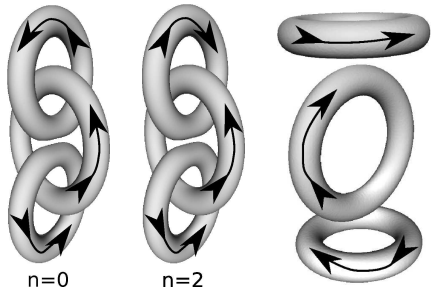

Figure 1. The three triple ring configurations for the initial time. From left to right: interlocked rings with no helicity, interlocked rings with finite helicity and non-interlocked rings without helicity. The arrows indicate the direction of the magnetic field. Adapted from (Del Sordo et al. 2010).

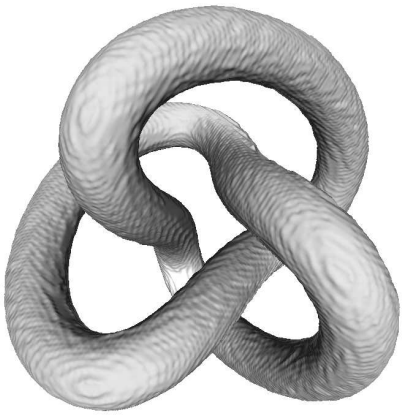

Figure 2. The initial magnetic field configuration for the trefoil knot.

The three-rings setups consist of three magnetic flux tubes. In two configurations they are interlocked where in one the helicity is zero and in the other one it has a finite value, as shown in Fig. 1. In the third setup we instead consider unlocked rings. Since the rings do not have internal twist, the helicity of this last configuration is zero. We also study the evolution of a self-interlocked flux tube having the form of a trefoil knot, with finite helicity (Fig. 2). In this case we have $H = 3\phi^2$, so the linking number is $n = 3/2$. All of these setups evolve according to the full resistive equations of MHD for an isothermal compressible medium. The Alfvén time is used as time unit.

As a consequence of the realizability condition the magnetic energy cannot decay faster than the helicity. The setups with finite H show a slower decay than the setups with no helicity (Fig. 3). The decay of the trefoil knot follows approximately the same decay law as the other configuration consisting of three rings with finite H. Within the simulation time H decays only to about one half of the initial value conserving then the topology. During later times field lines reconnect and the helicity seems to go into internal twist, which is topologically equivalent to linking; see Fig. 4.

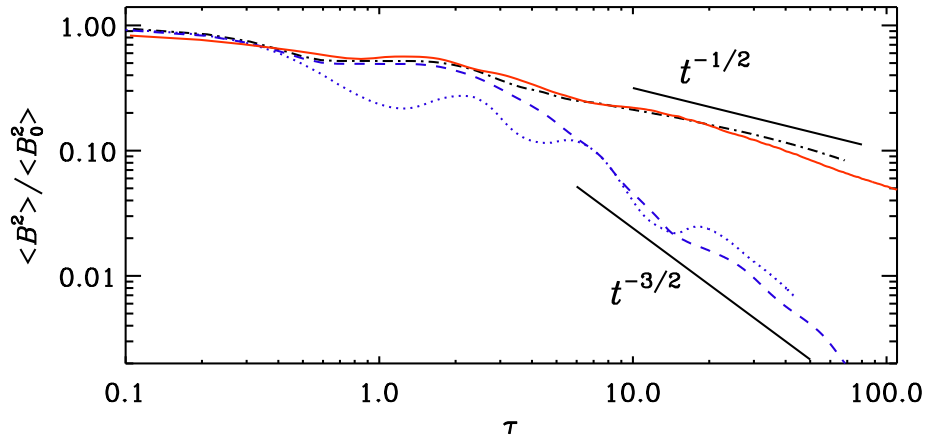

Figure 3. Evolution of the normalized magnetic energy for the trefoil know (solid/red line) compared with various three-ring configurations with $n = 2$ (dash-dotted line), $n = 0$ (dashed/blue line), and the non-interlocked case (dotted/blue line).

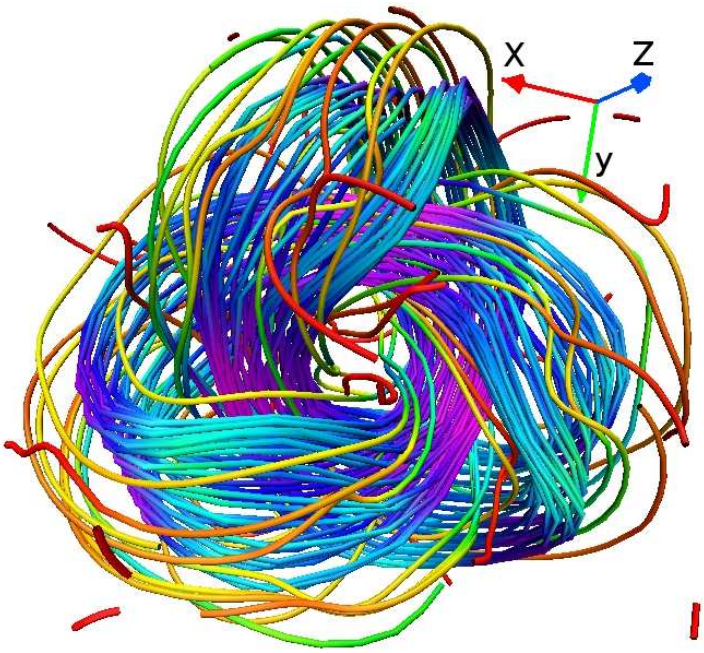

Figure 4. Magnetic field lines at 5 Alfvén times for the trefoil knot. The colors represent the magnitude of the magnetic field. Note that internal twist generation is weak.

The slow decay of H conserves the topology of the system. The linking is then eventually transformed into internal twisting during magnetic reconnection. Since both non-helical setups evolve similarly we conclude that it is mainly the magnetic helicity and not the actual linking which influences the dynamics. The helical trefoil knot evolves in a similar manner. This confirms the hypothesis that the decay of interlinked flux structures is governed by magnetic helicity and that higher-order invariants, advocated for example by (Yeates et al. 2010), may not be essential for describing this process.

In conclusion, we can say that magnetic helicity is decisive in controlling the decay of interlocked magnetic flux structures. If the magnetic helicity is zero, resistive decay will be fast while with finite magnetic helicity the decay will be slow and the speed of decay of magnetic energy depends on the speed at which magnetic helicity decays. This is likely an important aspect also in magnetic reconnection problems that has not yet received sufficient attention.

References

Brandenburg, A. & Subramanian, K. 2005, *Phys. Rep.* 417, 1
Brandenburg, A. & Dobler, W. 2001, *Astron. Astrophys.* 369, 329
Brandenburg, A., Candelaresi, S. & Chatterjee P. 2009, *MNRAS* 398, 1414
Canfield, R. C., Hudson, H. S. & McKenzie, D. E. 1999, *Geophys. Res. Lett.* 26, 627
Moffatt H. K. 1969, *J. Fluid Mech.* 35, 117
Del Sordo, F., Candelaresi, S. & Brandenburg, A. 2010, *Phys. Rev. E* 81, 036401
Gibson, S. E., Fletcher, L., Del Zanna G. & et al. 2002 *ApJ* 574, 1021
Leka, K. D., Canfield, R. C., McClymont A. N. & van Driel-Gesztelyi, L. 1996, *ApJ* 462, 547
Manoharan, P. K., van Driel-Gesztelyi, L., Pick, M. & Demoulin P. 1996, *ApJ* 468, L73
Pevtsov, A. A., Canfield, R. C. & Metcalf, T. R. 1995, *ApJ* 440, L109
Yeates, A. R., Hornig, G., & Wilmot-Smith, A. L. 2010, Phys. Rev. Lett., 105, 085002

III

Mon. Not. R. Astron. Soc. **398,** 1414–1422 (2009) doi:10.1111/j.1365-2966.2009.15188.x

Small-scale magnetic helicity losses from a mean-field dynamo

Axel Brandenburg,[1,2]★ Simon Candelaresi[1,2] and Piyali Chatterjee[3]

[1]*NORDITA, AlbaNova University Center, Roslagstullsbacken 23, SE 10691 Stockholm, Sweden*
[2]*Department of Astronomy, AlbaNova University Center, Stockholm University, SE 10691 Stockholm, Sweden*
[3]*Department of Astronomy and Astrophysics, Tata Institute of Fundamental Research, Colaba, Mumbai 400005, India*

Accepted 2009 June 5. Received 2009 June 5; in original form 2009 May 3

ABSTRACT

Using mean-field models with a dynamical quenching formalism, we show that in finite domains magnetic helicity fluxes associated with small-scale magnetic fields are able to alleviate catastrophic quenching. We consider fluxes that result from advection by a mean flow, the turbulent mixing down the gradient of mean small-scale magnetic helicity density or the explicit removal which may be associated with the effects of coronal mass ejections in the Sun. In the absence of shear, all the small-scale magnetic helicity fluxes are found to be equally strong for both large- and small-scale fields. In the presence of shear, there is also an additional magnetic helicity flux associated with the mean field, but this flux does not alleviate catastrophic quenching. Outside the dynamo-active region, there are neither sources nor sinks of magnetic helicity, so in a steady state this flux must be constant. It is shown that unphysical behaviour emerges if the small-scale magnetic helicity flux is forced to vanish within the computational domain.

Key words: hydrodynamics – magnetic fields – MHD – turbulence.

1 INTRODUCTION

Both mean-field theories and direct simulations of the generation of large-scale magnetic fields in astrophysical bodies, such as the Sun or the Galaxy, invoke the effects of twist. Twist is typically the result of the Coriolis force acting on ascending or descending magnetic field structures in a stratified medium. The net effect of this systematic twisting motion on the magnetic field is called the α effect. In textbooks, the α effect is normally introduced as a result of helical turbulence (Moffatt 1978; Parker 1979; Krause & Rädler 1980), but it could also arise from magnetic buoyancy instabilities (Schmitt 1987; Brandenburg & Schmitt 1998). The latter may also be at the heart of what is known as the Babcock–Leighton mechanism that describes the net effect of the tilt of decaying active regions. Mathematically, this mechanism can also be described by an α effect (Stix 1974). Regardless of all these details, any of these processes face a serious challenge connected with the conservation of magnetic helicity (Pouquet, Frisch & Léorat 1976; Kleeorin & Ruzmaikin 1982; Kleeorin, Rogachevskii & Ruzmaikin 1995). The seriousness of this is not generally appreciated, even though the conservation of magnetic helicity has long been associated with what is called catastrophic α quenching (Gruzinov & Diamond 1994, 1995, 1996). Catastrophic α quenching refers to the fact that the α effect in helical turbulence in a periodic box decreases with increasing magnetic Reynolds number for equipartition strength magnetic fields (Vainshtein & Cattaneo 1992; Cattaneo & Hughes 1996). This would be 'catastrophic' because the magnetic Reynolds number is large (10^9 in the Sun and 10^{15} in the Galaxy).

A promising theory for modelling catastrophic α quenching in a mean-field simulation is the dynamical quenching approach involving an evolution equation for the α effect that follows from magnetic helicity conservation (Kleeorin & Ruzmaikin 1982). Later, Field & Blackman (2002) showed for the first time that this formalism is also able to describe the slow saturation of a helical dynamo in a triply periodic domain (Brandenburg 2001a). As this dynamo evolves towards saturation, a large-scale magnetic field builds up, but this field possesses magnetic helicity. Indeed, the eigenfunction of a homogeneous α^2 dynamo has magnetic and current helicities proportional to α. However, this concerns only the mean field, and since the helicity of the total field is conserved, the small-scale or fluctuating field must have magnetic helicity of the opposite sign (Seehafer 1996). This leads to a reduction of the α effect (Pouquet et al. 1976).

The dynamical quenching formalism is now frequently used to model the non-linear behaviour of mean-field dynamos with and without shear (Blackman & Brandenburg 2002), open or closed boundaries (Brandenburg & Subramanian 2005) and sometimes even without α effect (Yousef, Brandenburg & Rüdiger 2003; Brandenburg & Subramanian 2005). However, it soon became clear that the catastrophic quenching of the α effect can only be alleviated in the presence of magnetic helicity fluxes out of the domain (Blackman & Field 2000a,b; Kleeorin et al. 2000, 2002). There are various contributions to the magnetic helicity flux (Rogachevskii &

★E-mail: brandenb@nordita.org

Kleeorin 2000; Vishniac & Cho 2001; Subramanian & Brandenburg 2004, 2006), but one of the most obvious ones is that associated with advection. Shukurov et al. (2006) have implemented this effect in a mean-field model with dynamical quenching in order to model the effects of outflows on the evolution of the galactic magnetic field. One goal of this paper is to study this effect in more detail. In particular, it is important to clarify the consequences of boundary conditions on the local dynamics away from the boundaries. Indeed, is it really true that a helicity flux has to be maintained all the way to the boundaries, or can the helicity flux be confined to a part of the domain to alleviate catastrophic α quenching at least locally? What happens if this is not the case?

The notion of alleviating catastrophic α quenching only locally is sometimes invoked in models of the solar dynamo that rely on the production of strong magnetic fields at the bottom of the convection zone. By placing the α effect only near the surface, as is done in the interface dynamo of Parker (1993) or dynamos that are controlled by meridional circulation (Choudhuri, Schüssler & Dikpati 1995), one may evade catastrophic quenching more easily. On the other hand, as shown by Yousef et al. (2003), the effects of magnetic helicity conservation can play a role even if there is originally no α effect. It is therefore important to understand in more detail the physics of dynamical α quenching and its dependence on magnetic helicity fluxes.

Our starting point in this paper is the model of Shukurov et al. (2006), where magnetic helicity fluxes were driven by the advection from an outflow. This allows us to study the effects of varying strength of this flux in different parts of the domain. For simplicity, and in order to isolate the main effects, we ignore shear in most parts of this paper. In view of later applications to the Sun and the Galaxy, this is clearly artificial, but it helps significantly in the interpretation of the results. In particular, in the absence of shear, it is possible to have steady solutions, or at least solutions whose magnetic energy density is constant in time.

2 THE MODEL

2.1 Evolution equation of the mean field

In this paper, we consider a simple mean-field dynamo in a local one-dimensional domain. Such a model could be applicable to one hemisphere of a rotating disc or to the region close to the equator of outer stellar convection zones. Denoting the mean magnetic field by $\overline{\boldsymbol{B}} = \overline{\boldsymbol{B}}(z, t)$, the coordinate z would correspond either to the height above the mid-plane in the case of the disc or to the latitudinal distance from the equator in the case of a spherical shell. The x and y components would correspond to poloidal and toroidal fields, although in the absence of shear the two are interchangeable and cannot be distinguished. Using $\nabla \cdot \overline{\boldsymbol{B}} = \partial \overline{B}_z/\partial z = 0$, we have $\overline{B}_z = \text{constant} = 0$, i.e. no $\overline{B}_z$ field is imposed. Such a mean field could be obtained by averaging the actual magnetic field over the x and y directions of a Cartesian domain.

The evolution of $\overline{\boldsymbol{B}}$ is governed by the Faraday equation

$$\frac{\partial \overline{\boldsymbol{B}}}{\partial t} = -\nabla \times \overline{\boldsymbol{E}}, \tag{1}$$

where $\overline{\boldsymbol{E}} = -(\overline{\boldsymbol{U}}_{\rm S} + \overline{\boldsymbol{U}}) \times \overline{\boldsymbol{B}} - \overline{\boldsymbol{\mathcal{E}}} + \eta\mu_0 \overline{\boldsymbol{J}}$ is the mean electric field, $\overline{\boldsymbol{U}}$ is the mean flow in the z direction, $\overline{\boldsymbol{U}}_{\rm S} = (0, Sx, 0)$ is a linear shear flow, $\overline{\boldsymbol{\mathcal{E}}}$ is the mean electromotive force, $\overline{\boldsymbol{J}} = \nabla \times \overline{\boldsymbol{B}}/\mu_0$ is the mean current density and μ_0 is the vacuum permeability. In one case, we adopt a shear parameter S that is different from zero. Since the shear is linear, we can write $\overline{\boldsymbol{U}}_{\rm S} \times \overline{\boldsymbol{B}}$ as $-S\overline{A}_y \hat{\boldsymbol{x}}$ plus a gradient term that can be removed by a gauge transformation. Thus, we have

$$-\overline{\boldsymbol{E}} = \nabla(Sx\overline{A}_y) - S\overline{A}_y \hat{\boldsymbol{x}} + \overline{\boldsymbol{U}} \times \overline{\boldsymbol{B}} + \overline{\boldsymbol{\mathcal{E}}} - \eta\mu_0 \overline{\boldsymbol{J}}, \tag{2}$$

where $\overline{\boldsymbol{U}}$ is now the flow associated with the outflow only and does not include the shear flow. Next, we express $\overline{\boldsymbol{B}} = \nabla \times \overline{\boldsymbol{A}}$ in terms of the magnetic vector potential $\overline{\boldsymbol{A}}$, and solve equation (1) in its uncurled form, $\partial \overline{\boldsymbol{A}}/\partial t = -\overline{\boldsymbol{E}} - \nabla\overline{\phi}$, where $\overline{\phi}$ is the mean electrostatic potential. We perform a gauge transformation, $\overline{\boldsymbol{A}} \to \overline{\boldsymbol{A}} + \nabla\Lambda$, with the choice $\Lambda = \int (\overline{\phi} - Sx\overline{A}_y)\,{\rm d}t$, which removes the gradient term to yield

$$\frac{\partial \overline{\boldsymbol{A}}}{\partial t} = -\overline{\boldsymbol{E}}, \tag{3}$$

which is then the final form of our equation for $\overline{\boldsymbol{A}}$. This form of the equation together with boundary conditions for $\overline{\boldsymbol{A}}$ characterizes the gauge used to calculate magnetic helicity densities and magnetic helicity fluxes for the mean field.

We solve equation (3) in the domain $0 < z < L$ and assume either a vacuum or a perfect conductor boundary condition on $z = L$. This means that on $z = L$ the mean magnetic field either vanishes, i.e. $\overline{B}_x = \overline{B}_y = 0$, or that its z derivatives vanish, i.e. $\overline{B}_{x,z} = \overline{B}_{y,z} = 0$, where a comma denotes partial differentiation. In terms of $\overline{\boldsymbol{A}}$, this means that on $z = L$ we have either

$$\overline{A}_{x,z} = \overline{A}_{y,z} = 0 \quad \text{(vacuum condition)}, \tag{4}$$

or

$$\overline{A}_x = \overline{A}_y = 0 \quad \text{(perfect conductor condition)}. \tag{5}$$

It is well known that the solutions can be in one of the two pure parity states that are either symmetric (S) or antisymmetric (A) about the mid-plane (Krause & Rädler 1980), so we have either $\overline{B}_{x,z} = \overline{B}_{y,z} = 0$ or $\overline{B}_x = \overline{B}_y = 0$ on $z = 0$. In terms of $\overline{\boldsymbol{A}}$,

$$\overline{A}_x = \overline{A}_y = 0 \quad \text{on } z = 0 \quad \text{(S solution)} \tag{6}$$

or

$$\overline{A}_{x,z} = \overline{A}_{y,z} = 0 \quad \text{on } z = 0 \quad \text{(A solution)}. \tag{7}$$

We note that the particular boundary conditions (5) and (6) fix the value of $\overline{\boldsymbol{A}}$ on $z = L$ or 0, respectively. In all other combinations, the value of $\overline{\boldsymbol{A}}$ is not fixed and the magnetic helicity could exhibit an unphysical drift (Brandenburg, Dobler & Subramanian 2002). However, in this paper we study magnetic helicity density and its flux only in situations where either (5) or (6) is used.

We recall that, even though there is no Ω effect, i.e. no mean flow in the y direction, we shall allow for a flow $\overline{\boldsymbol{U}}$ in the z direction. In a disc, this would correspond to a vertical outflow, while in a star this might locally be associated with meridional circulation.

2.2 Magnetic helicity conservation

In this paper, we will study the evolution of magnetic helicity of mean and fluctuating fields. In our gauge, the evolution of the magnetic helicity density of the mean field, $h_{\rm m} = \overline{\boldsymbol{A}} \cdot \overline{\boldsymbol{B}}$, is given by

$$\frac{\partial \overline{h}_{\rm m}}{\partial t} = 2\overline{\boldsymbol{\mathcal{E}}} \cdot \overline{\boldsymbol{B}} - 2\eta\mu_0 \overline{\boldsymbol{J}} \cdot \overline{\boldsymbol{B}} - \nabla \cdot \overline{\boldsymbol{F}}_{\rm m}, \tag{8}$$

where $\overline{\boldsymbol{F}}_{\rm m} = \overline{\boldsymbol{E}} \times \overline{\boldsymbol{A}}$ is the flux of magnetic helicity of the mean magnetic field. Under the assumption of scale separation, Subramanian & Brandenburg (2006) have defined a magnetic helicity density of the small-scale field in terms of its mutual linkages.

They derived an evolution equation for the magnetic helicity density of the small-scale field,

$$\frac{\partial \overline{h}_{\rm f}}{\partial t} = -2\overline{\boldsymbol{\mathcal{E}}} \cdot \overline{\boldsymbol{B}} - 2\eta\mu_0 \overline{\boldsymbol{j} \cdot \boldsymbol{b}} - \nabla \cdot \overline{\boldsymbol{F}}_{\rm f}, \tag{9}$$

where $\overline{\boldsymbol{F}}_{\rm f}$ is the flux of magnetic helicity density of the fluctuating field. Equation (9) is similar to equation (8), except that $\overline{\boldsymbol{\mathcal{E}}} \cdot \overline{\boldsymbol{B}}$ appears with the opposite sign. This implies that turbulent amplification and diffusion of mean magnetic field (characterized by the $\overline{\boldsymbol{\mathcal{E}}}$ term) cannot change the total magnetic helicity density, $\overline{h} = \overline{h}_{\rm m} + \overline{h}_{\rm f}$, which therefore obeys the equation

$$\frac{\partial \overline{h}}{\partial t} = -2\eta\mu_0 \overline{\boldsymbol{J} \cdot \boldsymbol{B}} - \nabla \cdot \overline{\boldsymbol{F}}, \tag{10}$$

where $\overline{\boldsymbol{F}} = \overline{\boldsymbol{F}}_{\rm m} + \overline{\boldsymbol{F}}_{\rm f}$ is the total magnetic helicity flux, and $\overline{\boldsymbol{J} \cdot \boldsymbol{B}} = \overline{\boldsymbol{J}} \cdot \overline{\boldsymbol{B}} + \overline{\boldsymbol{j} \cdot \boldsymbol{b}}$ is the total current helicity density.

2.3 Dynamical quenching formalism

In order to satisfy the evolution equation for the total magnetic helicity density (10), we have to solve equation (9) along with equation (3), which implies that equations (8) and (10) are automatically obeyed. We assume that $\overline{h}_{\rm f}$ is proportional to $\mu_0 \overline{\boldsymbol{j} \cdot \boldsymbol{b}}$. This $\overline{\boldsymbol{j} \cdot \boldsymbol{b}}$ term also modifies the mean electromotive force by producing an α effect (Pouquet et al. 1976). This is sometimes referred to as the magnetic α effect,

$$\alpha_{\rm M} = \tfrac{1}{3}\tau \overline{\boldsymbol{j} \cdot \boldsymbol{b}}/\overline{\rho}, \tag{11}$$

where τ is the correlation time of the turbulence. In the special case of isotropy of the fluctuating field, the ratio between $\mu_0 \overline{\boldsymbol{j} \cdot \boldsymbol{b}}$ and $\overline{h}_{\rm f}$ is $k_{\rm f}^2$. Direct three-dimensional turbulence simulations (details to be published elsewhere) confirm a proportionality, but the ratio between the two tends to be larger than $k_{\rm f}^2$. We should therefore consider $k_{\rm f}^2$ as an adjustable parameter. In the following, we ignore compressibility effects and assume that the mean density $\overline{\rho}$ is constant.[1] Next, we assume that the turbulence is helical, so there is also a kinetic α effect proportional to the kinetic helicity,

$$\alpha_{\rm K} = -\tfrac{1}{3}\tau \overline{\boldsymbol{\omega} \cdot \boldsymbol{u}}, \tag{12}$$

where $\boldsymbol{\omega} = \nabla \times \boldsymbol{u}$ is the vorticity. The total α effect is then

$$\alpha = \alpha_{\rm K} + \alpha_{\rm M}, \tag{13}$$

and the resulting mean electromotive force is

$$\overline{\boldsymbol{\mathcal{E}}} = \alpha \overline{\boldsymbol{B}} - \eta_{\rm t}\mu_0 \overline{\boldsymbol{J}}, \tag{14}$$

where

$$\eta_{\rm t} = \tfrac{1}{3}\tau \overline{\boldsymbol{u}^2} \tag{15}$$

is the turbulent magnetic diffusivity. In the following, we consider $\eta_{\rm t}$ and η as given and define their ratio as the magnetic Reynolds number, $R_{\rm m} = \eta_{\rm t}/\eta$. We shall express the strength of the magnetic field in terms of the equipartition value,

$$B_{\rm eq} = (\mu_0 \overline{\rho} \overline{\boldsymbol{u}^2})^{1/2}, \tag{16}$$

which allows us to determine τ in the mean-field model via $\frac{1}{3}\tau = \mu_0 \overline{\rho} \eta_{\rm t}/B_{\rm eq}^2$. With these preparations, we can write the dynamical quenching formula as

$$\frac{\partial \alpha_{\rm M}}{\partial t} = -2\eta_{\rm t} k_{\rm f}^2 \left(\frac{\overline{\boldsymbol{\mathcal{E}}} \cdot \overline{\boldsymbol{B}}}{B_{\rm eq}^2} + \frac{\alpha_{\rm M}}{R_{\rm m}} \right) - \frac{\partial}{\partial z} \overline{\mathcal{F}}_\alpha, \tag{17}$$

[1] Note that a constant mean density implies that there must exist a small-scale mass flux compensating the losses associated with the mass flux $\overline{\rho}\overline{\boldsymbol{U}}$.

where $\overline{\mathcal{F}}_\alpha$ is related to the mean magnetic helicity flux of the fluctuating field via

$$\overline{\mathcal{F}}_\alpha = \frac{\mu_0 \overline{\rho} \eta_{\rm t} k_{\rm f}^2}{B_{\rm eq}^2} \overline{\boldsymbol{F}}_{\rm f}. \tag{18}$$

In order to compute mean-field models, we have to solve equation (3) together with equation (17) using a closed expression for the flux $\overline{\mathcal{F}}_\alpha$. In this paper, we focus on the advective flux proportional to $\alpha_{\rm M}\overline{\boldsymbol{U}}$, but in some cases we consider instead the effects of a turbulent magnetic helicity flux that we model by a Fickian diffusion term proportional to $-\kappa_\alpha \nabla \alpha_{\rm M}$, where κ_α is a diffusion term that is either zero or otherwise a small fraction of $\eta_{\rm t}$. A more natural choice might have been $\kappa_\alpha = \eta_{\rm t}$, but since the effects of such diffusive magnetic helicity fluxes have never been seen in simulations, we felt that it would be more convincing if even a small fraction of $\eta_{\rm t}$ would lead to a notable effect.

In addition, we consider cases where we model magnetic helicity fluxes by an explicit removal of $\overline{h}_{\rm f}$ from the domain in regular time intervals Δt. Such an explicit removal of magnetic helicity associated with the fluctuating field may model the effects of coronal mass ejections, although one would expect that in reality such an approach also implies some loss of magnetic helicity associated with the large-scale field. The removal of the fluctuating magnetic field was employed by Brandenburg et al. (2002) in connection with three-dimensional turbulence simulations to demonstrate that it is, at least in principle, possible to alleviate catastrophic quenching by an artificial filtering out of small-scale turbulent magnetic fields. In this paper, we model the occasional removal of $\overline{h}_{\rm f}$ by resetting its values

$$\overline{h}_{\rm f} \to \overline{h}_{\rm f} - \Delta\overline{h}_{\rm f} \quad \text{in regular intervals } \Delta t, \tag{19}$$

where $\Delta\overline{h}_{\rm f} = \epsilon \overline{h}_{\rm f}$ is chosen to be a certain fraction ϵ of the current value of $\overline{h}_{\rm f}$. In our one-dimensional model, the corresponding expression for the flux $\Delta\overline{F}_{\rm f}$ can be obtained by integration, i.e.

$$\Delta\overline{F}_{\rm f}(z,t) = \int_0^z \Delta\overline{h}_{\rm f}(z',t)\,{\rm d}z'. \tag{20}$$

Since magnetic helicity densities and their fluxes are proportional to each other, we have simply

$$\overline{\mathcal{F}}_\alpha = \alpha_{\rm M}\overline{U} - \kappa_\alpha \frac{\partial \alpha_{\rm M}}{\partial z} + \Delta\overline{\mathcal{F}}_\alpha, \tag{21}$$

where $\Delta\overline{\mathcal{F}}_\alpha = (\mu_0 \overline{\rho} \eta_{\rm t} k_{\rm f}^2/B_{\rm eq}^2)\Delta\overline{F}_{\rm f}$ is defined analogously to equation (18).

We note that the α effect will produce magnetic fields that have magnetic helicity with the same sign as that of α, and the rate of magnetic helicity production is proportional to $\alpha\overline{\boldsymbol{B}}^2$. In the Northern hemisphere, we have $\alpha > 0$, so the mean field should have positive magnetic helicity. We recall that shear does not contribute to magnetic helicity production, because the negative electric field associated with the shear flow, $\overline{\boldsymbol{U}}_{\rm S} \times \overline{\boldsymbol{B}}$, gives no contribution to magnetic helicity production, which is proportional to $\overline{\boldsymbol{E}} \cdot \overline{\boldsymbol{B}}$, but it can still give a contribution to the flux of magnetic helicity. This is also evident if we write shear using the $-S\overline{A}_y\hat{\boldsymbol{x}}$ term in equation (2): after multiplying with $\overline{\boldsymbol{B}}$ and using $\overline{B}_x = \partial\overline{A}_y/\partial z$, we find that this term can be integrated to give just an additional flux term, $\frac{1}{2}S\overline{A}_y^2$. However, this contribution belongs clearly to the magnetic helicity flux associated with the large-scale field and is therefore unable to alleviate catastrophic quenching.

2.4 Model profiles and boundary conditions

We consider a model similar to that of Shukurov et al. (2006) who adopted linear profiles for α_K and $\overline{U}$ of the form $\alpha_K = \alpha_0 z/H$ and $\overline{U}_z = U_0 z/H$, where the height H was chosen to be equal to the domain size, $H = L$. However, in order to separate boundary effects from effects of the dynamo we also consider the case where we extend the domain in the z direction and choose $L = 4H$ and let α_K go smoothly to zero at $z = H$ and $\overline{U}_z$ either goes to a constant for $z > H$ or also goes smoothly to zero. Thus, we choose

$$\alpha = \alpha_0 \frac{z}{H} \Theta(z; H, w_\alpha), \tag{22}$$

where we have defined the profile function

$$\Theta(z; H, w) = \frac{1}{2}\left(1 - \tanh\frac{z-H}{w}\right), \tag{23}$$

which is unity for $z \ll H$ and zero otherwise, and w quantifies the width of this transition. For the outflow, we choose the function

$$\overline{U}_z = U_0 \frac{z}{H}\left[1 + (z/H)^n\right]^{-1/n} \Theta(z; H_U, w_U), \tag{24}$$

with $n = 20$. Both profiles are shown in Fig. 1. The strictly linear profiles of Shukurov et al. (2006) can be recovered by taking $L = H$, $w_\alpha \to 0$ and $n \to \infty$.

As length unit, we take $k_1 = \pi/2H$, and as time unit we take $(\eta_t k_1^2)^{-1}$. This deviates from Shukurov et al. (2006), who used π/H as their basic wavenumber. Our motivation for this change is that now the turbulent decay rate is equal to $\eta_t k_1^2$, without an extra 1/4 factor. We adopt non-dimensional measures for α_0, U_0 and S, by defining

$$C_\alpha = \frac{\alpha_0}{\eta_t k_1}, \quad C_U = \frac{U_0}{\eta_t k_1} \quad \text{and} \quad C_S = \frac{S}{\eta_t k_1^2}. \tag{25}$$

To match the parameters of Shukurov et al. (2006), we note that $C_U = 0.6$ corresponds to their value of 0.3, and the value $k_f/k_1 = 10$ corresponds to their value of 5.

We obtain solutions numerically using two different codes. One code uses an explicit third-order Runge–Kutta time-stepping scheme and the other one is a semi-implicit scheme. Both schemes employ a second-order finite differences. We begin by reporting results for the original profile of Shukurov et al. (2006) with $L = H$.

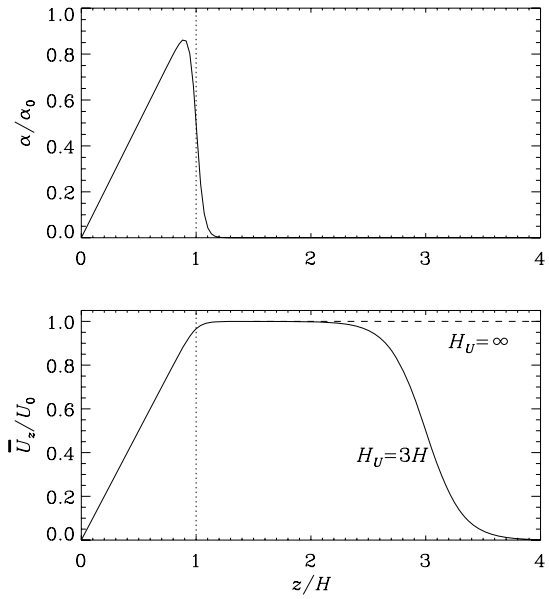

Figure 1. Profiles of α and $\overline{U}$ for $w_\alpha k_1 = 0.2$ and $w_U k_1 = 1$.

3 RESULTS

3.1 Kinematic behaviour of the solutions

When the magnetic field is weak, the back reaction via the Lorentz force and hence the α_M term are negligible. The value of R_m then does not enter into the theory. The effects of magnetic helicity fluxes are therefore not important, so we begin by neglecting the outflow or other transporters of magnetic helicity. For the linear α profile, we find that the critical value of C_α for dynamo action to occur is about 5.13. These solutions are oscillatory with a dimensionless frequency $\tilde{\omega} \equiv \omega/\eta_t k_1^2 = 1.64$. The oscillations are associated with the migration of the dynamo wave in the positive z direction. This is shown in Fig. 2 where we compare with the case of a perfectly conducting boundary condition at $z = H$ for which we find $C_\alpha^{\rm crit} = 7.12$ and $\tilde{\omega} = 2.28$.

The fact that there are oscillatory solutions to the α^2 dynamo is perhaps somewhat unusual, but it is here related to the fact that α changes sign about the equator. Similar solutions were first found by Shukurov, Sokolov & Ruzmaikin (1985) and analysed in detail by Baryshnikova & Shukurov (1987) and Rädler & Bräuer (1987). Oscillations have also been seen in other α^2 dynamos where α changes

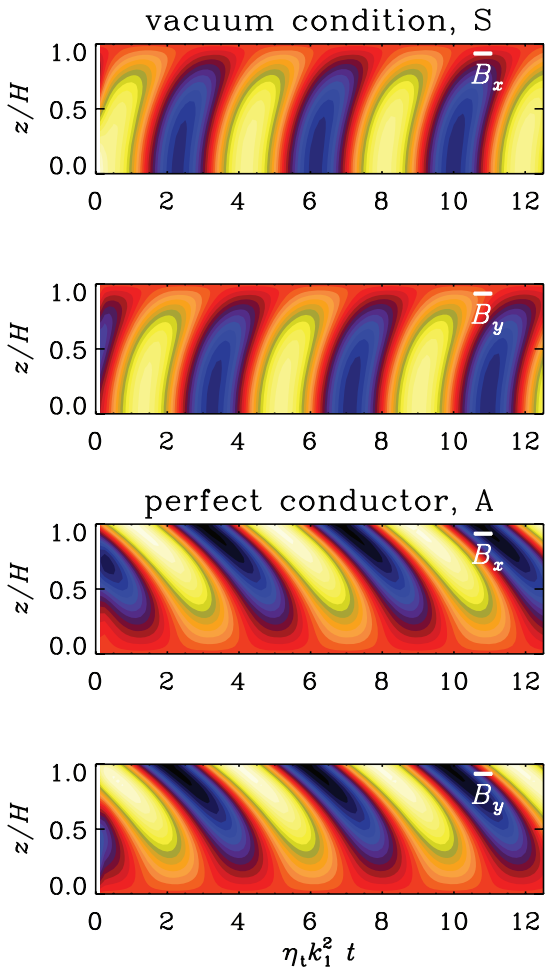

Figure 2. Space–time diagrams for $\overline{B}_x$ and $\overline{B}_y$ for the marginal values of C_α for $L = H$ with $C_U = 0$ and either the symmetric solution (S) with a vacuum boundary condition on $z = H$ or the antisymmetric solution (A) with the perfect conductor boundary condition. In both cases, the critical value $C_\alpha = 5.13$ is applied. Light (yellow) shades indicate positive values and dark (blue) shades indicate negative values.

sign with depth (Stefani & Gerbeth 2003; Rüdiger & Hollerbach 2004; Rüdiger, Elstner & Ossendrijver 2004; Giesecke, Ziegler & Rüdiger 2005) and in simulations of helically forced turbulence with a change of sign about the equator (Mitra et al. 2009). In the latter case, however, the outer boundaries were perfectly conducting. In our mean-field model, such a case is also oscillatory, as will be discussed below.

Note that here we have made the assumption that the solutions are symmetric about the mid-plane, i.e. $\overline{B}_i(z,t) = \overline{B}_i(-z,t)$ for $i = x$ or y. For the application to real systems, such a symmetry condition can only be justified if the symmetric solution is more easily excited than the antisymmetric one for which $\overline{B}_i(z,t) = -\overline{B}_i(-z,t)$ for $i = x$ or y. This is indeed the case when we adopt the vacuum condition at $z = H$, because the antisymmetric solution has $C_\alpha^{\rm crit} = 7.14$ in that case. However, this is not the case for the perfect conductor boundary condition for which the antisymmetric solution has $C_\alpha^{\rm crit} = 5.12$. We remark that there is a striking correspondence in the critical C_α values between the antisymmetric solution with perfect conductor boundary condition and the symmetric solution with vacuum condition on the one hand, and the symmetric solution with perfect conductor condition and the antisymmetric solution with vacuum condition on the other hand.

In the following, we consider both symmetric solutions using the vacuum boundary conditions, as well as antisymmetric ones using the perfect conductor boundary condition, which correspond in each case to the most easily excited mode. In the cases where we use a vacuum condition, we shall sometimes also apply an outflow. This makes the dynamo somewhat harder to excite and raises $C_\alpha^{\rm crit}$ from 5.12 to 5.60 for $C_U = 0.6$, but the associated magnetic helicity flux alleviates catastrophic quenching in the non-linear case. Alternatively, we consider an explicit removal of magnetic helicity to alleviate catastrophic quenching. In cases with perfect conductor boundary conditions, the most easily excited mode is antisymmetric about the equator, which corresponds to a boundary condition that permits a magnetic helicity flux through the equator. This would not be the case for the symmetric solutions.

3.2 Saturation behaviour for different values of $R_{\rm m}$

We now consider the saturated state for a value of C_α that is supercritical for dynamo action. In the following, we choose $C_\alpha = 8$. Throughout this paper, we assume $k_{\rm f}/k_1 = 10$ for the scale separation ratio. This corresponds to the value of 5 in Shukurov et al. (2006), where k_1 was defined differently. The dynamo saturates by building up negative $\alpha_{\rm M}$ when $\alpha_{\rm K}$ is positive. This diminishes the total α in equation (13) and saturates the dynamo. The strength of this quenching can be alleviated by magnetic helicity fluxes that lower the negative value of $\alpha_{\rm M}$.

We plot in Fig. 3 the dependence of the saturation field strength $\overline{B}_{\rm sat}$, defined here as the maximum of $|\overline{\boldsymbol{B}}(z)|$ at the time of saturation. To monitor the degree of quenching, we also plot in Fig. 3 the $R_{\rm m}$ dependence of the maximum of the negative value of $\alpha_{\rm M}$ at the time when the dynamo has saturated and reached a steady state. The maximum value of $-\alpha_{\rm M}$ is lowered by about 5 per cent from 1.8 to 1.7 in units of $\eta_{\rm t}k_1$ (see Fig. 3). Finally, we recall that for the α^2 dynamos considered here both $\overline{B}_x$ and $\overline{B}_y$ oscillate, but their relative phase shift is such that $\overline{\boldsymbol{B}}^2$ is non-oscillatory. The normalized cycle frequency, $\tilde{\omega} \equiv \omega/\eta_{\rm t}k_1$, is also plotted in Fig. 3 as a function of $R_{\rm m}$. It is somewhat surprising that ω does not strongly depend on $R_{\rm m}$. One may have expected that the cycle frequency could scale with the inverse resistive time $\eta\, k_1^2$. On the other hand, for oscillatory $\alpha\Omega$ dynamos the cycle frequency is known to scale with $\eta_{\rm t}k_1^2$ (Blackman & Brandenburg 2002), although that value could decrease if $\eta_{\rm t}(\overline{\boldsymbol{B}})$ is strongly quenched. However, simulations only give evidence for mild quenching (Brandenburg et al. 2008; Käpylä & Brandenburg 2009).

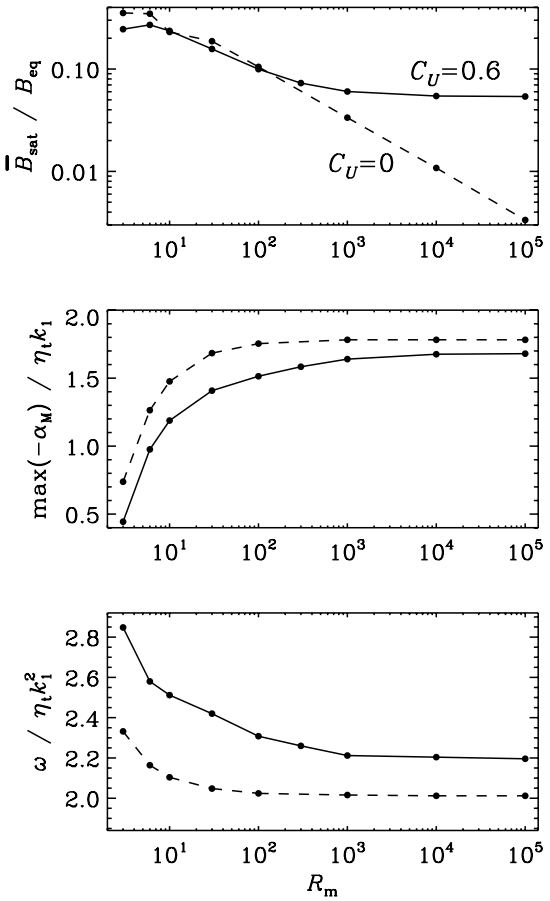

Figure 3. Scaling of the extremal value of $\alpha_{\rm M}$, the saturation field strength $\overline{B}_{\rm sat}$ and the cycle frequency ω with $R_{\rm m}$ and either $C_U = 0.6$ (solid lines) or $C_U = 0$ (dashed lines).

3.3 Helicity fluxes through the equator

We have seen in Section 3.1 that in the perfect conductor case the antisymmetric solutions are the most easily excited ones. The boundary conditions for antisymmetric solutions permit magnetic helicity transfer through the equator. A possible candidate for driving a flux through the equator would be a diffusive flux driven by the $\nabla\alpha_{\rm M}$ term. In Fig. 4, we plot the $R_{\rm m}$ dependence of max($-\alpha_{\rm M}$), $\overline{B}_{\rm sat}$ and $\tilde{\omega}$ for $\tilde{\kappa}_\alpha = 0.05$ and 0. Again, catastrophic α quenching is alleviated by the action of a magnetic helicity flux, but this time it is through the equator. The maximum value of $-\alpha_{\rm M}$ is lowered by 15 per cent from 2.35 to 2.15 in units of $\eta_{\rm t}k_1$ (see Fig. 4). Again, the cycle frequency is not changed significantly.

In Fig. 5, we compare the profiles of $\overline{h}_{\rm m}$, $\overline{h}_{\rm f}$, $\overline{F}_{\rm m}$ and $\overline{F}_{\rm f}$ for the most easily excited solution with vacuum and perfect conductor boundary conditions on $z = L$. In all cases, we have $\overline{h}_{\rm m} = \overline{h}_{\rm f} = 0$ at the mid-plane due to symmetry, and at $z = L$ we have $\overline{h}_{\rm m} = 0$ and $\overline{h}_{\rm f} \neq 0$. It turns out that the magnetic helicity flux of the small-scale field is balanced nearly exactly by that of the mean field. This agrees with the expectation of Blackman & Brandenburg (2003) who argued that both should be shed at nearly the same rate.

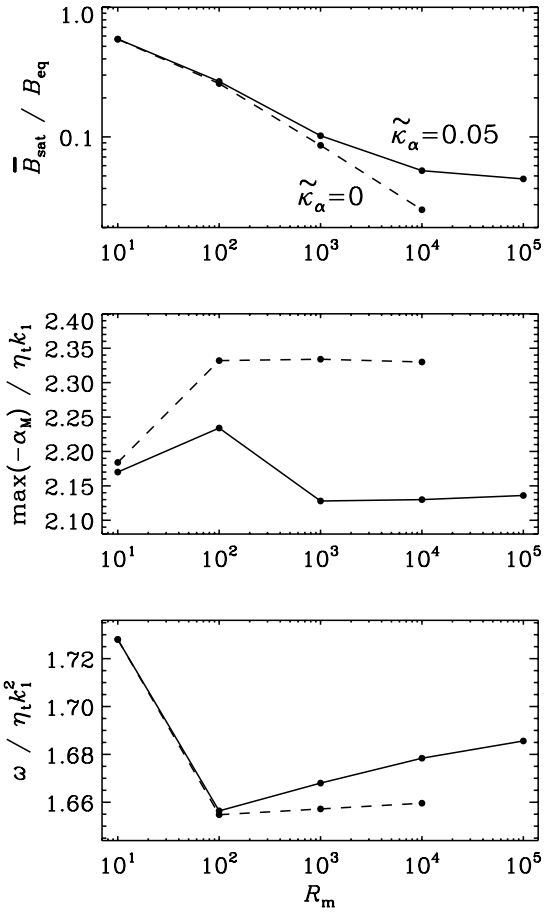

Figure 4. Same as Fig. 3, but for antisymmetric solutions in a model with perfect conductor boundary conditions with $C_U = 0$ and $\tilde{\kappa}_\alpha \equiv \kappa_\alpha/\eta_t = 0.05$ (solid lines) or 0 (dashed lines).

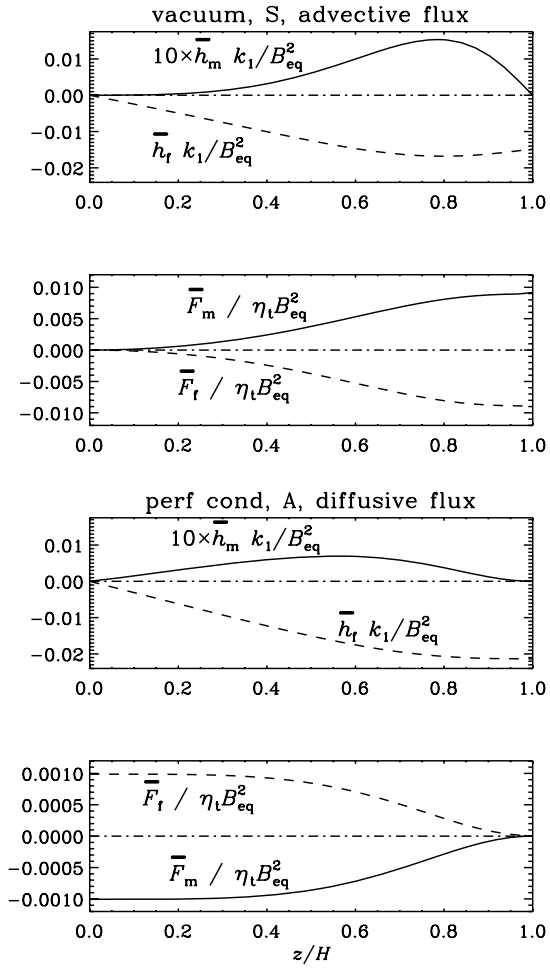

Figure 5. Mean magnetic helicity densities of mean and fluctuating fields as well as mean magnetic helicity fluxes of mean and fluctuating fields as functions of z for the S solution with vacuum boundary condition and advective flux with $C_U = 0.6$ (upper two panels) and for the A solution with perfect conductor boundary condition and diffusive flux with $\tilde{\kappa}_\alpha = 0.05$ (lower two panels). The profiles of $\overline{h}_{\rm f}$ have been scaled by a factor of 10 to make them more clearly visible. In all cases, we used $C_\alpha = 8$ and $R_{\rm m} = 10^5$.

The ad hoc assumption of a turbulent magnetic helicity flux is plausible and has of course been made in the past (Kleeorin et al. 2002), but its effect in alleviating catastrophic quenching has not yet been seen in earlier three-dimensional turbulence simulations (Brandenburg & Dobler 2001; Brandenburg 2001b). However, except for the effects of boundaries, the conditions in those simulation were essentially homogeneous and the gradients of magnetic helicity density may have been just too small. It would therefore be important to reconsider the question of diffusive helicity fluxes in future simulations of inhomogeneous helical turbulence.

3.4 Occasional removal of $\overline{h}_f$

Catastrophic quenching can also be alleviated by the artificial removal of small-scale magnetic fields (see equation 19). We consider the saturation strength of the magnetic field, $\overline{B}_{\rm sat}$, to characterize the alleviating effect of small-scale magnetic helicity losses. It is not surprising that the dynamo becomes stronger ($\overline{B}_{\rm sat}$ increases) when the fraction of small-scale field removal ϵ is increased (upper panel of Fig. 6) or the time interval of field removal is decreased (lower panel of Fig. 6). These dependencies follow approximate power laws,

$$\overline{B}_{\rm sat}/B_{\rm eq} \approx 0.17\,\epsilon^{1/2} \approx 0.024\,\left(\Delta t\,\eta_{\rm t}k_1^2\right)^{-1/2}, \qquad (26)$$

suggesting that even relatively small amounts of magnetic helicity removal in long intervals can have an effect.

We have also performed some numerical experiments where the magnetic helicity associated with the small-scale field is only removed near the surface layers. However, in those cases the catastrophic quenching was not notably alleviated. This can be explained by noting that, in the absence of additional magnetic helicity fluxes in the interior, there is still a build-up of $\overline{h}_{\rm f}$ in the interior which quenches the α effect catastrophically.

3.5 Magnetic helicity density and flux profiles

In an attempt to understand further the evolution of magnetic helicity we have performed calculations where the magnetic helicity flux of the fluctuating field was forced to vanish at the surface. This was done by choosing a profile for $\overline{U}$ that goes to zero at the surface. However, this invariably led to numerical problems. In order to clarify the origin of these problems we performed calculations with a taller domain, $L = 4H$, using the profiles shown in Fig. 1 and varying the value of H_U. For $H_U \to \infty$, the flux is still able to carry magnetic helicity away from the dynamo-active region into the outer layers $z > H$ (see Fig. 7). The cyclic dynamo in

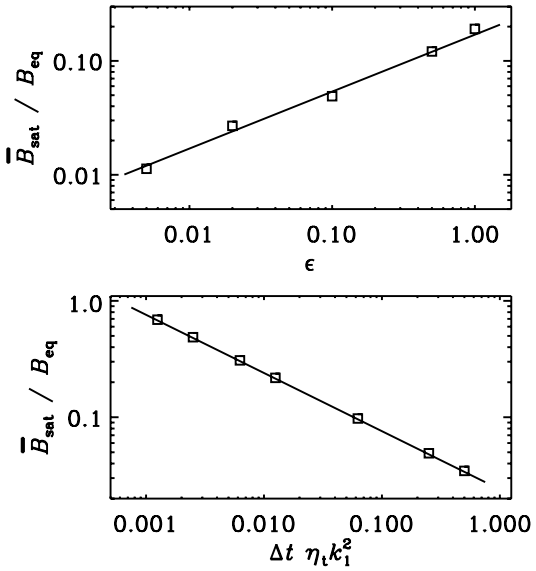

Figure 6. Saturation field strength versus ϵ for $\Delta t\eta_t k_1^2 = 0.25$ (upper panel) and versus $\Delta t\eta_t k_1^2$ for $\epsilon = 0.1$ (lower panel) in a model with $C_\alpha = 8$, $R_{\rm m} = 10^5$ and $C_U = C_{\rm S} = \kappa_\alpha = 0$.

$0 \le z \le H$ operates very much like in the case of a smaller domain (Fig. 2), except that the critical value of C_α is now lowered to $C_\alpha^{\rm crit} = 4.32$.

However, for $H_U = 3H$ a problem arises when a parcel of positive magnetic helicity that is shed early on from the dynamo-active region reaches the upper layers at $z \approx 3H$, through which now no magnetic helicity can be transmitted. Positive magnetic helicity piles up into a δ function near $z \approx 3H$ until it cannot be numerically resolved any more. At higher resolution, the evolution can be followed a little longer, but the problem cannot be removed. This demonstrates again that, once a magnetic helicity flux is initiated, there is no way to stop it locally. There is also no tendency for an annihilation between magnetic helicities of mean and fluctuating fields.

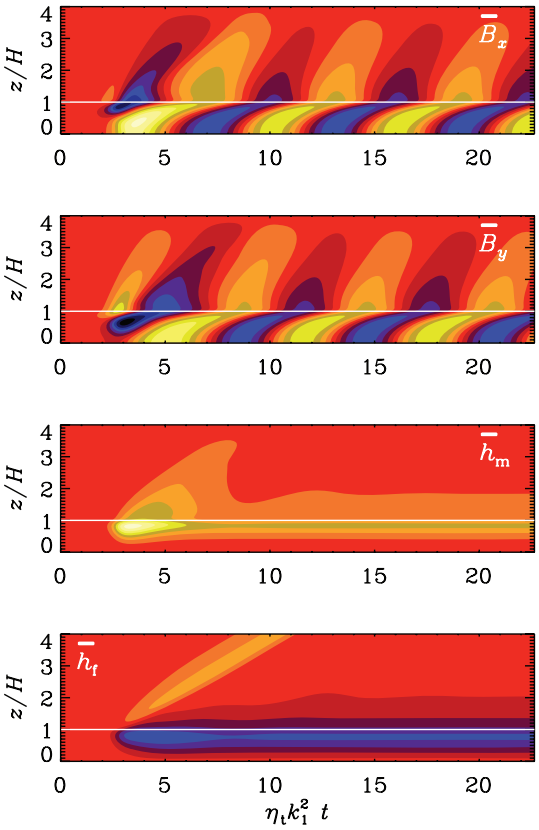

Figure 7. Space–time diagrams for $\overline{B}_x$ and $\overline{B}_y$, as well as the magnetic helicity densities $\overline{h}_{\rm m}$ and $\overline{h}_{\rm f}$ for $L = 4H$, $C_\alpha = 8$, $C_U = 0.6$ and $H_U \to \infty$. The white horizontal line marks the location $z = H$. Light (yellow) shades indicate positive values and dark (blue) shades indicate negative values.

The fact that positive magnetic helicity is produced is somewhat unexpected, because for $\alpha > 0$ the magnetic helicity production is positive definite. However, this can be traced back to the term $\eta_t \overline{\boldsymbol{J}} \cdot \overline{\boldsymbol{B}}$, which is part of $\overline{\boldsymbol{\mathcal{E}}} \cdot \overline{\boldsymbol{B}}$ on the right-hand side of equation (9). Since $\overline{\boldsymbol{J}} \cdot \overline{\boldsymbol{B}}$ is positive for positive $\alpha_{\rm K}$, it is clear that this term produces positive $\overline{h}_{\rm f}$ just *outside* the range where $\alpha_{\rm K}$ is finite and where it would produce $\overline{h}_{\rm f}$ of opposite sign.

In another experiment, we adopt a profile for $\overline{U}$ such that H_U is changed from ∞ to $3H$ only after a time $t\eta_t k_1^2 = 25$, which is when the parcel of positive $\overline{h}_{\rm f}$ has left the domain. Now it is indeed negative magnetic helicity that the dynamo tries to shed and that begins to pile up near $z = 3H$. However, even though the flux is relatively weak, the blockage at $z = 3H$ leads eventually to a problem and, again, to short-wavelength oscillations indicating that the solution is numerically no longer valid.

These results suggest that the magnetic helicity flux must be allowed to continue through the rest of the domain. Of course, in reality there is the possibility of various fluxes, including diffusive fluxes that have not been included in this particular model. We note, however, that model calculations with finite κ_α in equation (21) then confirm that $\overline{F}_{\rm f}(z, t)$ becomes constant in the outer parts.

3.6 Magnetic helicity with shear

It is remarkable that the magnetic helicity fluxes of the mean and fluctuating fields were always equally strong and of opposite sign. The point of this section is to underline that this is a particular property of the α^2 dynamo, and would not apply to $\alpha\Omega$ dynamos. In Fig. 8, we show the fluxes of the model with $C_\alpha = 8$ and $C_U = 0.6$, where we have varied $C_{\rm S}$ in the range from -8 to $+8$.

Shear gives rise to an additional magnetic helicity flux (Berger & Ruzmaikin 2000), and the perfect correspondence between magnetic helicity fluxes of opposite sign for mean and fluctuating fields is then broken. This additional flux of magnetic helicity is associated with the mean field and therefore does not, on its own, alleviate

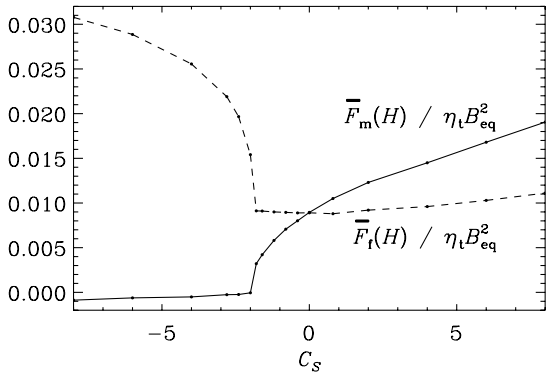

Figure 8. Dependence of $\overline{F}_{\rm m}(H)$ and $\overline{F}_{\rm f}(H)$ on the shear parameter for the S solution in a model with vacuum boundary condition, $C_\alpha = 8$, $C_U = 0.6$ and $R_{\rm m} = 10^5$.

catastrophic quenching. However, in this model we have neglected additional magnetic helicity fluxes arising from the shear that would be associated with the fluctuating field. An example is the Vishniac–Cho flux whose effect in a mean-field model was already studied in an earlier paper (Brandenburg & Subramanian 2005). For $C < -2$, the oscillating solutions are no longer preferred and a new solution branch emerges, where the solutions are now non-oscillatory. Those are also the type of solutions studied by Shukurov et al. (2006), where $C_S = -8$ was chosen, corresponding to the value -2 in their normalization.

4 CONCLUSIONS

The present simulations have confirmed that in finite domains magnetic helicity losses through local fluxes are able to alleviate catastrophic quenching. Without such fluxes, the energy of the mean field goes to zero in the limit of large R_m, while in the presence of such fluxes $|\overline{\boldsymbol{B}}|$ reaches values that are about 5 per cent of the equipartition value. We emphasize at this point that this applies to the case of an α^2 dynamo. For an $\alpha\Omega$ dynamo, the mean field can reach larger values, depending on the amount of shear. For example for the model shown in Fig. 8, the field strength in units of the equipartition value rises from 5 per cent without shear to about 36 per cent with negative shear ($C_S = -8$), while for positive shear it stays around 5 per cent. We also emphasize that the difference between the two cases with and without helicity fluxes is rather weak for $R_m \leq 10^3$, so one really has to reach values around $R_m \leq 10^4$ or $R_m \leq 10^5$. Such high values of R_m are not currently feasible with three-dimensional turbulence simulations.

The other surprising result is that it is not possible to dissipate magnetic helicity flux locally once it is initiated. If the magnetic helicity flux of the small-scale field has already left the dynamo-active domain, it has to stay constant in the steady state. By adding a diffusive flux, the boundary layer in the magnetic helicity of the small-scale field could be smoothed out, but this contribution would then carry the same amount of energy as before, although now by other means.

In the presence of shear, there are additional contributions to the magnetic helicity flux associated with the mean magnetic field. There are first of all the fluxes associated with the mean field itself, but those fluxes cannot contribute to alleviating catastrophic quenching on their own. However, earlier work has shown that in the presence of shear there are also additional contributions associated with the fluctuating field (Vishniac & Cho 2001; Subramanian & Brandenburg 2004, 2006). Those terms have not been included in the present work, because they have already been studied in an earlier paper (Brandenburg & Subramanian 2005).

Several new issues have emerged from the present study. The fact that diffusive magnetic helicity fluxes through the equator can alleviate catastrophic quenching is not surprising as such, but its effects in alleviating catastrophic saturation behaviour in three-dimensional turbulence simulations have not yet been reported (Brandenburg & Dobler 2001; Brandenburg 2001b). On the other hand, simulations of forced turbulence in spherical shells with an equator did show near-equipartition strength saturation fields (Mitra et al. 2009), although the values of R_m were typically below 20, so it was not possible to draw conclusions about catastrophic quenching. A new dedicated attempt in that direction would be worthwhile using driven turbulence, but now with a linear gradient of its intensity and in the Cartesian geometry.

In view of applications to the Sun and other stars, another important development would be to extend the present work to spherical domains. Again, some work in that direction was already reported in Brandenburg et al. (2007), but none of these models used diffusive fluxes, nor has any attempt been made to model the Sun. This would now be an important target for future research.

ACKNOWLEDGMENTS

We thank Anvar Shukurov for detailed comments and suggestions regarding an earlier version of the manuscript. We acknowledge the use of computing time at the Center for Parallel Computers at the Royal Institute of Technology in Sweden. This work was supported in part by the European Research Council under the AstroDyn Research Project 227952 and the Swedish Research Council grant 621-2007-4064.

REFERENCES

Baryshnikova Y., Shukurov A. M., 1987, Astron. Nachr., 308, 89
Berger M. A., Ruzmaikin A., 2000, J. Geophys. Res., 105, 10481
Blackman E. G., Brandenburg A., 2002, ApJ, 579, 359
Blackman E. G., Brandenburg A., 2003, ApJ, 584, L99
Blackman E. G., Field G. B., 2000a, ApJ, 534, 984
Blackman E. G., Field G. B., 2000b, MNRAS, 318, 724
Brandenburg A., 2001a, ApJ, 550, 824
Brandenburg A., 2001b, in Chossat P., Armbruster D., Iuliana O., eds, Nato ASI Series 26, Dynamo and Dynamics, a Mathematical Challenge. Kluwer, Dordrecht, p. 125
Brandenburg A., Dobler W., 2001, A&A, 369, 329
Brandenburg A., Schmitt D., 1998, A&A, 338, L55
Brandenburg A., Subramanian K., 2005, Astron. Nachr., 326, 400
Brandenburg A., Dobler W., Subramanian K., 2002, Astron. Nachr., 323, 99
Brandenburg A., Käpylä P. J., Mitra D., Moss D., Tavakol R., 2007, Astron. Nachr., 328, 1118
Brandenburg A., Rädler K.-H., Rheinhardt M., Subramanian K., 2008, ApJ, 687, L49
Cattaneo F., Hughes D. W., 1996, Phys. Rev. E, 54, R4532
Choudhuri A. R., Schüssler M., Dikpati M., 1995, A&A, 303, L29
Field G. B., Blackman E. G., 2002, ApJ, 572, 685
Giesecke A., Ziegler U., Rüdiger G., 2005, Phys. Earth Planet. Inter., 152, 90
Gruzinov A. V., Diamond P. H., 1994, Phys. Rev. Lett., 72, 1651
Gruzinov A. V., Diamond P. H., 1995, Phys. Plasmas, 2, 1941
Gruzinov A. V., Diamond P. H., 1996, Phys. Plasmas, 3, 1853
Käpylä P. J., Brandenburg A., 2009, ApJ, 699, 1059
Kleeorin N. I., Ruzmaikin A. A., 1982, Magnetohydrodynamics, 18, 116
Kleeorin N., Rogachevskii I., Ruzmaikin A., 1995, A&A, 297, 159
Kleeorin N., Moss D., Rogachevskii I., Sokoloff D., 2000, A&A, 361, L5
Kleeorin N., Moss D., Rogachevskii I., Sokoloff D., 2002, A&A, 387, 453
Kleeorin N., Moss D., Rogachevskii I., Sokoloff D., 2003, A&A, 400, 9
Krause F., Rädler K.-H., 1980, Mean-field Magnetohydrodynamics and Dynamo Theory. Pergamon Press, Oxford
Mitra M., Tavakol R., Käpylä P. J., Brandenburg A., 2009, Phys. Rev. Lett., submitted
Moffatt H. K., 1978, Magnetic Field Generation in Electrically Conducting Fluids. Cambridge Univ. Press, Cambridge
Parker E. N., 1979, Cosmical Magnetic Fields. Clarendon Press, Oxford
Parker E. N., 1993, ApJ, 408, 707
Pouquet A., Frisch U., Léorat J., 1976, J. Fluid Mech., 77, 321
Rädler K.-H., Bräuer H.-J., 1987, Astron. Nachr., 308, 101
Rogachevskii I., Kleeorin N., 2000, Phys. Rev. E, 61, 5202
Rüdiger G., Hollerbach R., 2004, The Magnetic Universe. Wiley-VCH, Weinheim
Rüdiger G., Elstner D., Ossendrijver M., 2003, A&A, 406, 15
Schmitt D., 1987, A&A, 174, 281
Seehafer N., 1996, Phys. Rev. E, 53, 1283

Shukurov, A. M., Sokolov, D. D., Ruzmaikin, A. A., 1985, Magn. Gidrodin., 3, 9
Shukurov A., Sokoloff D., Subramanian K., Brandenburg A., 2006, A&A, 448, L33
Stefani F., Gerbeth G., 2003, Phys. Rev. E, 67, 027302
Stix M., 1974, A&A, 37, 121
Subramanian K., Brandenburg A., 2004, Phys. Rev. Lett., 93, 205001
Subramanian K., Brandenburg A., 2006, ApJ, 648, L71
Vainshtein S. I., Cattaneo F., 1992, ApJ, 393, 165
Vishniac E. T., Cho J., 2001, ApJ, 550, 752
Yousef T. A., Brandenburg A., Rüdiger G., 2003, A&A, 411, 321

This paper has been typeset from a TEX/LATEX file prepared by the author.

IV

Astron. Nachr. / AN **331**, No. 1, 130 – 135 (2010) / **DOI** 10.1002/asna.200911308

Equatorial magnetic helicity flux in simulations with different gauges

D. Mitra[1,⋆], **S. Candelaresi**[2,3], **P. Chatterjee**[2], **R. Tavakol**[1], and **A. Brandenburg**[2,3]

[1] Astronomy Unit, School of Mathematical Sciences, Queen Mary University of London, Mile End Road, London E1 4NS, United Kingdom
[2] NORDITA, AlbaNova University Center, Roslagstullsbacken 23, SE-10691 Stockholm, Sweden
[3] Department of Astronomy, AlbaNova University Center, Stockholm University, SE-10691 Stockholm, Sweden

Received 2009 Nov 4, accepted Nov 16
Published online 2009 Dec 30

Key words Sun: magnetic fields – magnetohydrodynamics (MHD)

We use direct numerical simulations of forced MHD turbulence with a forcing function that produces two different signs of kinetic helicity in the upper and lower parts of the domain. We show that the mean flux of magnetic helicity from the small-scale field between the two parts of the domain can be described by a Fickian diffusion law with a diffusion coefficient that is approximately independent of the magnetic Reynolds number and about one third of the estimated turbulent magnetic diffusivity. The data suggest that the turbulent diffusive magnetic helicity flux can only be expected to alleviate catastrophic quenching at Reynolds numbers of more than several thousands. We further calculate the magnetic helicity density and its flux in the domain for three different gauges. We consider the Weyl gauge, in which the electrostatic potential vanishes, the pseudo-Lorenz gauge, where the speed of light is replaced by the sound speed, and the 'resistive gauge' in which the Laplacian of the magnetic vector potential acts as a resistive term. We find that, in the statistically steady state, the time-averaged magnetic helicity density and the magnetic helicity flux are the same in all three gauges.

1 Introduction

The generation of magnetic fields on scales larger than the eddy scale of the underlying turbulence in astrophysical bodies has posed a major problem. Magnetic helicity is believed to play an important role in this process (Brandenburg & Subramanian 2005a). The magnetic helicity density, defined by $\boldsymbol{A}\cdot\boldsymbol{B}$, where $\boldsymbol{B}=\boldsymbol{\nabla}\times\boldsymbol{A}$ is the magnetic field and $\boldsymbol{A}$ is the corresponding magnetic vector potential, is important because at large scales it is produced in many dynamos. This has been demonstrated for dynamos based on the α effect (Shukurov et al. 2006; Brandenburg et al. 2009), the shear-current effect (Brandenburg & Subramanian 2005b), and the incoherent α-shear effect (Brandenburg et al. 2008). The volume integral of the magnetic helicity density over periodic domains (as well as domains with perfect-conductor boundary conditions or infinite domains where the magnetic field and the vector potential decays fast enough at infinity) is a conserved quantity in ideal MHD. This conservation is also believed to be recovered in the limit of infinite magnetic Reynolds number in non-ideal MHD (Berger 1984). This implies that for finite (but large) magnetic Reynolds numbers magnetic helicity can decay only through microscopic resistivity. This would in turn control the saturation time and cycle periods of large-scale *helical* magnetic field which would be too slow to explain the observed variations of magnetic fields in astrophysical settings, such as for example the 11 year variation of the large-scale fields during the solar cycle.

A possible way out of this deadlock is provided by fluxes of magnetic helicity out of the domain (Blackman & Field 2000; Kleeorin et al. 2000). In the case of the solar dynamo, such a flux could be out of the domain, mediated by coronal mass ejections, or it could be across the equator, mediated by internal gradients within the domain. Several possible candidates for magnetic helicity fluxes have been proposed (Kleeorin & Rogachevskii 1999; Vishniac & Cho 2001; Subramanian & Brandenburg 2004).

In this paper we measure the diffusive flux across the domain with two different signs of magnetic helicity. This measurement, however, poses an additional difficulty due to the fact that neither the flux nor the magnetic helicity density remain invariant under the gauge transformation $\boldsymbol{A}\rightarrow\boldsymbol{A}+\boldsymbol{\nabla}\Lambda$, up to which the vector potential is defined. This constitutes a gauge problem. This problem, however, does not arise in homogeneous (or nearly homogeneous) domains with periodic or perfect-conductor boundary conditions, or in infinitely large domains where both the magnetic field and the vector potential decay fast enough at infinity. In these cases the volume integral of magnetic helicity is *gauge-invariant*, because surface terms vanish and $\boldsymbol{\nabla}\cdot\boldsymbol{B}=0$, so that $\int\boldsymbol{B}\cdot\boldsymbol{\nabla}\Lambda\,\mathrm{d}V=-\int\Lambda\boldsymbol{\nabla}\cdot\boldsymbol{B}\,\mathrm{d}V=0$. However, in practice we are often interested in finite or open domains with more realistic boundary conditions. Also, if we are to talk meaningfully about the exchange of magnetic helicity between two parts of the domain we need to evaluate changes in magnetic helicity densities locally even if the

⋆ Corresponding author: dhruba.mitra@gmail.com

integral of the magnetic helicity density over the whole domain is gauge-invariant. An important question then is how to calculate this quantity across arbitrary surfaces in numerical simulations. Ideally one would like to have a gauge-invariant description of magnetic helicity. A number of suggestions have been put forward in the literature (Berger & Field 1984; Subramanian & Brandenburg 2006). In practice, however, calculating the gauge-invariant volume integral of magnetic helicity poses an awkward complication and may not be the quantity relevant for dynamo quenching (Subramanian & Brandenburg 2006). In this paper, to partially address this question, we take an alternative view and try to compare and contrast the magnetic helicity and its flux across the domain in three different gauges that are often used in numerical simulations.

2 Model and background

The setup in this paper is inspired by the recent work of Mitra et al. (2009), who considered a wedge-shaped domain encompassing parts of both the southern and northern hemispheres. Direct numerical simulations (DNS) of the compressible MHD equations with an external force which injected negative (positive) helicity in the northern (southern) hemisphere shows a dynamo with polarity reversals, oscillations and equatorward migration of magnetic activity. It was further shown, using mean-field models, that such a dynamo is well described by an α^2 dynamo, where α has positive (negative) sign in the northern (southern) hemisphere. However, the mean-field dynamo showed catastrophic quenching, i.e., the ratio of magnetic energy to the equipartition magnetic energy decreases as $R_{\rm m}^{-1}$, where $R_{\rm m}$ is the magnetic Reynolds number. Such catastrophic quenching could potentially be alleviated by a mean flux of small-scale magnetic helicity across the equator (Brandenburg et al. 2009). Diffusive flux of this kind has previously been employed in mean-field models on empirical grounds (Covas et al. 1998; Kleeorin et al. 2000). Using a one-dimensional mean-field model of an α^2 dynamo with positive α in the north and negative in the south, it was possible to show that for large enough values of $R_{\rm m}$ catastrophic quenching is indeed alleviated (Brandenburg et al. 2009). However, three questions still remained:

1. Can such a diffusive flux result from DNS?
2. Is it strong enough to alleviate catastrophic quenching?
3. When is it independent of the gauge chosen?

In this paper we provide partial answers to these questions.

We proceed by simplifying our problem further, both conceptually and numerically, by considering simulations performed in a rectangular Cartesian box with dimensions $L_x \times L_y \times L_z$. The box is divided into two equal cubes along the z direction, with sides $L_x = L_y = L_z/2$. We shall refer to the xy plane at $z = 0$ as the 'equator' and the regions with positive (negative) z as 'north' and 'south' respectively. We shall choose the helicity of the external force such that it has negative (positive) helicity in the northern (southern) part of the domain. All the sides of the simulation domain are chosen to have periodic boundary conditions. The slowest resistive decay rate of the mean magnetic field is ηk_1^2, where η is the microscopic magnetic diffusivity and $k_1 = \pi/L_z$ is the lowest wavenumber of the domain.

We employ two different random forcing functions: one where the helicity of the forcing function varies sinusoidally with z (Model A) and one where it varies linearly with z (Model B). This also leads to a corresponding variation of the kinetic and small-scale current helicities in the domain. Model A minimizes the possibility of boundary effects, while Model B employs the same profile as that used in an earlier mean-field model (Brandenburg et al. 2009). The typical wavenumber of the forcing function is chosen to be $k_{\rm f} = 20k_1$ in Model A and $k_{\rm f} = 16k_1$ in Model B. An important control parameter of our simulations is the magnetic Reynolds number, $R_{\rm m} = u_{\rm rms}/\eta k_{\rm f}$, which is varied between 2 and 68, although we also present a result with a larger value of $R_{\rm m}$. This last simulation may not have run long enough and will therefore not be analyzed in detailed.

We perform DNS of the equations of compressible MHD for an isothermal gas with constant sound speed $c_{\rm s}$,

$$\mathrm{D}_t \boldsymbol{U} = -c_{\rm s}^2 \boldsymbol{\nabla} \ln \rho + \frac{1}{\rho} \boldsymbol{J} \times \boldsymbol{B} + \boldsymbol{F}_{\rm visc} + \boldsymbol{f}, \tag{1}$$

$$\mathrm{D}_t \ln \rho = -\boldsymbol{\nabla} \cdot \boldsymbol{U}, \tag{2}$$

$$\partial_t \boldsymbol{A} = \boldsymbol{U} \times \boldsymbol{B} - \eta \mu_0 \boldsymbol{J} - \boldsymbol{\nabla} \Psi, \tag{3}$$

where $\boldsymbol{F}_{\rm visc} = (\mu/\rho)(\nabla^2 \boldsymbol{U} + \frac{1}{3} \boldsymbol{\nabla} \boldsymbol{\nabla} \cdot \boldsymbol{U})$ is the viscous force when the dynamic viscosity μ is constant (Model A), and $\boldsymbol{F}_{\rm visc} = \nu(\nabla^2 \boldsymbol{U} + \frac{1}{3} \boldsymbol{\nabla} \boldsymbol{\nabla} \cdot \boldsymbol{U} + 2 \boldsymbol{\mathsf{S}} \ln \rho)$ is the viscous force when the kinematic viscosity ν is constant (Model B), $\boldsymbol{U}$ is the velocity, $\boldsymbol{J} = \boldsymbol{\nabla} \times \boldsymbol{B}/\mu_0$ is the current density, μ_0 is the vacuum permeability (in the following we measure the magnetic field in Alfvén units by setting $\mu_0 = 1$ everywhere), ρ is the density, Ψ is the electrostatic potential, and $\mathrm{D}_t \equiv \partial_t + \boldsymbol{U} \cdot \boldsymbol{\nabla}$ is the advective derivative. Here, $\boldsymbol{f}(\boldsymbol{x}, t)$ is an external random white-in-time helical function of space and time. The simulations were performed with the PENCIL CODE[1], which uses sixth-order explicit finite differences in space and third order accurate time stepping method. We use a numerical resolution of $128 \times 128 \times 256$ meshpoints.

These simulations in a Cartesian box capture the essential aspects of the simulations of Mitra et al. (2009) in spherical wedge-shaped domains. In particular, in this case we also observe the generation of large-scale magnetic fields which show oscillations on dynamical time scales, reversals of polarity and equatorward migration, as can be seen from the sequence of snapshots in Fig. 1 for a run with $R_{\rm m} = 68$. Here we express time in units of the expected turbulent diffusion time, $T = (\eta_{\rm t0} k_1^2)^{-1}$, where $\eta_{\rm t0} = u_{\rm rms}/3k_{\rm f}$ is used as the reference value (Sur et al. 2008).

Below we shall employ this setup to study the magnetic helicity and its flux. We shall discuss the issue of gauge-dependence in Sect. 5.

[1] http://www.nordita.org/software/pencil-code/

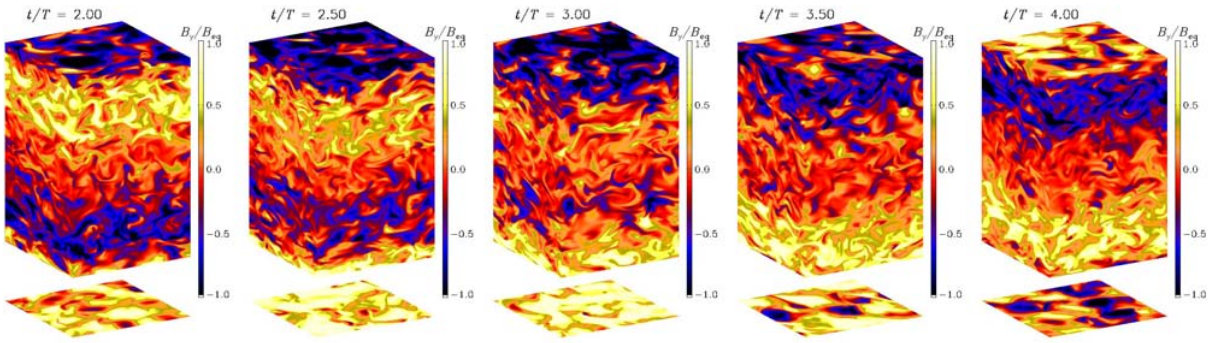

Fig. 1 (online colour at: www.an-journal.org) Visualization of the B_y component of the magnetic field on the periphery of the domain at different times showing the migration of magnetic patterns from the top and bottom boundaries toward the equator. Yellow (light) shades denote positive values and blue (dark) shades denote negative values. Time is measured in turbulent diffusion times, $T = (\eta_{\rm t0}k_1^2)^{-1}$, where $\eta_{\rm t0} = u_{\rm rms}/3k_{\rm f}$ is used as reference.

3 Magnetic helicity fluxes

Let us first summarize the role played by magnetic helicity and its fluxes in large-scale helical dynamos. In the spirit of mean-field theory, we define large-scale (or mean) quantities, denoted by an overbar, as a horizontal average taken over the x and y directions. In addition, we denote a volume average by angular brackets, $\langle\cdot\rangle$. The magnetic helicity density is denoted by

$$h^{\rm M} \equiv \boldsymbol{A}\cdot\boldsymbol{B}. \tag{4}$$

In general the evolution equation of $h^{\rm M}$ can be written down using the MHD equations, which yields

$$\partial_t h^{\rm M} = -2\boldsymbol{E}\cdot\boldsymbol{B} - \boldsymbol{\nabla}\cdot\boldsymbol{\mathcal{F}}^{\rm H}, \tag{5}$$

where

$$\boldsymbol{\mathcal{F}}^{\rm H} = \boldsymbol{E}\times\boldsymbol{A} + \Psi\boldsymbol{B} \tag{6}$$

is the magnetic helicity flux and $\boldsymbol{E}$ is the electric field, which is given by

$$\boldsymbol{E} = -\boldsymbol{U}\times\boldsymbol{B} + \eta\boldsymbol{J}. \tag{7}$$

Given that our system is statistically homogeneous in the horizontal directions, we consider the evolution equation for the horizontally averaged magnetic helicity density,

$$\partial_t \overline{h}^{\rm M} = -2\eta\overline{\boldsymbol{J}\cdot\boldsymbol{B}} - \boldsymbol{\nabla}\cdot\overline{\boldsymbol{\mathcal{F}}}^{\rm H}, \tag{8}$$

where the contribution from the full electromotive force, $\boldsymbol{U}\times\boldsymbol{B}$, has dropped out after taking the dot product with $\boldsymbol{B}$. However, the mean electromotive force from the fluctuating fields, $\overline{\boldsymbol{\mathcal{E}}} = \overline{\boldsymbol{u}\times\boldsymbol{b}}$, enters the evolution of the mean fields, so this contribution does not vanish if we consider separately the contributions to $\overline{h}^{\rm M}$ that result from mean and fluctuating fields, i.e.

$$\partial_t \overline{h}^{\rm M}_{\rm m} = 2\overline{\boldsymbol{\mathcal{E}}}\cdot\overline{\boldsymbol{B}} - 2\eta\overline{\boldsymbol{J}}\cdot\overline{\boldsymbol{B}} - \boldsymbol{\nabla}\cdot\overline{\boldsymbol{\mathcal{F}}}^{\rm H}_{\rm m}, \tag{9}$$

$$\partial_t \overline{h}^{\rm M}_{\rm f} = -2\overline{\boldsymbol{\mathcal{E}}}\cdot\overline{\boldsymbol{B}} - 2\eta\overline{\boldsymbol{j}\cdot\boldsymbol{b}} - \boldsymbol{\nabla}\cdot\overline{\boldsymbol{\mathcal{F}}}^{\rm H}_{\rm f}, \tag{10}$$

where

$$\overline{\boldsymbol{\mathcal{F}}}^{\rm H}_{\rm m} = \overline{\boldsymbol{E}}\times\overline{\boldsymbol{A}} + \overline{\Psi}\,\overline{\boldsymbol{B}}, \tag{11}$$

$$\overline{\boldsymbol{\mathcal{F}}}^{\rm H}_{\rm f} = \overline{\boldsymbol{e}\times\boldsymbol{a}} + \overline{\psi\boldsymbol{b}}, \tag{12}$$

and $\Psi = \overline{\Psi} + \psi$.

In mean-field dynamo theory one solves the evolution equation for $\overline{\boldsymbol{B}}$, so $\overline{\boldsymbol{\mathcal{F}}}^{\rm H}_{\rm m}$ is known explicitly from the actual mean fields. However, the evolution equation for $\overline{h}^{\rm M}_{\rm f}$ is not automatically obeyed in the usual mean-field treatment. This is the reason why in the dynamical quenching formalism this equation is added as an additional constraint equation. The terms $\overline{h}^{\rm M}_{\rm f}$ and $\overline{\boldsymbol{j}\cdot\boldsymbol{b}} \approx k_{\rm f}^2\overline{h}^{\rm M}_{\rm f}$ are coupled to the mean-field equations through an additional contribution to the α effect with a term proportional to $k_{\rm f}^2\overline{h}^{\rm M}_{\rm f}$. However, the coupling of the flux term $\overline{\boldsymbol{\mathcal{F}}}^{\rm H}_{\rm f}$ is less clear, because there are several possibilities and their relative importance is not well established.

In this paper we are primarily interested in $\overline{\boldsymbol{\mathcal{F}}}^{\rm H}_{\rm f}$ across the equator. We assume that this flux can be written in terms of the gradient of the magnetic helicity density via a Fickian diffusion law, i.e.,

$$\overline{\boldsymbol{\mathcal{F}}}^{\rm H}_{\rm f} = -\kappa_{\rm f}\boldsymbol{\nabla}\overline{h}^{\rm M}_{\rm f}, \tag{13}$$

where $\kappa_{\rm f}$ is an effective diffusion coefficient for the magnetic helicity density.

There are several points to note regarding Eq. (13). Firstly, both the magnetic helicity and its flux are *gauge-dependent*. Hence this expression should in principle depend on the gauge we choose. On the other hand, catastrophic quenching is a physically observable phenomenon that should not depend on the particular gauge chosen. Secondly, we recall that Eq. (13) is purely a conjecture at this stage, and it is the aim of this paper to test this conjecture. Thirdly, Eq. (13) is not the only form of flux of magnetic helicity possible. Two other obvious candidates are the advective flux and the Vishniac-Cho flux (Vishniac & Cho 2001).

Table 1 Dependence of $\overline{\boldsymbol{B}}^2$, normalized by $B_{\rm eq}^2$, the slopes of the three terms on the RHS of Eq. (10), normalized by $\eta_{\rm t0}B_{\rm eq}^2$, as well as the value of $\kappa_{\rm f}/\eta_{\rm t0}$.

Run	$R_{\rm m}$	$\overline{\boldsymbol{B}}^2$	$2\overline{\boldsymbol{\mathcal{E}}}\cdot\overline{\boldsymbol{B}}$	$2\eta\overline{\boldsymbol{j}\cdot\boldsymbol{b}}$	$\boldsymbol{\nabla}\cdot\overline{\boldsymbol{\mathcal{F}}}_{\rm f}^{\rm H}$	$\kappa_{\rm f}/\eta_{\rm t0}$
B1	2	1.1	9.42	-9.38	-0.04	0.41
B2	5	2.2	11.18	-11.14	-0.04	0.34
B3	15	2.0	4.54	-4.52	-0.02	0.27
B4	33	1.7	2.28	-2.27	-0.01	0.31
B5	68	0.8	1.15	-1.12	-0.03	0.34

However, none of them can be of importance to the problem at hand, because we have neither a large-scale velocity (thus ruling out advective flux) nor a large-scale shear (thus ruling out Vishniac-Cho flux).

4 Diffusive flux and $R_{\rm m}$ dependence

Let us postpone the discussion of the complications arising from the choice of gauge until Sect. 5 and use the *resistive gauge* for the results reported in this section, i.e. we set

$$\Psi=\eta\boldsymbol{\nabla}\cdot\boldsymbol{A}. \tag{14}$$

We then calculate $\overline{\mathcal{F}}_{\rm f}^{\rm H}$ and $\overline{h}_{\rm f}^{\rm M}$ as functions of z from our simulations, time-average both of them and use Eq. (13) to calculate $\kappa_{\rm f}$ from a least-square fit of $\overline{\mathcal{F}}_{\rm f}^{\rm H}$ versus $-\boldsymbol{\nabla}\overline{h}_{\rm f}^{\rm M}$ within the range $-1.3\le k_1z\le 1.3$. The values of $\kappa_{\rm f}$ as a function of $R_{\rm m}$ is given in the last column of Table 1.

In order to determine the relative importance of equatorial magnetic helicity fluxes, we now consider individually the three terms on the RHS of Eq. (10). Within the range $-1.3\le k_1z\le 1.3$, all three terms vary roughly linearly with z. We therefore determine the slope of this dependence. In Table 1 we compare these three terms at $k_1z=-1$, evaluated in units of $\eta_{\rm t0}k_1B_{\rm eq}^2$, as well as the value of $\kappa_{\rm f}/\eta_{\rm t0}$. In Fig. 2 we show the z dependence of these three terms for Run B5, where $R_{\rm m}=68$. The values of $\kappa_{\rm f}$ as a function of $R_{\rm m}$ is given in the last column of Table 1. The z dependence of $\overline{\mathcal{F}}_{\rm f}^{\rm H}$ and $\overline{h}_{\rm f}^{\rm M}$ is shown in the last panel of Fig. 2. Note that the two profiles agree quite well.

We point out that, near $z=0$, all simulations show either a local reduction in the gradients of the terms on the RHS of Eq. (10) or even a local reversal of the gradient. This is likely to be associated with a local reduction in dynamo activity near $z=0$, where kinetic helicity is zero. The non-uniformity of the turbulent magnetic field also leads to transport effects (Brandenburg & Subramanian 2005a) that may modify the gradient. However, we shall not pursue this question further here.

Looking at Table 1, we see that the terms $2\overline{\boldsymbol{\mathcal{E}}}\cdot\overline{\boldsymbol{B}}$ and $2\eta\overline{\boldsymbol{j}\cdot\boldsymbol{b}}$ balance each other nearly perfectly, and that only a small residual is then balanced by the diffusive flux divergence, $\boldsymbol{\nabla}\cdot\overline{\boldsymbol{\mathcal{F}}}_{\rm f}^{\rm H}$. For the values of $R_{\rm m}$ considered here, the terms $2\overline{\boldsymbol{\mathcal{E}}}\cdot\overline{\boldsymbol{B}}$ and $2\eta\overline{\boldsymbol{j}\cdot\boldsymbol{b}}$ scale with $R_{\rm m}$, while the dependence of $\boldsymbol{\nabla}\cdot\overline{\boldsymbol{\mathcal{F}}}_{\rm f}^{\rm H}$ on $R_{\rm m}$ is comparatively weak. If catastrophic quenching is to be alleviated by the magnetic helicity flux, one would expect that at large values of $R_{\rm m}$ the terms $2\overline{\boldsymbol{\mathcal{E}}}\cdot\overline{\boldsymbol{B}}$ and $\boldsymbol{\nabla}\cdot\overline{\boldsymbol{\mathcal{F}}}_{\rm f}^{\rm H}$ should balance. At the moment our values of $R_{\rm m}$ are still too small by about a factor of 30–60 (assuming that the same scaling with $R_{\rm m}$ persists). This result is compatible with that of earlier mean field models (Brandenburg et al. 2009). Consequently, we see that the energy of the mean magnetic field decreases with increasing $R_{\rm m}$ from 33 to 68; see Fig. 3. For larger values of $R_{\rm m}$ the situation is still unclear.

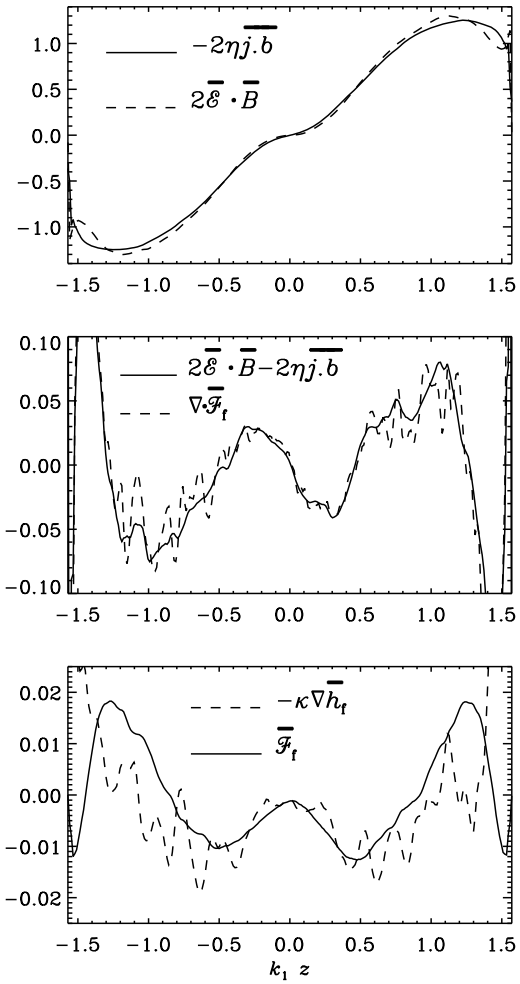

Fig. 2 z dependence of the terms on the RHS of Eq. (10) in the first two panels and in Eq. (13) for Run B5.

In Table 1, we also give the approximate values of $\kappa_{\rm f}/\eta_{\rm t0}$. Note that this ratio is always around 0.3 and independent of $R_{\rm m}$. This is the first time that an estimate for the diffusion coefficient of the diffusive flux has been obtained. There exists no theoretical prediction for the value of $\kappa_{\rm f}$ other than the naive expectation that such a term should be expected and that its value should be of the order of $\eta_{\rm t0}$.

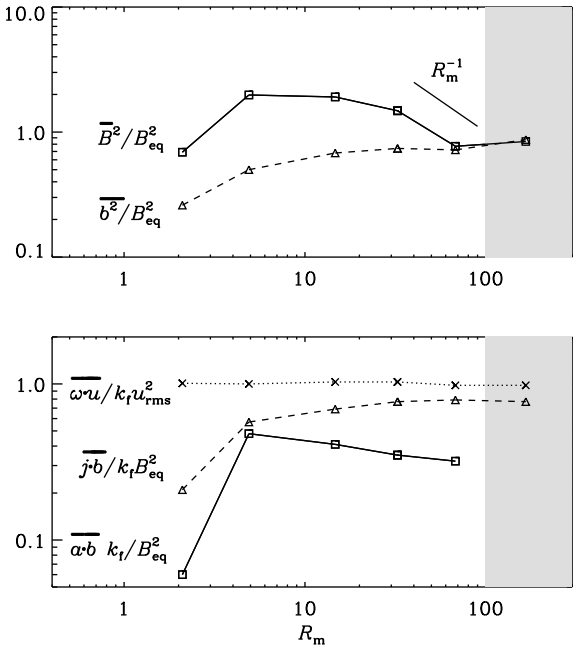

Fig. 3 $R_{\rm m}$ dependence of the normalized magnetic energy of the mean field, $\langle\overline{\boldsymbol{B}}^2\rangle/B_{\rm eq}^2$, and the fluctuating field, $\langle\boldsymbol{b}^2\rangle/B_{\rm eq}^2$, in the *upper panel* together with the normalized helicities of the small-scale magnetic field, $\overline{\boldsymbol{a}\cdot\boldsymbol{b}}\,k_{\rm f}/B_{\rm eq}^2$, the small-scale current density, $\overline{\boldsymbol{j}\cdot\boldsymbol{b}}/k_{\rm f}B_{\rm eq}^2$, and the small-scale velocity, $\overline{\boldsymbol{\omega}\cdot\boldsymbol{u}}/k_{\rm f}u_{\rm rms}^2$, at $k_1 z=-1$ (i.e. in the south) in the *lower panel*. (All three helicities are negative in the north and positive in the south.) The shaded areas indicate that the solutions are different in nature, and that the simulations may not have run for long enough.

This now allows us to state more precisely the point where the turbulent diffusive helicity flux becomes comparable with the resistive term, i.e. we assume $\kappa_{\rm f}\nabla^2\overline{\boldsymbol{a}\cdot\boldsymbol{b}}$ to become comparable with $2\eta\overline{\boldsymbol{j}\cdot\boldsymbol{b}}$. Using the relation $\overline{\boldsymbol{j}\cdot\boldsymbol{b}}\approx k_{\rm f}^2\overline{\boldsymbol{a}\cdot\boldsymbol{b}}$ (Blackman & Brandenburg 2002), which is confirmed by the current simulations within a factor of about 2 (see the second panel of Fig. 3), we find that

$$\kappa_{\rm f}/2\eta > (k_{\rm f}/k_1)^2, \quad (15)$$

where we have assumed that the Laplacian of $\overline{\boldsymbol{a}\cdot\boldsymbol{b}}$ can be replaced by a k_1^2 factor. Using our empirical finding, $\kappa_{\rm f}\approx\eta_{\rm t0}/3$, together with the definition $\eta_{\rm t0}/\eta\approx u_{\rm rms}/3\eta k_{\rm f}=R_{\rm m}/3$, we arrive at the condition

$$R_{\rm m} > 18(k_{\rm f}/k_1)^2\approx 4600 \quad \text{(for } \kappa_{\rm f} \text{ to be important)}, \quad (16)$$

where we have inserted the value $k_{\rm f}/k_1=16$ for the present simulations. Similarly, large values of $R_{\rm m}$ for alleviating catastrophic quenching by turbulent diffusive helicity fluxes were also found using mean-field modelling (Brandenburg et al. 2009). Unfortunately, the computing resources are still not sufficient to verify this in the immediate future.

5 Gauge-dependence of helicity flux

Let us now consider the question of gauge-dependence of the helicity flux. Equation (10) is obviously gauge-dependent. However, if, in the statistically steady state, $\overline{h}_{\rm f}^{\rm M}$ becomes independent of time, we can average this equation and obtain

$$\frac{\partial\overline{\mathcal{F}}_{\rm f}^{\rm H}}{\partial z}=-2\overline{\boldsymbol{\mathcal{E}}}\cdot\overline{\boldsymbol{B}}-2\eta\overline{\boldsymbol{j}\cdot\boldsymbol{b}}, \quad (17)$$

where $\overline{\mathcal{F}}_{\rm f}^{\rm H}$ refers to the z component of $\overline{\boldsymbol{\mathcal{F}}}_{\rm f}^{\rm H}$. On the RHS of this equation the two terms are gauge-independent. Therefore $\boldsymbol{\nabla}\cdot\overline{\boldsymbol{\mathcal{F}}}_{\rm f}^{\rm H}$ must also be gauge-independent. The same applies also to $\overline{\boldsymbol{\mathcal{F}}}_{\rm m}^{\rm H}$ and $\overline{\boldsymbol{\mathcal{F}}}^{\rm H}$; see Eq. (8). We have confirmed that, in the steady state, $\overline{h}_{\rm f}^{\rm M}$ is statistically steady and does not show a long-term trend; cf. Fig. 4 for the three gauges. We note that the fluctuations of $\overline{h}_{\rm f}^{\rm M}$ are typically much larger for the Weyl gauge than for the other two.

We now verify the expected gauge-independence explicitly for three different gauges: the *Weyl gauge*,

$$\Psi=0, \quad (18)$$

the *Lorenz gauge* (or pseudo-Lorenz gauge)[2], defined by

$$\partial_t\Psi=-c_\Psi^2\boldsymbol{\nabla}\cdot\boldsymbol{A}, \quad (19)$$

and the resistive gauge, defined by (14) above. We calculate the normalized magnetic helicity for both the mean and fluctuating parts and the respective fluxes for all the three gauges. These simulations are done for Model A with low $R_{\rm m}$ ($R_{\rm m}\approx 1.9$).

We find the transport coefficient $\kappa_{\rm f}$ in the way described in the previous section. A snapshot of the mean flux $\overline{\mathcal{F}}_{\rm f}^{\rm H}$ is plotted in the top panel of Fig. 5. The flux is different in all the three gauges. However, when averaged over the horizontal directions as well as time the fluxes in the three different gauges agree with one another as shown in the bottom panel of Fig. 5. We find the transport coefficient $\kappa_{\rm f}$ as described in the previous section and obtain the same value in all the three gauges.

6 Conclusion

In this paper we use a setup in which the two parts of the domain have different signs of kinetic and magnetic helicities. Using DNS we show that the flux of magnetic helicity due to small-scale fields can be described by Fickian diffusion down the gradient of this quantity. The corresponding diffusion coefficient is approximately independent of $R_{\rm m}$. However, in the range of $R_{\rm m}$ values considered here, the flux is not big enough to alleviate catastrophic quenching. The critical value of $R_{\rm m}$ for the flux to become important is proportional to the square of the scale separation ratio. In the present case, where this ratio is 16, the critical value of $R_{\rm m}$ is estimated to be 4600. We have also calculated the flux and the diffusion coefficient in the three gauges discussed above and have found the fluxes to be independent

[2] In fact, this is not the true Lorenz gauge because we use velocity of sound (Brandenburg & Käpylä 2007) instead of the velocity of light which appears in the original Lorenz gauge

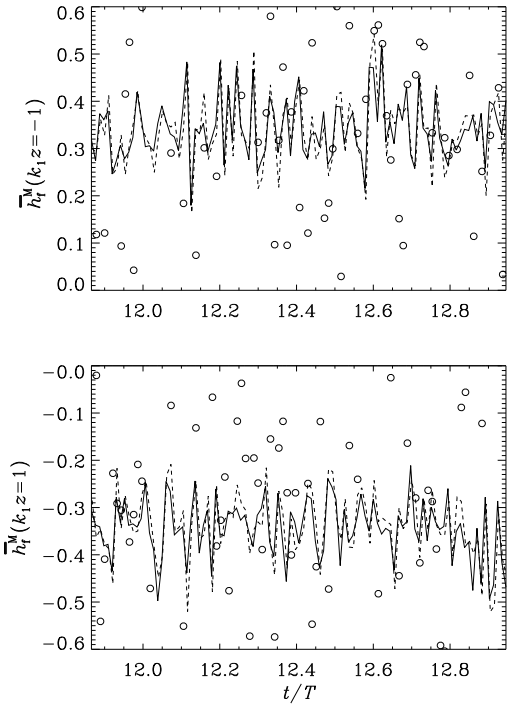

Fig. 4 Plot of $\overline{h}_{\rm f}^{\rm M}$ as a function of time in the statistically stationary state for $k_1 z = -1$ (south, *top panel*) and $k_1 z = 1$ (north, *bottom panel*) for the three different gauges, Weyl gauge (open circle), Lorenz gauge (line) and resistive gauge (broken line).

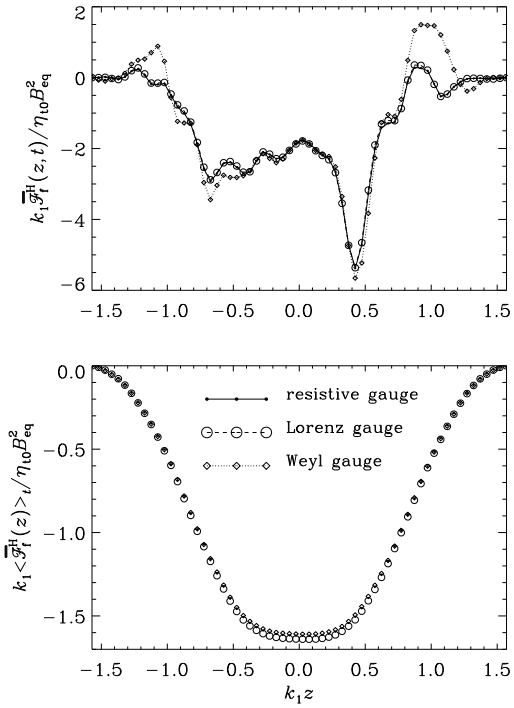

Fig. 5 Comparison of the flux $\overline{\mathcal{F}}_{\rm f}^{\rm H}(z,t)$ at a randomly chosen instant (*upper panel*) and its time average $\overline{\mathcal{F}}_{\rm f}^{\rm H}(z)$ for the three different gauges. Lorenz gauge (○), Weyl gauge (◇) and the resistive gauge (·). The instantaneous flux is plotted in the top panel and the time-averaged flux is plotted in the *bottom panel*.

of the choice of these gauges. This is explained by the fact that in the steady state the divergence of magnetic helicity flux is balanced by terms that are gauge-independent.

Several immediate improvements on this study spring to mind. One is to compare our results with the gauge-independent magnetic helicity of Berger & Field (1984) and the corresponding magnetic helicity flux. The second is to extend the present study to higher values of $R_{\rm m}$ to understand the asymptotic behavior of the flux. Finally, it may be useful to compare the results for different profiles of kinetic helicity to see whether or not our results depend on such details.

Acknowledgements. We thank the referee for a careful assessment of the paper and for pointing out an error in the original notation. The simulations were performed with the computers hosted by QMUL HMC facilities purchased under the SRIF initiative. We also acknowledge the allocation of computing resources provided by the Swedish National Allocations Committee at the Center for Parallel Computers at the Royal Institute of Technology in Stockholm and the National Supercomputer Centers in Linköping. This work was supported in part by the European Research Council under the AstroDyn Research Project 227952 and the Swedish Research Council grant 621-2007-4064. DM is supported by the Leverhulme Trust.

References

Berger, M.: 1984, GApFD 30, 79
Berger, M., Field, G.B.: 1984, JFM 147, 133
Blackman, E.G., Field, G.B.: 2000, ApJ 534, 984
Blackman, E.G., Brandenburg, A.: 2002, ApJ 579, 359
Brandenburg, A., Käpylä, P.J.: 2007, NJPh 9, 305
Brandenburg, A., Subramanian, K.: 2005a, PhR 417, 1
Brandenburg, A. & Subramanian, K.: 2005b, AN 326, 400
Brandenburg, A., Candelaresi, S., Chatterjee, P.: 2009, MNRAS 398, 1414
Brandenburg, A., Rädler, K.-H., Rheinhardt, M., Käpylä, P.J.: 2008, ApJ 676, 740
Covas, E., Tavakol, R., Tworkowski, A., Brandenburg, A.: 1998, A&A 329, 350
Kleeorin, N., Rogachevskii, I.: 1999, Phys Rev E 59, 6724
Kleeorin, N., Moss, D., Rogachevskii, I., Sokoloff, D.: 2000, A&A 361, L5
Mitra, D., Tavakol, R., Käpylä, P.J., Brandenburg, A.: 2009, astro-ph/0901.2364
Shukurov, A., Sokoloff, D., Subramanian, K., Brandenburg, A.: 2006, A&A 448, L33
Subramanian, K., Brandenburg, A.: 2004, Phys Rev Lett 93, 205001
Subramanian, K., Brandenburg, A.: 2006, ApJ 648, L71
Sur, S., Brandenburg, A., Subramanian, K.: 2008, MNRAS 385, L15
Vishniac, E.T., Cho, J.: 2001, ApJ 550, 752

V

Magnetic helicity transport in the advective gauge family

Simon Candelaresi,[1,2] Alexander Hubbard,[1] Axel Brandenburg,[1,2] and Dhrubaditya Mitra[1]
[1]*NORDITA, AlbaNova University Center, Roslagstullsbacken 23, SE-10691 Stockholm, Sweden*
[2]*Department of Astronomy, Stockholm University, SE 10691 Stockholm, Sweden*

(Received 29 October 2010; accepted 14 December 2010; published online 10 January 2011)

Magnetic helicity fluxes are investigated in a family of gauges in which the contribution from ideal magnetohydrodynamics takes the form of a purely advective flux. Numerical simulations of magnetohydrodynamic turbulence in this advective gauge family exhibit instabilities triggered by the build-up of unphysical irrotational contributions to the magnetic vector potential. As a remedy, the vector potential is evolved in a numerically well behaved gauge, from which the advective vector potential is obtained by a gauge transformation. In the kinematic regime, the magnetic helicity density evolves similarly to a passive scalar when resistivity is small and turbulent mixing is mild, i.e., when the fluid Reynolds number is not too large. In the dynamical regime, resistive contributions to the magnetic helicity flux in the advective gauge are found to be significant owing to the development of small length scales in the irrotational part of the magnetic vector potential.
 [doi:10.1063/1.3533656]

I. INTRODUCTION

Most astrophysical and laboratory plasmas are good conductors. This, together with high-speed flows and large length scales, nearly universal in the astrophysical context, makes for large magnetic Reynolds numbers. In the limit of infinitely large magnetic Reynolds number, and for domains with closed boundaries, total magnetic helicity is a conserved quantity. Here, an analogy can be drawn with mass conservation in domains whose boundaries are closed to mass flux. Furthermore, in open domains, the change in total mass is governed by the mass flux across open surfaces. In ideal magnetohydrodynamics (MHD), a similar property holds for the total magnetic helicity. But unlike mass, magnetic helicity depends on the choice of gauge. In the special case of the advective gauge, the magnetic helicity flux is given by the velocity times the magnetic helicity density,[1] making this gauge particularly interesting for studying pointwise properties of magnetic helicity. This is an important goal of this paper.

Magnetic helicity plays an important role in many fields of plasma physics and astrophysics, and has applications ranging from tokamaks and other plasma confinement machines, to dynamo action in the Sun and the galaxy. Our physical understanding of the role of magnetic helicity in MHD is greatly aided by concepts such as Taylor relaxation,[2] selective decay,[3] and the inverse cascade of magnetic helicity.[4]

Furthermore, magnetic helicity is a crucial ingredient of the turbulent dynamos which are believed to be the source of the equipartition magnetic fields in astrophysical bodies such as stars and galaxies.[5] In all such cases the characteristic length scales of the dynamo generated magnetic field exceed those of the fluid's energy carrying scale. In dynamo theory, the formation of such a large-scale magnetic field is typically possible through the α effect, which is nonzero for helical turbulent flows. In periodic boxes with helical turbulence, the α effect becomes strongly quenched when the (appropriately normalized) magnetic helicity in the small-scale field (i.e., scales that are smaller than the energy-carrying scale of turbulent fluid) is comparable to the helicity in the small-scale velocity. Conservation of magnetic helicity implies that the helicity in small- and large-scale fields will have comparable magnitudes, so the quenching of the large-scale dynamo will occur for weak large-scale fields. This α quenching[6,7] increases with scale separation and endures for as long as magnetic helicity is nearly conserved, a resistive time that scales with the magnetic Reynolds number $\mathrm{Re}_M \equiv UL/\eta$. The quenching is called "catastrophic" because for the Sun $\mathrm{Re}_M \sim 10^9$ and the galaxy $\mathrm{Re}_M \sim 10^{15}$, and their resistive timescales are problematically long. This rapid preresistive saturation of the dynamo generated field poses clear difficulties in applying theory to astronomical systems, but it may be possible to alleviate the problem through magnetic helicity fluxes.[8,9] It should also be pointed out that problems with catastrophic quenching are often not clearly seen in present-day simulations.[10–12] While trend lines suggest that catastrophic quenching will occur, simulations at currently achievable, low to intermediate Re_M and scale separation have shown significant large-scale fields.

There exists reasonable observational evidence is support of such fluxes of magnetic helicity. The Sun's surface magnetic field shows helical structures.[13,14] Further, it was shown[15] that the S-shaped (helical) regions which are active in the corona are precursors of coronal mass ejections (CMEs) and later[16] that those regions are more likely to erupt. This suggests that the Sun sheds magnetic helicity via CMEs. Since the Sun's large-scale magnetic field is believed to be generated by a helical dynamo[17,18] this shedding of magnetic helicity could play an important role in the 11 year solar cycle. Physically, magnetic helicity fluxes out of the domain can be mediated in many ways, such as the aforementioned CMEs for the Sun[19] or fountain flows in the case of galaxies.[17] In direct simulations magnetic helicity fluxes

are permitted by adjusting the boundary conditions, e.g., to vertical field boundaries, but their actual presence can be difficult to ascertain. Internal helicity fluxes have also been found to alleviate α quenching[18] in systems with internal boundaries that separate zones of oppositely signed kinetic and magnetic helicities.

A difficulty in addressing the generation and transport of magnetic helicity is its gauge dependence. We denote the magnetic vector potential as $\boldsymbol{A}$ such that $\boldsymbol{B}\equiv\boldsymbol{\nabla}\times\boldsymbol{A}$ is the magnetic field. Magnetic helicity $H\equiv\int_V \boldsymbol{A}\cdot\boldsymbol{B}dV$ is independent of the gauge for perfectly conducting boundaries, as well as periodic boundaries so long as $\boldsymbol{A}$ is also required to be periodic. However, if one wishes to study the transport of magnetic helicity for physically motivated systems a nonvolume integral formulation will be needed. Magnetic helicity *density*, $h\equiv\boldsymbol{A}\cdot\boldsymbol{B}$, the quantity we will be working with, clearly depends on the gauge choice for $\boldsymbol{A}$. The gauge dependence of fluxes of mean magnetic helicity contained in the fluctuating fields was examined via direct numerical simulations (DNS) for three different gauges,[20] and it was found that, averaged over time, they do not depend on the gauge choice. This is a result of the fact that, for sufficient scale separation, the magnetic helicity of the fluctuating field can be expressed as the density of linkages, which in turn is gauge-invariant.[21] This result implies that the study of specific but useful gauge choices is a meaningful task.

In this work we examine the properties of magnetic helicity density in a particularly interesting gauge-family which we call "advective" because in this gauge the effect of velocity on the evolution equation of magnetic helicity takes the form of a purely advective term. In previous work[1] this gauge choice was shown to be crucial to understanding magnetic helicity fluxes in the presence of shear, including the Vishniac–Cho flux.[22] Unfortunately, evolving $\boldsymbol{A}$ in this gauge proves numerically unstable. This may be related to earlier findings in smoothed particle MHD calculations.[23,24] There, the problem was identified as the result of an unconstrained evolution of vector potential components, which were argued to be connected with "poor accuracy with respect to "reverse-advection"-type terms."[23] Our present work clarifies that this instability is related to the excessive build-up of irrotational contributions to the magnetic vector potential. These contributions have no physical meaning, but discretization errors at small length scales can spoil the solution dramatically.

We shall therefore describe a novel method for obtaining $\boldsymbol{A}$ in this gauge by evolving it first in a numerically robust gauge and then applying a gauge transformation with a simultaneously evolved gauge potential. This will be referred to as the Λ method throughout the text. Next, we show that the magnetic helicity density in the advective gauge tends to be small even pointwise, provided turbulent effects are still weak, and discuss the analogy with passive scalar transport. We conclude by pointing out that resistive terms break the analogy with passive scalar advection through the emergence of a turbulently diffusive magnetic helicity flux.

II. MAGNETIC EVOLUTION EQUATIONS

A. Weyl and advective gauges

In this work we remain within nonrelativistic MHD and hence neglect the Faraday displacement current. So the current density is given by $\boldsymbol{J}=\boldsymbol{\nabla}\times\boldsymbol{B}$, where $\boldsymbol{B}$ is the magnetic field and we use units where the vacuum permeability is unity. At the core of MHD is the induction equation

$$\frac{\partial\boldsymbol{B}}{\partial t}=\boldsymbol{\nabla}\times(\boldsymbol{U}\times\boldsymbol{B}-\eta\boldsymbol{J}), \tag{1}$$

where $\boldsymbol{U}$ is the velocity and η is the molecular magnetic diffusivity. Equation (1) can be uncurled to give an evolution equation for the magnetic vector potential $\boldsymbol{A}$, but only up to a gauge choice. In the Weyl gauge, indicated by a superscript W on the magnetic vector potential, we just have

$$\frac{\partial\boldsymbol{A}^W}{\partial t}=\boldsymbol{U}\times\boldsymbol{B}-\eta\boldsymbol{J} \tag{2}$$

but by adding the gradient of a scalar field, the vector potential can be obtained in any other gauge. Of particular interest to this paper is the advective gauge

$$\boldsymbol{A}^a=\boldsymbol{A}^W+\boldsymbol{\nabla}\Lambda^{W:a}, \tag{3}$$

where $\Lambda^{W:a}$ is the gauge potential that transforms from $\boldsymbol{A}^W$ to $\boldsymbol{A}^a$. We demand that[25]

$$\frac{DA_i^a}{Dt}=-U_{j,i}A_j^a-\eta J_i. \tag{4}$$

Here, $D/Dt=\partial/\partial t+\boldsymbol{U}\cdot\boldsymbol{\nabla}$ is the advective derivative. Consequently one can show that $\Lambda^{W:a}$ obeys the evolution equation (see Appendix A)

$$\frac{D\Lambda^{W:a}}{Dt}=-\boldsymbol{U}\cdot\boldsymbol{A}^W. \tag{5}$$

Thus, to obtain $\boldsymbol{A}^a$, one can either solve Eq. (4) directly or, alternatively, solve Eq. (2) together with Eq. (5) and use Eq. (3) to obtain $\boldsymbol{A}^a$. A possible initial condition for $\Lambda^{W:a}$ would be $\Lambda^{W:a}=0$, in which case $\boldsymbol{A}^a=\boldsymbol{A}^W$ initially. For numerical reasons that will be discussed in more detail below, we shall consider the indirect method of obtaining the magnetic vector potential in the advective gauge, but starting from more numerically stable gauge which will be discussed in Sec. II B.

Variants on the advective gauge have seen significant use, particularly in DNS with constant imposed shear. Although the magnetic field in such simulations must obey shearing-periodic boundary condition the vector potential need not. In particular, the evolution Eq. (2) does not impose shearing-periodicity on the vector potential, while Eq. (4) does, enabling shearing-periodic numerical simulations[26] in terms of $\boldsymbol{A}$.

For our purposes, the importance of Eq. (4) lies in the form of the magnetic helicity density evolution equation. By writing the induction equation in the form

$$\frac{DB_i}{Dt} = + U_{i,j}B_j - (\boldsymbol{\nabla}\cdot\boldsymbol{U})B_i - (\boldsymbol{\nabla}\times\eta\boldsymbol{J})_i \tag{6}$$

computing $D(\boldsymbol{A}^a\cdot\boldsymbol{B})/Dt=\boldsymbol{A}^a\cdot D\boldsymbol{B}/Dt+\boldsymbol{B}\cdot D\boldsymbol{A}^a/Dt$, and noting that the $A_iU_{i,j}B_j$ terms from both equations cancel, we find that

$$\frac{Dh^a}{Dt} = -h^a\,\boldsymbol{\nabla}\cdot\boldsymbol{U} - \boldsymbol{\nabla}\cdot(\eta\boldsymbol{J}\times\boldsymbol{A}^a) - 2\eta\boldsymbol{J}\cdot\boldsymbol{B} \tag{7}$$

which shows that in ideal MHD ($\eta=0$) under the assumption of incompressibility ($\boldsymbol{\nabla}\cdot\boldsymbol{U}=0$) the magnetic helicity density in the advective gauge, $h^a=\boldsymbol{A}^a\cdot\boldsymbol{B}$ is just advected with the flow like a passive scalar, i.e.,

$$\frac{Dh^a}{Dt} = 0 \quad (\text{for } \eta=0 \text{ and } \boldsymbol{\nabla}\cdot\boldsymbol{U}=0). \tag{8}$$

In the general case with $\boldsymbol{\nabla}\cdot\boldsymbol{U}\neq 0$, the rate of change of the local value of h^a is given by $-\boldsymbol{\nabla}\cdot(h^a\boldsymbol{U})$, which is analogous to the continuity equation for the fluid density. However, for $\eta\neq 0$, there is also a source term

$$\frac{\partial h^a}{\partial t} = -2\eta\boldsymbol{J}\cdot\boldsymbol{B} - \boldsymbol{\nabla}\cdot\boldsymbol{F}^a, \tag{9}$$

as well as a resistive contribution to the magnetic helicity flux

$$\boldsymbol{F}^a = h^a\boldsymbol{U} + \eta\boldsymbol{J}\times\boldsymbol{A}^a. \tag{10}$$

In this paper we address the question how the $\eta\boldsymbol{J}\times\boldsymbol{A}^a$ contribution scales in the limit $\eta\to 0$, i.e., for large values of Re_M. It could either stay finite, just like the resistive energy dissipation $\eta\boldsymbol{J}^2$, which tends to a finite limit[5] as $\eta\to 0$, or it could go to zero like the source term $\eta\boldsymbol{J}\cdot\boldsymbol{B}$.[27,28]

B. Resistive and advecto-resistive gauges

There are two important issues to be noted about the equations discussed above. First, for numerical reasons, Eq. (2) is often replaced by

$$\frac{\partial\boldsymbol{A}^r}{\partial t} = \boldsymbol{U}\times\boldsymbol{B} + \eta\nabla^2\boldsymbol{A}^r, \tag{11}$$

where $\boldsymbol{A}^r$ is the magnetic vector potential in the resistive gauge and we have assumed that $\eta=$const; otherwise there would be an additional gradient term of the magnetic diffusivity that results from[29]

$$-\eta\boldsymbol{J} + \boldsymbol{\nabla}(\eta\boldsymbol{\nabla}\cdot\boldsymbol{A}) = \eta\nabla^2\boldsymbol{A} + (\boldsymbol{\nabla}\cdot\boldsymbol{A})\,\boldsymbol{\nabla}\,\eta. \tag{12}$$

This "resistive" gauge introduces an explicit, numerically stabilizing diffusion term for each component of $\boldsymbol{A}$. Second, and again for numerical reasons, Eq. (5) should be solved with a small diffusion term proportional to $\nabla^2\Lambda^{W:a}$. These two issues are actually connected and can be resolved by considering the gauge transformation

$$\boldsymbol{A}^{\mathrm{ar}} = \boldsymbol{A}^r + \boldsymbol{\nabla}\Lambda^{r:\mathrm{ar}} \tag{13}$$

which allows us to obtain the magnetic vector potential $\boldsymbol{A}^{\mathrm{ar}}$ in the advecto-resistive gauge obeying

$$\frac{DA_i^{\mathrm{ar}}}{Dt} = -U_{j,i}A_j^{\mathrm{ar}} + \eta\nabla^2A_i^{\mathrm{ar}}, \tag{14}$$

by solving Eq. (11) for $\boldsymbol{A}^r$ together with

$$\frac{D\Lambda^{r:\mathrm{ar}}}{Dt} = -\boldsymbol{U}\cdot\boldsymbol{A}^r + \eta\nabla^2\Lambda^{r:\mathrm{ar}} \tag{15}$$

and finally using the gauge transformation Eq. (13). For a full derivation of this equation we refer to Appendix B. Note that the microscopic magnetic diffusivity automatically enters the $\Lambda^{r:\mathrm{ar}}$ equation as a diffusion term, which implies that the $\Lambda^{r:\mathrm{ar}}$ equation is numerically well behaved.

The magnetic helicity density $h^{\mathrm{ar}}=\boldsymbol{A}^{\mathrm{ar}}\cdot\boldsymbol{B}$ in the advecto-resistive gauge can be calculated from the magnetic helicity in the resistive gauge through $h^{\mathrm{ar}}=h^r+\boldsymbol{\nabla}\Lambda^{r:\mathrm{ar}}\cdot\boldsymbol{B}$, and it obeys

$$\frac{\partial h^{\mathrm{ar}}}{\partial t} = -2\eta\boldsymbol{J}\cdot\boldsymbol{B} - \boldsymbol{\nabla}\cdot\boldsymbol{F}^{\mathrm{ar}} \tag{16}$$

with

$$\boldsymbol{F}^{\mathrm{ar}} = h^{\mathrm{ar}}\boldsymbol{U} - \eta(\boldsymbol{\nabla}\cdot\boldsymbol{A}^{\mathrm{ar}})\boldsymbol{B} + \eta\boldsymbol{J}\times\boldsymbol{A}^{\mathrm{ar}}. \tag{17}$$

For comparison, the evolution equation of the magnetic helicity density in the resistive gauge is given by an equation similar to Eq. (16), but with h^{ar} being replaced by h^r and $\boldsymbol{F}^{\mathrm{ar}}$ being replaced by

$$\boldsymbol{F}^r = h^r\boldsymbol{U} - (\boldsymbol{U}\cdot\boldsymbol{A}^r + \eta\boldsymbol{\nabla}\cdot\boldsymbol{A}^r)\boldsymbol{B} + \eta\boldsymbol{J}\times\boldsymbol{A}^r \tag{18}$$

which contains a nonadvective velocity driven flux of the form $(\boldsymbol{U}\cdot\boldsymbol{A}^r)\boldsymbol{B}$—even in the ideal case.

C. Numerical details

We perform simulations for isotropically forced, triply periodic cubic domains with sides of length 2π, as was done in earlier work.[28] The $\eta\boldsymbol{J}\cdot\boldsymbol{B}$ term in Eq. (9) implies (and past simulations have shown) that such a system will experience a slow, but steady production of magnetic helicity. This is the price to pay for a system which is both helical, providing us with a signal, and homogeneous, so avoiding extraneous magnetic helicity fluxes. In addition to the uncurled induction Eq. (11) and the gauge transformation evolution Eq. (15), we solve

$$\frac{D\boldsymbol{U}}{Dt} = -c_s^2\,\boldsymbol{\nabla}\,\ln\rho + \frac{c_L}{\rho}\boldsymbol{J}\times\boldsymbol{B} + \boldsymbol{F}_{\mathrm{visc}} + \boldsymbol{f}, \tag{19}$$

$$\frac{D\ln\rho}{Dt} = -\boldsymbol{\nabla}\cdot\boldsymbol{U}, \tag{20}$$

where c_s(=const) is the isothermal sound speed, ρ is the density, $\boldsymbol{F}_{\mathrm{visc}}=\rho^{-1}\boldsymbol{\nabla}\cdot(2\rho\nu\mathsf{S})$ is the viscous force, $\mathsf{S}_{ij}=\frac{1}{2}(U_{i,j}+U_{j,i})-\frac{1}{3}\delta_{ij}\boldsymbol{\nabla}\cdot\boldsymbol{U}$ is the rate of strain tensor, ν is the kinematic viscosity, $\boldsymbol{f}$ the forcing term, and $c_L=1$ is a prefactor that can be put to 0 to turn off the Lorentz force in kinematic calculations. As in earlier work[28] the forcing function consists of plane polarized waves whose direction and phase change randomly from one time step to the next. The modulus of its wavevectors is taken from a band of wavenumbers around a given average wavenumber k_f. The magnetic vector potential is initialized with a weak nonhelical sine wave

along one direction. In some cases we shall also consider solutions to the passive scalar equation in the incompressible case

$$\frac{DC}{Dt} = \kappa \nabla^2 C, \tag{21}$$

where κ is the passive scalar diffusivity. Following earlier work,[30] we impose a linear gradient in C, i.e., $C=Gz+c$, and solve for the departure from this gradient G, i.e.,

$$\frac{Dc}{Dt} = \kappa \nabla^2 c - GU_z, \tag{22}$$

where GU_z acts essentially as a forcing term.

We use the PENCIL CODE (http://pencil-code.googlecode.com)[31] to solve the equations for $\boldsymbol{A}^r$, $\boldsymbol{U}$, $\Lambda^{r:\mathrm{ar}}$, ρ, and in some cases also c. The calculations involving $\Lambda^{r:\mathrm{ar}}$ have been carried out with the publicly available revision r15211 (or similar) of the module special/advective_gauge.f90.

The control parameters we use are the magnetic Reynolds number Re_M, the magnetic Prandtl number Pr_M, and the Schmidt number

$$\mathrm{Re}_M \equiv \frac{u_{\mathrm{rms}}}{\eta k_f}, \quad \mathrm{Pr}_M \equiv \frac{\nu}{\eta}, \quad \mathrm{Sc} \equiv \frac{\nu}{\kappa}, \tag{23}$$

where u_{rms} is the root mean square velocity. We use $k_f=3k_1$ where k_1, the box wavenumber, is unity. The numerical resolution is varied between 32^3 and 256^3 meshpoints for values of Re and Re_M between 3 and 300. In one case we used $\mathrm{Re}_M \approx 800$, which was only possible because in that case we used $\mathrm{Pr}_M=10$, so that most of the energy gets dissipated viscously, leaving relatively little magnetic energy at high wavenumbers.[32]

III. IMPORTANCE OF MAGNETIC HELICITY DENSITY

A. Implications of Eq. (7) for dynamo theory

Magnetic helicity is not only of interest by being a conserved quantity in ideal MHD, but also by being the basis of a methodology to treat nonlinear helical MHD dynamos, namely, dynamical α quenching.[33] This methodology relates the current helicity in small scale fields with the magnetic helicity in small-scale fields, $\boldsymbol{j}\cdot\boldsymbol{b} \approx k_f^2 \boldsymbol{a}\cdot\boldsymbol{b}$, and invokes the magnetic α effect.[4] The evolution equation of the magnetic helicity density then becomes the evolution equation of the magnetic part of the α effect and the nonlinear evolution of the dynamo can be modeled. This methodology has been used successfully in systems where no net helicity flux is possible, and initial work invoking the methodology has captured the behavior of at least one system with finite helicity fluxes.[34] A major prediction of the theory is that in the absence of preferential helicity fluxes of small-scale fields, dynamo action is quenched to subequipartition mean field strengths. This phenomenon is sometimes referred to as "catastrophic quenching."

B. Magnetic helicity as passive scalar

In the advective and advecto-resistive gauges, the velocity appears in the evolution equations of the magnetic helicity density, Eqs. (7) and (16), only as advection terms in the fluxes, Eqs. (10) and (17). In the limit of ideal, incompressible, kinematic MHD, Eq. (7) is the evolution equation for a passive scalar. Even in nonideal MHD, if the fluctuations of h^{ar} due to the velocity field $\boldsymbol{U}$ were purely advective in nature (i.e., passive), magnetic helicity transport would only be resistive, large-scale advective, and/or turbulently diffusive. This would forbid the preferential export of small-scale magnetic helicity and might call for alternate solutions to the catastrophic quenching problem than helicity fluxes.[18]

While in ideal MHD ($\eta=0$) the resistive terms in Eq. (7) vanish, resistive terms need not vanish in the limit of $\eta \to 0$ (high Re_M). For example, in a turbulent flow, Ohmic dissipation $\eta \boldsymbol{J}^2$ tends to a finite value as η decreases. The need for nonresistive solutions to the build-up of magnetic helicity is therefore not a given. We will examine this by performing kinematic simulations where the Lorentz force is turned off, i.e., $c_L=0$.

If the Lorentz force is significant, the fluctuations of h^{ar} and $\boldsymbol{U}$ might be correlated beyond simple turbulent diffusion concerns (i.e., the fluctuations of h^{ar} could drive flow patterns). In the limit of incompressible flows, if the helicity is uniform, then the only source terms for helicity patterns of finite k are the resistive terms. The terms are small compared to dimensional estimates for the velocity terms when $\mathrm{Re}_M \gg 1$. We will look for signals of magnetic helicity transport by examining spectra of h^r and h^{ar} as (pseudo) scalars, together with spectra of a true passive scalar. As we will show, the advecto-resistive gauge is adequately efficient at turbulently diffusing magnetic helicity that no inertial range for the magnetic helicity density can be identified. However, the spectra of h^r help elucidate previous results[34] which found diffusive fluxes, but at values well below turbulent diffusivities. Instead, our spectra show clear diffusive behavior in the inertial range, but the mere existence of the inertial range implies nondiffusive behavior.

We emphasize that our spectra of h^r and h^{ar} have nothing to do with the usual magnetic helicity spectrum that obeys a realizability condition and whose integral gives the volume-averaged magnetic helicity. Here we are looking instead at the power of the magnetic helicity density as a (pseudo) scalar field. Our h_k measures the spatial variation of h. In order to avoid confusion, we shall refer to these spectra as scalar spectra.

IV. RESULTS

The results reported below for the magnetic helicity density h refer to the advecto-resistive gauge and have been obtained by the Λ method, unless indicated otherwise. The results from the direct method agree (Sec. IV A), but this method develops an instability when nonlinear effects become important (Sec. IV B).

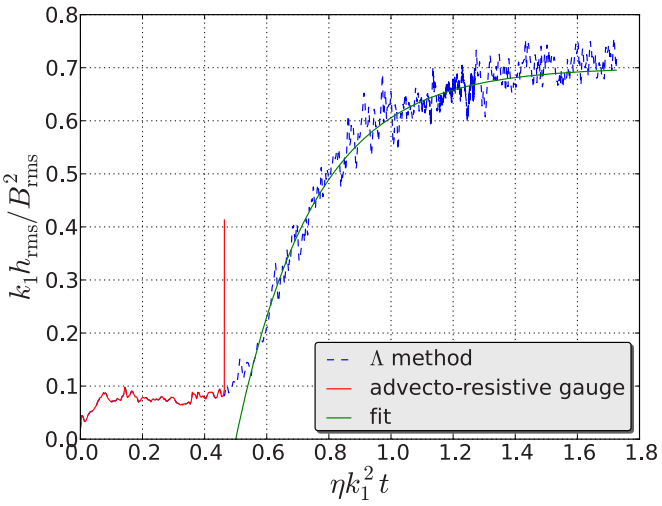

FIG. 1. (Color online) Time dependence of the normalized helicity for the advecto-resistive gauge with the direct method and the Λ method. Both curves agree perfectly just until the moment when the code develops an instability in the direct calculation. Time is normalized in terms of the magnetic diffusion time. The fit is an exponential relaxation to a constant value proportional to $1-\exp(-2\eta k_m^2 \Delta t)$, where $\Delta t = t - t_{\rm sat}$ is the time after the small-scale magnetic field has saturated (Ref. 28) and $k_m = 1.4 k_1$ has been chosen for a good fit.

A. Agreement between Λ and direct methods

To test the agreement between the Λ method and directly solving the induction equation in the advecto-resistive gauge, we plot the normalized rms magnetic helicity $h_{\rm rms}^{\rm ar}$ with respect to time (Fig. 1). Note that the nondimensional ratio $k_1 h_{\rm rms}^{\rm ar}/B_{\rm rms}^2$ has a well-defined plateau during the kinematic stage. Below we shall study the average value of this plateau as a function of magnetic Reynolds and Prandtl numbers. At the end of the kinematic phase, there is a slow saturation phase on a resistive time scale during which the large-scale field of the dynamo develops.[28] The results of the two calculations agree just until the moment when the direct calculation develops a numerical instability, whose nature will be discussed in more detail below. The perfect agreement until this moment can be taken as confirmation that the Λ method works and is correctly implemented in the code.

B. Nature of the instability

In Fig. 2 we show time series for a range of modest values of Re_M and two resolutions, 32^3 and 64^3. Reducing the magnetic Reynolds number may stabilize the system somewhat, but changing the resolution has no clear effect. In Fig. 3 we present data from equivalent runs that solve either Eq. (14) or alternatively Eqs. (11) and (15). We can see that the solutions match up until time $t = 220/c_s k_f$, where the run that solves Eq. (14) becomes unstable.

The key point is that when we evolve Eqs. (11) and (15), Λ never enters the equations for physical quantities. However, when we evolve Eq. (14), the magnetic field includes a term $\boldsymbol{\nabla}\times(\boldsymbol{\nabla}\Lambda)$, which, when computed numerically, is not zero. The first panel in Fig. 3 shows the power spectra of the vector potential. Comparing the advecto-resistive gauge (dashed/red) with resistive gauge (dotted/blue) we see that

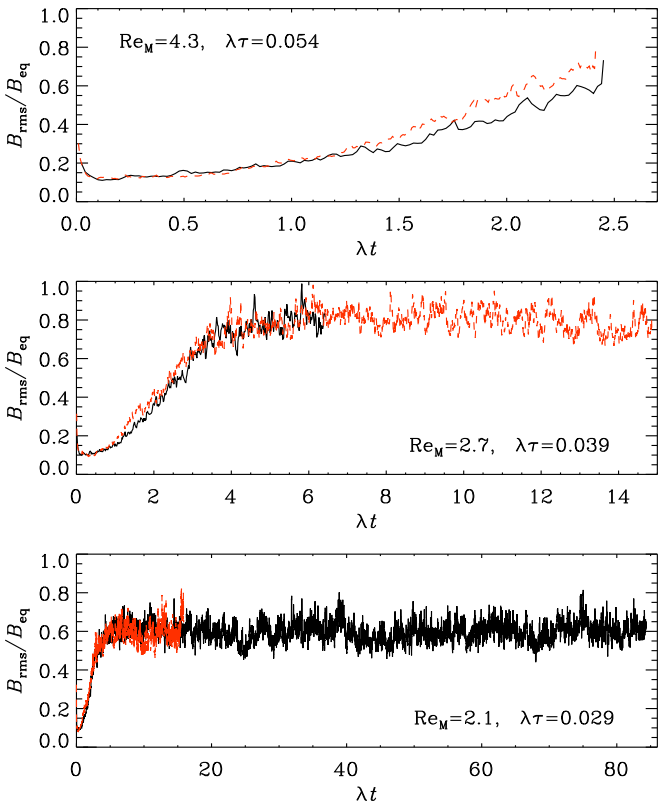

FIG. 2. (Color online) Evolution of $B_{\rm rms}/B_{\rm eq}$ for small values of Re_M between 4.3 (top) and 2.1 (bottom), using 32^3 (solid lines) and 64^3 (dashed, red lines). In each case, time on the abscissa is normalized by the growth rate λ, whose value is given in each panel in units of the inverse turnover time, $\tau^{-1} = u_{\rm rms} k_f$. The ends of each line mark the point when the solution became unstable.

$\boldsymbol{A}^{\rm ar} = \boldsymbol{A}^r + \boldsymbol{\nabla}\Lambda$ has significantly more power at high k than $\boldsymbol{A}^r$. Numerics cannot adequately handle the requirement that $\boldsymbol{\nabla}\times\boldsymbol{\nabla}\Lambda = 0$ at high k in the direct method, introducing errors in $\boldsymbol{B}$, as can be seen in the second panel. This fictitious increase in magnetic power at high k (and the attendant increase in current) result in a fictitious high k increase in the velocity field (third panel) that produces the numerical instability. The results of Fig. 2 suggest that the power of Λ (remembering that $\boldsymbol{J}$ includes that the third derivative of Λ) drops slowly enough at high k that numerical stability can only be achieved by enforcing an adequate resistivity η to damp Λ for only modest wavenumbers. Indeed, any gauge with large power in $\boldsymbol{A}$ for high k is expected to be numerically unstable, and the method sketched in Appendix A orAppendix B may be used to make the connection between analytical results in such a numerically unstable gauge and numerical results produced in a stable gauge.

C. Evolution of rms helicity density

In Fig. 4 we present a time series of the normalized rms magnetic helicity density in the kinematic regime (Lorentz force turned off, i.e., $c_L = 0$). In both the advecto-resistive and resistive gauges, there is an initial adjustment of the nondimensional ratio $k_1 h_{\rm rms}/B_{\rm rms}^2$ to a certain value, followed by a plateau. In the kinematic regime the magnetic helicity

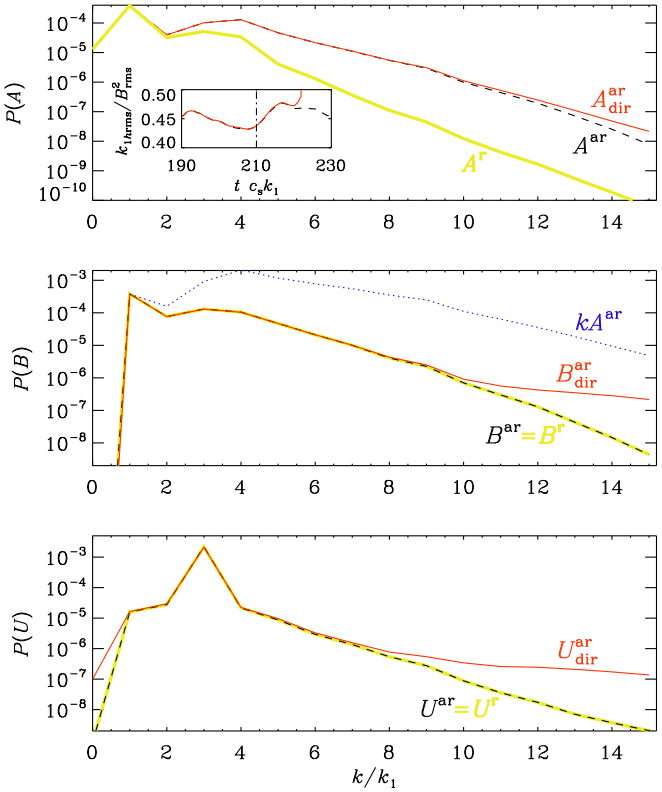

FIG. 3. (Color online) Power spectra of $\boldsymbol{A}$, $\boldsymbol{B}$, and $\boldsymbol{U}$ for two runs that are identical except that the first run solves for $\boldsymbol{A}^{\rm ar}$ directly while the second solves for $\boldsymbol{A}^{r}$ and Λ. In the top panel we plot the spectrum of $\boldsymbol{A}$ obtained either via $\boldsymbol{A}^{\rm ar}=\boldsymbol{A}^{r}+\boldsymbol{\nabla}\Lambda$ (dashed) or directly, $\boldsymbol{A}^{\rm ar}_{\rm dir}$ (solid/red), and compare with $\boldsymbol{A}^{r}$ (thick gray/yellow), showing that the vector potential in the advecto-resistive gauge has much more power at high k. The inset shows the time evolution of the normalized $h_{\rm rms}$ shortly before the time of the numerical instability. The dash-dotted line indicates the time for which the power spectra is taken. In the second panel we present magnetic energy spectra obtained in the direct gauge (solid/red), with the Λ method (dashed/black) as well as $k\boldsymbol{A}^{\rm ar}$ (dotted/blue), showing that there is significant power in the irrotational part of $\boldsymbol{A}$. We see that in the direct calculation of $\boldsymbol{A}^{\rm ar}$ the numerics are unable to adequately handle the high wavenumber power of $\boldsymbol{A}^{\rm ar}$ with consequences for the velocity seen in the last panel (solid/red line). The spectra of $\boldsymbol{B}$ and $\boldsymbol{U}$ agree for resistive and advecto-resistive gauges (thick gray/yellow line underneath the dashed black line) because the evaluation of the curl of a gradient has been avoided (last two panels). The three spectra are all taken for $t=210/c_s k_1$.

density is passive and the advection term in the advecto-resistive gauge merely serves to turbulently diffuse any local concentrations of $h^{\rm ar}$. Therefore there cannot be any spontaneous growth of $h^{\rm ar}$, except for effects from the resistive terms in the early adjustment phase. Turbulent diffusion itself, on the other hand, cannot generate variance of $h^{\rm ar}$.

In Figs. 5 and 6 we plot the height of the rms-magnetic helicity density plateau as a function of Re_M for several values of the magnetic Prandtl number and constant forcing amplitude. The differences between the evolution equations for h^{r} and $h^{\rm ar}$ are contained entirely in the flux terms so the volume integral of h is the same in the two gauges. Any difference between the rms values of h therefore is due to spatial fluctuations generated by the flux terms.

We fit the data points in Fig. 5 with functions of the form

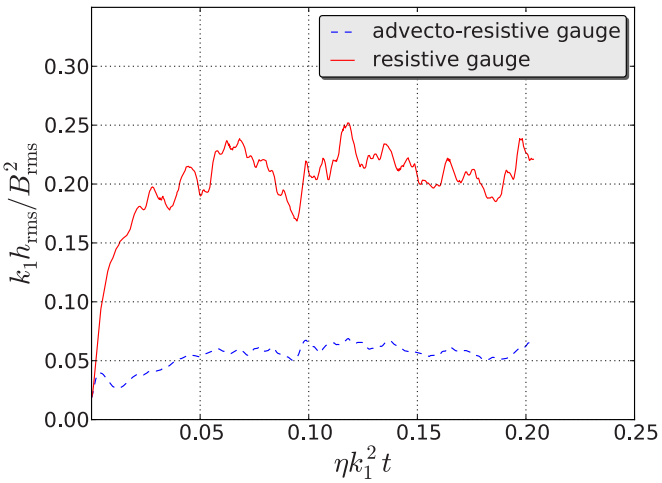

FIG. 4. (Color online) Time dependence of the rms values for the helicity in the advecto-resistive (solid/red) and resistive (dashed/blue) gauges with the Lorentz force switched off, i.e., $c_L=0$ in both cases.

$$\frac{k_1 h^{\rm ar}}{B^2_{\rm rms}} = c\mathrm{Re}_M^{-a}(1+b\mathrm{Re}_M^{2a}). \tag{24}$$

The fit results for the parameters are presented in Table I. Of interest is c, which increases with Pr_M and scales approximately with $\mathrm{Pr}_M^{1/2}$. A more general, although less accurate fit is given by

$$\frac{k_1 h^{\rm ar}}{B^2_{\rm rms}} \approx 3\mathrm{Re}_M^{-1}\left[1+\left(\frac{\mathrm{Re}_M/\mathrm{Pr}_M^{1/3}}{50}\right)^2\right] \tag{25}$$

see Fig. 7.

It is clear that high wavenumber fluid eddies (which are damped for small Re, i.e., large Pr_M, contribute significantly to $h^{\rm ar}_{\rm rms}$ for $\mathrm{Re}_M>100$, while from Fig. 6 we see that they do not contribute to $h^{r}_{\rm rms}$. That these eddies could contribute in the advecto-resistive gauge is to be expected as the advective

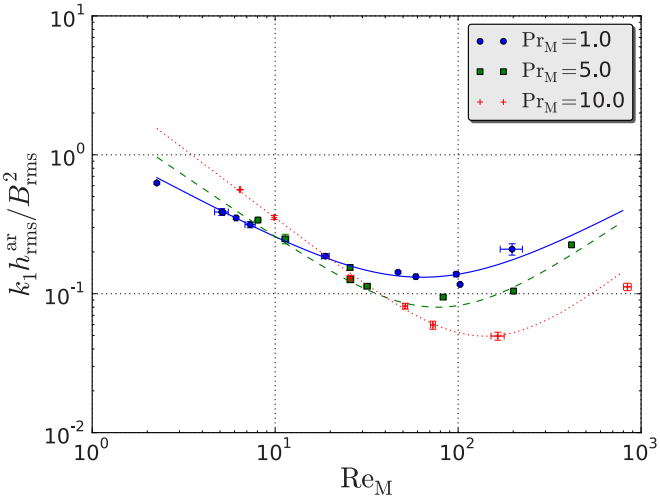

FIG. 5. (Color online) Re_M dependence of $k_1 h^{\rm ar}_{\rm rms}/B^2_{\rm rms}$ for the kinematic phase. Values are averages over times where they reach a stationary state. The curves represent fits according to Eq. (24).

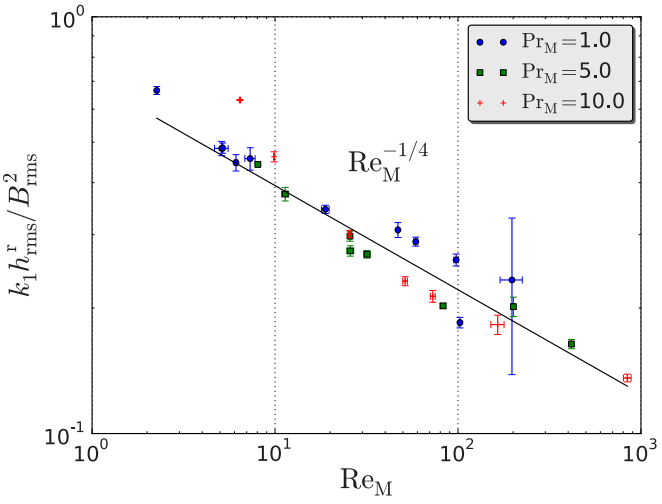

FIG. 6. (Color online) Re_M dependence of $k_1 h^r_{\rm rms}/B^2_{\rm rms}$ for the kinematic phase. Values are averages over times where they reach a stationary state. A $-1/4$ power law can be seen.

nature of that gauge implies the existence of an efficient turbulent cascade; the fact that they do contribute there and that the $\eta \boldsymbol{J}\times\boldsymbol{A}^{\rm ar}$ and $\eta(\boldsymbol{\nabla}\cdot\boldsymbol{A}^{\rm ar})\boldsymbol{B}$ terms remain important implies that resistive terms both become important at small length scales and have nondissipative effects. This is explained by the fact that $\boldsymbol{A}^{\rm ar}$ develops a strong high-k tail; see also Fig. 3. This is confirmed in Fig. 8, which shows that the resistive magnetic helicity fluxes in the advecto-resistive gauge are proportional to Re_M. In this gauge the rms resistive helicity fluxes are therefore independent of the actual value of the resistivity, staying finite even in the high Re_M limit. This is quite different from the resistive magnetic helicity fluxes in the resistive gauge, and the global magnetic helicity dissipation (which is gauge-independent): both terms are only proportional to $\mathrm{Re}_M^{1/2}$ and, after multiplying with η these terms tend to zero for $\mathrm{Re}_M \to \infty$.

D. Comparison with passive scalar

In Fig. 9 we present scalar spectra of the magnetic helicity density for both the resistive and advecto-resistive gauges and for the passive scalar concentration c, in the kinematic (arbitrary units) and saturated regimes. The passive scalar spectrum shows a peak at the forcing scale, $k_f/k_1=3$, followed by an approximate $k^{-5/3}$ subrange and an exponential diffusive subrange. As long as the magnetic energy density is still small compared with the kinetic energy density, the field exhibits exponential growth and a Kazantsev $k^{3/2}$ energy spectrum, which is well seen in simulations even at magnetic Prandtl numbers of unity both with and without

TABLE I. Fit parameters for Eq. (24) and Fig. 5.

Pr_M	a	b	c	Line type
1	0.7	3×10^{-3}	1.2	Solid/blue
5	0.9	4×10^{-4}	2.0	Dashed/green
10	1.0	5×10^{-5}	3.5	Dotted/red

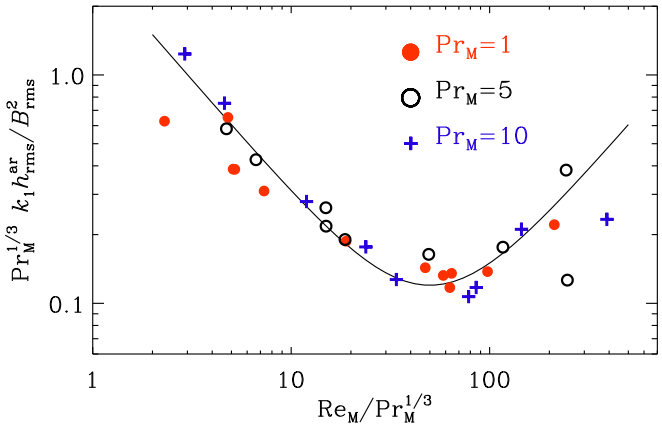

FIG. 7. (Color online) Dependence of $k_1 h^{\rm ar}_{\rm rms}/B^2_{\rm rms}$, scaled by $\mathrm{Pr}_M^{1/3}$ on $\mathrm{Re}_M/\mathrm{Pr}_M^{1/3}$ for the kinematic phase and $\mathrm{Pr}_M=1$ (filled circles), 5 (open circles), and 10 (plus signs). The solid line represents the fit of Eq. (25).

kinetic helicity in the velocity field.[35] This $k^{3/2}$ spectrum is also reflected in the scalar spectrum of $h^{\rm ar}$. The scalar spectrum of h^r is somewhat steeper and closer to k^2, indicating that h^r is dominated by white noise in space at large scales.

The saturated regime exhibits some interesting properties. The pronounced peak of the power of the passive scalar at the driving scale is easily understood as being due to the source of c. However, the magnetic helicity density in the resistive gauge shows a significant peak there as well, while it does not in the advecto-resistive gauge. This implies that the velocity term in Eq. (18) generates significant spatial variations in the magnetic helicity density—even in the absence of external modulations. As in dynamical α quenching, h influences the α effect, this suggests a way to quantify the appropriateness of different gauge choices: systems where spatial and temporal fluctuations in α can be adequately constrained would allow one to determine whether spatial fluctuations in h, as seen in Fig. 9, are fictitious as suggested by the advecto-resistive gauge or not.

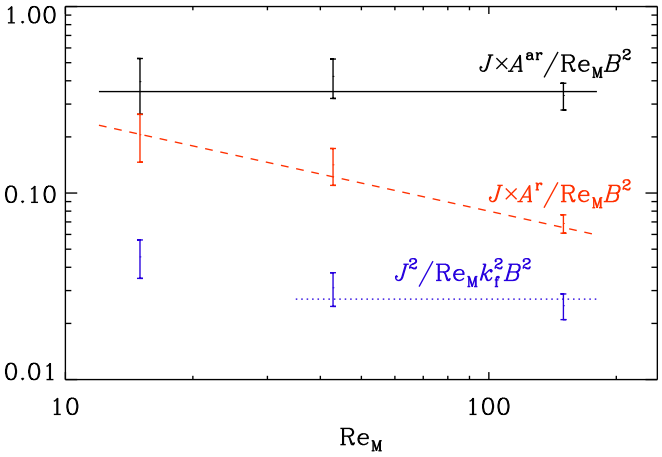

FIG. 8. (Color online) Re_M scaling of the rms value of $\boldsymbol{J}\times\boldsymbol{A}$, normalized by $\mathrm{Re}_M B^2_{\rm rms}$, for the advecto-resistive and resistive gauges. The solid line represents constant scaling, i.e., $\eta\boldsymbol{J}\times\boldsymbol{A}^{\rm ar}\approx$const, while the dashed line represents inverse square root scaling, i.e., $\eta\boldsymbol{J}\times\boldsymbol{A}^{r}\propto\mathrm{Re}_M^{-1/2}$, for three runs with $\mathrm{Pr}_M=1$ in the saturated regime. The dotted/blue line shows that ηJ^2, properly normalized, is approximately constant.

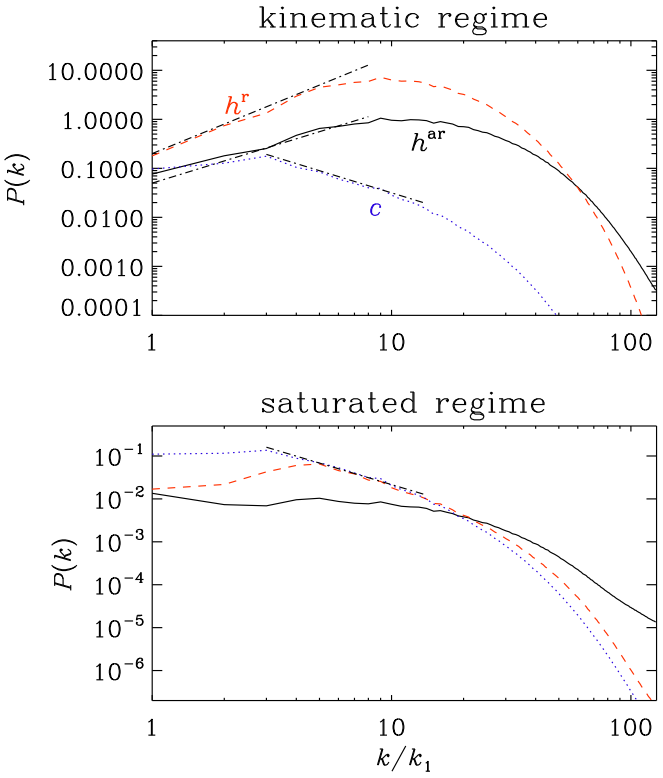

FIG. 9. (Color online) Power spectra of h^r, h^{ar}, and the passive scalar c, both in the kinematic regime (top) and the nonlinear saturated regime (bottom) for Re=80 with Pr_M=Sc=1. In the kinematic regime, the dash-dotted lines have slopes +2 for h^r, +3/2 for h^{ar}, −3/2 for c (top), and −5/3 for c in the saturated regime.

The spectra of h^{ar} in the saturated regime do not present a clear inertial range, so we cannot draw strong conclusions as to possible nondiffusive turbulent fluxes. However, h^r follows the same cascade as the passive scalar. Previous studies in that gauge[1] found that magnetic helicity fluxes were best treated as diffusive, although the fits were imperfect. The diffusive nature is clearly seen in the spectrum while the imperfections of the diffusive fit can be seen in the generation of a peak at the driving scale. This evidence in support of diffusive magnetic helicity fluxes gives us the confidence to predict at what Re_M diffusive magnetic helicity fluxes will play a dominant role in dynamo saturation, i.e., when the diffusive fluxes have a greater effect on magnetic helicity evolution than the resistive terms. This will be done in Sec. V where we reanalyze simulation data from earlier work.[34]

V. REVISITING EARLIER WORK

Earlier work[20,34] on magnetic helicity fluxes in inhomogeneous open systems confirmed that the magnetic helicity density of the small-scale field is gauge-invariant —even if that of the large-scale field is not. The divergence of the mean magnetic helicity flux of the small-scale field is then also gauge-invariant, but its value is small compared with resistive magnetic helicity dissipation. We return to this work to estimate at what Re_M diffusive magnetic helicity fluxes will begin to play a dominant role in dynamo saturation.

We emphasize that we are now discussing helicity properties of what we call the small-scale field. Such a field is

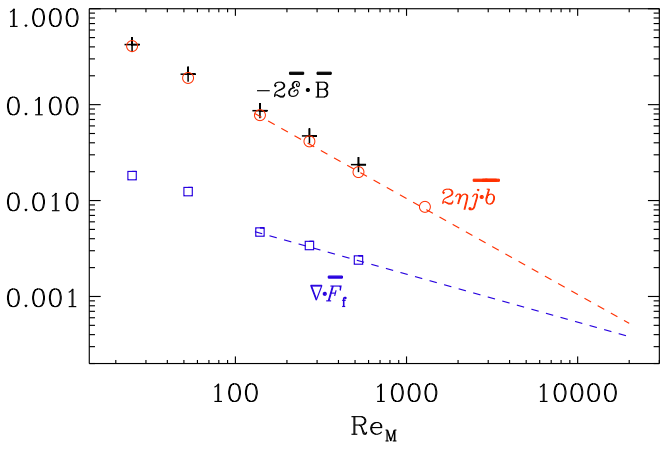

FIG. 10. (Color online) Scaling of $\bar{\mathcal{E}}\cdot\bar{\boldsymbol{B}}$, $\overline{\boldsymbol{j}\cdot\boldsymbol{b}}$, and $\boldsymbol{\nabla}\cdot\bar{\boldsymbol{F}}_f$ vs Re_M for the data of an earlier simulation (Ref. 34) of helically driven turbulence embedded in a poorly conducting nonhelically driven turbulent halo. The symbols show actual data obtained from simulations, the dashed lines are the extrapolation to high Re_M.

defined by introducing an averaged magnetic field, $\bar{\boldsymbol{B}}$, indicated by an overbar. Following earlier work[20,34] we restrict ourselves here to planar (or horizontal) averaging. The small-scale field is then given by $\boldsymbol{b}=\boldsymbol{B}-\bar{\boldsymbol{B}}$, and the mean magnetic and current helicity densities of the fluctuating fields are then $\bar{h}_f\equiv\overline{\boldsymbol{a}\cdot\boldsymbol{b}}$ and $\overline{\boldsymbol{j}\cdot\boldsymbol{b}}$, respectively, where $\boldsymbol{\nabla}\times\boldsymbol{a}=\boldsymbol{b}$ and $\boldsymbol{j}=\boldsymbol{\nabla}\times\boldsymbol{b}$. Turbulent diffusion and the α effect imply helicity transfer between scales[36,37] through the mean electromotive force of the fluctuating field, $\bar{\mathcal{E}}=\overline{\boldsymbol{u}\times\boldsymbol{b}}$, so that the evolution equation for $\bar{h}_f$ takes the form

$$\frac{\partial\bar{h}_f}{\partial t}=-2\bar{\mathcal{E}}\cdot\bar{\boldsymbol{B}}-2\eta\overline{\boldsymbol{j}\cdot\boldsymbol{b}}-\boldsymbol{\nabla}\cdot\bar{\boldsymbol{F}}_f. \tag{26}$$

Here, both $\bar{h}_f$ and $\boldsymbol{\nabla}\cdot\bar{\boldsymbol{F}}_f$ are a gauge-dependent, but if there is a steady state, and if $\bar{h}_f$ is constant, then $\partial\bar{h}_f/\partial t=0$, and since both $\bar{\mathcal{E}}\cdot\bar{\boldsymbol{B}}$ and $\overline{\boldsymbol{j}\cdot\boldsymbol{b}}$ are gauge-invariant, $\boldsymbol{\nabla}\cdot\bar{\boldsymbol{F}}_f$ must also be gauge-invariant. Numerical values for $\bar{\mathcal{E}}\cdot\bar{\boldsymbol{B}}$, $\overline{\boldsymbol{j}\cdot\boldsymbol{b}}$, and $\boldsymbol{\nabla}\cdot\bar{\boldsymbol{F}}_f$ were given earlier[34] for a particular simulation of a slab of helically driven turbulence embedded in a poorly conducting nonhelically driven turbulent halo. In Fig. 10 we show the scaling of all three terms versus Re_M. Note that $-\bar{\mathcal{E}}\cdot\bar{\boldsymbol{B}}$ is balanced mainly by $\overline{\boldsymbol{j}\cdot\boldsymbol{b}}$. However, if the current trend, $\overline{\boldsymbol{j}\cdot\boldsymbol{b}}\sim Re_M^{-1}$ and $\boldsymbol{\nabla}\cdot\bar{\boldsymbol{F}}_f\sim Re_M^{-1/2}$ were to continue, one might expect a cross-over at $Re_M\approx3\times10^4$. If so, the scaling of $\bar{\mathcal{E}}\cdot\bar{\boldsymbol{B}}$ is expected to become shallower, following that of $\boldsymbol{\nabla}\cdot\bar{\boldsymbol{F}}_f$. Given that the largest Re_M accessible today is of order 10^3, we may conclude that an alleviation of quenching through diffusive magnetic helicity fluxes will not be prominent in simulations for the near future. Nevertheless, astrophysical systems such as the Sun are orders of magnitude beyond the estimated critical point of $Re_M\sim3\times10^4$; and we expect their dynamo dynamics to behave accordingly.

VI. CONCLUSIONS

In view of the fact that the time averaged magnetic helicity of the fluctuating fields is gauge-invariant in systems with sufficient scale separation, the gauge-freedom can be exploited to gain insights using gauges that are particularly revealing. Here we have examined an interesting gauge: the advecto-resistive gauge. As the advecto-resistive gauge is inherently numerically unstable, we had to implement a possibly universal technique to run numerical simulations in such unstable gauges by running in a stable gauge while also solving a further equation for the gauge transformation.

The advecto-resistive gauge has allowed us to examine both the consequences of finite resistivity for magnetic helicity density as well as the possibilities of turbulent transport. The magnetic helicity flux, and in particular the contribution from $\eta \boldsymbol{J}\times\boldsymbol{A}^{\rm ar}$ (properly normalized) reaches a constant value as $\eta\to 0$. This behavior is similar to the behavior of energy dissipation in turbulence, known as the law of finite energy dissipation.[38] This is interesting as the source term for the volume integrated magnetic helicity H does in fact tend to zero as η does. In this sense, the high Re_M behavior of magnetic helicity is richer than previously anticipated. Indeed, the generation of spatial magnetic helicity fluctuations *ex nihilo* in nonadvecto-resistive gauges is interesting, with potentially testable implications. We expect that the magnetic helicity fluxes resulting from terms of the form $\eta \boldsymbol{J}\times\boldsymbol{A}^{\rm ar}$ can be modeled as turbulent Fickian diffusion-type fluxes down the gradient of mean magnetic helicity. However, it is clear that fluxes from turbulent diffusion provide only a poor escape from catastrophic α quenching, partly because they cannot distinguish between large- and small-scale fields. Furthermore, in simulations with such turbulent diffusion fluxes, their contribution is still much smaller than the local resistive magnetic helicity dissipation.[20,34] However, the latter decreases faster ($\sim \mathrm{Re}_M^{-1}$) with magnetic Reynolds number than the former ($\sim \mathrm{Re}_M^{-1/2}$), so one may estimate that only for magnetic Reynolds numbers of around 10^4 one has a chance to see the effects of turbulent diffusion. If true, however, such fluxes would definitely be important for the magnetic Reynolds numbers relevant to stars and galaxies—even though such values cannot be reached with present day computer power.

ACKNOWLEDGMENTS

National Supercomputer Centre in Linköping and the Center for Parallel Computers at the Royal Institute of Technology in Sweden. This work was supported in part by the Swedish Research Council (Grant No. 621-2007-4064), and the European Research Council under the AstroDyn Research Project 227952.

APPENDIX A: DERIVATION OF EQ. (5)

We begin by expressing $\boldsymbol{U}\times\boldsymbol{B}$ in terms of $\boldsymbol{A}$

$$(\boldsymbol{U}\times\boldsymbol{B})_i = U_j A_{j,i} - U_j A_{i,j}. \tag{A1}$$

The last term can be subsumed into an advective derivative term for $\boldsymbol{A}$. Using furthermore $U_j A_{j,i} = (U_j A_j)_{,i} - U_{j,i} A_j$, we can write Eq. (2) as

$$\frac{DA_i^W}{Dt} = -U_{j,i}A_j^W + (\boldsymbol{U}\cdot\boldsymbol{A}^W)_{,i} - \eta J_i. \tag{A2}$$

We now insert Eq. (3) for $\boldsymbol{A}^W = \boldsymbol{A}^a - \boldsymbol{\nabla}\Lambda^{W:a}$, so

$$\frac{DA_i^a}{Dt} - \frac{D\Lambda_{,i}^{W:a}}{Dt} = -U_{j,i}A_j^a + U_{j,i}\Lambda_{,j}^{W:a} + (\boldsymbol{U}\cdot\boldsymbol{A}^W)_{,i} - \eta J_i. \tag{A3}$$

and note that

$$-\frac{D\Lambda_{,i}^{W:a}}{Dt} = -\nabla_i\left(\frac{D\Lambda^{W:a}}{Dt}\right) + U_{j,i}\Lambda_{,j}^{W:a}. \tag{A4}$$

The last term cancels and we are left with

$$\frac{DA_i^a}{Dt} + U_{j,i}A_j^a + \eta J_i = \nabla_i\left(\frac{D\Lambda^{W:a}}{Dt} + \boldsymbol{U}\cdot\boldsymbol{A}^W\right), \tag{A5}$$

so we recover the evolution equation for the advective gauge provided Eq. (5) is obeyed.

APPENDIX B: DERIVATION OF EQ. (15)

We present here the derivation of the transformation from the resistive gauge to the advecto-resistive gauge, proceeding analogously to the derivation presented in Appendix A. However, instead of Eq. (A2) we now have

$$\frac{DA_i^r}{Dt} = -U_{j,i}A_j^r + (\boldsymbol{U}\cdot\boldsymbol{A}^r)_{,i} + \eta\nabla^2 A_i^r. \tag{B1}$$

Inserting Eq. (13) for $\boldsymbol{A}^r = \boldsymbol{A}^{\rm ar} - \boldsymbol{\nabla}\Lambda^{r:{\rm ar}}$, we obtain an Equation similar to Eq. (A3)

$$\frac{DA_i^{\rm ar}}{Dt} - \frac{D\Lambda_{,i}^{r:{\rm ar}}}{Dt} = -U_{j,i}A_j^{\rm ar} + U_{j,i}\Lambda_{,j}^{r:{\rm ar}} + (\boldsymbol{U}\cdot\boldsymbol{A}^r)_{,i} + \eta\nabla^2 A_i^{\rm ar} - \eta\nabla^2\Lambda_{,i}^{r:{\rm ar}} \tag{B2}$$

which leads to

$$\frac{DA_i^{\rm ar}}{Dt} + U_{j,i}A_j^{\rm ar} - \eta\nabla^2 A_i^{\rm ar} = \nabla_i\left(\frac{D\Lambda_i^{r:{\rm ar}}}{Dt} + \boldsymbol{U}\cdot\boldsymbol{A}^r - \eta\nabla^2\Lambda^{r:{\rm ar}}\right) \tag{B3}$$

so we recover the evolution equation for the advecto-resistive gauge provided Eq. (15) is obeyed.

[1] A. Hubbard and A. Brandenburg, Astrophys. J. **727**, 11 (2010).
[2] J. B. Taylor, Rev. Mod. Phys. **58**, 741 (1986).
[3] W. H. Matthaeus and D. Montgomery, Ann. N.Y. Acad. Sci. **357**, 203 (1980).
[4] A. Pouquet, U. Frisch, and J. Leorat, J. Fluid Mech. **77**, 321 (1976).
[5] A. Brandenburg and K. Subramanian, Phys. Rep. **417**, 1 (2005).
[6] S. I. Vainshtein and F. Cattaneo, Astrophys. J. **393**, 165 (1992).
[7] F. Cattaneo and D. W. Hughes, Phys. Rev. E **54**, R4532 (1996).

[8]E. G. Blackman and G. B. Field, Mon. Not. R. Astron. Soc. **318**, 724 (2000).
[9]E. G. Blackman and G. B. Field, Astrophys. J. **534**, 984 (2000).
[10]B. P. Brown, M. K. Browning, A. S. Brun, M. S. Miesch, and J. Toomre, Astrophys. J. **711**, 424 (2010).
[11]P. J. Käpylä, M. J. Korpi, A. Brandenburg, D. Mitra, and R. Tavakol, Astron. Nachr. **331**, 73 (2010).
[12]P. Charbonneau, Living Reviews in Solar Physics **7**, 3 (2010), http://livingreviews.org/lrsp-2010-3.
[13]S. E. Gibson, L. Fletcher, G. D. Zanna, C. D. Pike, H. E. Mason, C. H. Mandrini, P. Dmoulin, H. Gilbert, J. Burkepile, T. Holzer, D. Alexander, Y. Liu, N. Nitta, J. Qiu, B. Schmieder, and B. J. Thompson, Astrophys. J. **574**, 1021 (2002).
[14]K. D. Leka, R. C. Canfield, A. N. McClymont, and L. van Driel-Gesztelyi, Astrophys. J. **462**, 547 (1996).
[15]P. K. Manoharan, L. van Driel-Gesztelyi, M. Pick, and P. Demoulin, Astrophys. J. **468**, L73+ (1996).
[16]R. C. Canfield, H. S. Hudson, and D. E. McKenzie, Geophys. Res. Lett. **26**, 627, doi:10.1029/1999GL900105 (1999).
[17]A. Shukurov, D. Sokoloff, K. Subramanian, and A. Brandenburg, Astron. Astrophys. **448**, L33 (2006).
[18]A. Brandenburg, S. Candelaresi, and P. Chatterjee, Mon. Not. R. Astron. Soc. **398**, 1414 (2009).
[19]E. G. Blackman and A. Brandenburg, Astrophys. J. **584**, L99 (2003).
[20]D. Mitra, S. Candelaresi, P. Chatterjee, R. Tavakol, and A. Brandenburg, Astron. Nachr. **331**, 130 (2010).
[21]K. Subramanian and A. Brandenburg, Astrophys. J. Lett. **648**, L71 (2006).
[22]E. T. Vishniac and J. Cho, Astrophys. J. **550**, 752 (2001).
[23]D. J. Price and C. Federrath, Astron. Soc. Pac. Conf. Ser. **429**, 274 (2010).
[24]D. J. Price, Mon. Not. R. Astron. Soc. **401**, 1475 (2010).
[25]A. Brandenburg, Mon. Not. R. Astron. Soc. **401**, 347 (2010).
[26]A. Brandenburg, A. Nordlund, R. F. Stein, and U. Torkelsson, Astrophys. J. **446**, 741 (1995).
[27]M. A. Berger, Geophys. Astrophys. Fluid Dyn. **30**, 79 (1984).
[28]A. Brandenburg, Astrophys. J. **550**, 824 (2001).
[29]W. Dobler, A. Shukurov, and A. Brandenburg, Phys. Rev. E **65**, 036311 (2002).
[30]A. Brandenburg, P. J. Käpylä, and A. Mohammed, Phys. Fluids **16**, 1020 (2004).
[31]A. Brandenburg and W. Dobler, Comput. Phys. Commun. **147**, 471 (2002).
[32]A. Brandenburg, Astron. Nachr. **332**, 51 (2010).
[33]N. I. Kleeorin and A. A. Ruzmaikin, Magnetohydrodynamics **2**, 17 (1982).
[34]A. Hubbard and A. Brandenburg, Geophys. Astrophys. Fluid Dyn. **104**, 577 (2010).
[35]N. E. L. Haugen, A. Brandenburg, and W. Dobler, Phys. Rev. E **70**, 016308 (2004).
[36]N. Seehafer, Phys. Rev. E **53**, 1283 (1996).
[37]H. Ji, Phys. Rev. Lett. **83**, 3198 (1999).
[38]U. Frisch, *Turbulence. The Legacy of A. N. Kolmogorov* (Cambridge University Press, Cambridge, 1995).